



UNIVERSITÀ DEGLI STUDI DI GENOVA

CORSO DI DOTTORATO IN FLUIDODINAMICA E
PROCESSI DELL' INGEGNERIA AMBIENTALE

Numerical and analytical study of combustion instabilities in industrial gas turbines

Thesis submitted for the degree of Doctor of Philosophy

Candidate:

Dmytro Iurashev

Supervisors:

Dr Giovanni Campa, Ansaldo Energia S.p.A.

Prof. Alessandro Bottaro, University of Genoa

Reviewers:

Prof. Maria Heckl, Keele University

Prof. Wolfgang Polifke, Technical University of Munich

Abstract

For the last two decades, gas turbine producers have faced the problem of combustion instabilities - strong combustion-driven pressure fluctuations. Such pressure oscillations can lead to heavy damage of gas turbines. Despite the enormous work done in this field, the problem of the occurrence of such instabilities is still not fully understood and has to be investigated. In particular, tools to predict combustion instabilities are in high demand.

A three-step approach to predict combustion instabilities in gas turbines is proposed in this work. The first step is to compute the heat release response of the burner to the velocity excitation at various frequencies and amplitudes. To accomplish this task, Unsteady Reynolds-Averaged Navier-Stokes (URANS) simulations are performed with a Flame Speed Closure (FSC) model implemented in the OpenFOAM environment. To compute the heat release response to small-amplitude excitations, the setup is excited with the broadband signal and a Wiener-Hopf inversion is performed. The second step is to approximate the computed heat release response with a time-lag distributed flame model. The third step is to model closed loop thermoacoustic phenomena with a low-order network model. The network model is implemented in a Simulink environment and simulations in the time domain are performed. The time domain simulations with the time-lag distributed flame model allow computing both frequencies and amplitudes of pressure oscillations in a straightforward way.

The three-step approach is first applied to a laboratory test rig. The time-lag distributed flame model presented in the literature for low-amplitude excitation is extended to high-amplitude excitation. Dependencies of the model parameters on the amplitude of the excitation are calculated and justified. The stability prediction approximates well the available experimental data. The unstable acoustic mode of the setup is associated with the unsteady heat release; this acoustic mode would not appear in the absence of unsteady heat release. The dependencies of the computed mode on the acoustic characteristics of the setup are addressed. A dependence of the unstable mode on the amplitude of the acoustic oscillations is observed and explained.

Then, the three-step approach is applied to an industrial test rig. URANS simulations with the FSC model are conducted and the heat release response to the acoustic excitation at different amplitudes is calculated. The computed heat release response is approximated with a time-lag distributed model for technically-premixed swirl-stabilised flames. The response of the technically-premixed swirl-stabilised flames to excitations is characterised by a more complicated physics than for perfectly-premixed flames. However, if certain conditions are met, the heat release response of the technically-premixed flames can be modelled by fewer parameters than the perfectly premixed flames. Dependencies of the flame model parameters on the excitation amplitude are computed and justified. Several flame models are presented for this setup. Results of the stability analysis in the network model with one of the flame models agree with the experimental analysis both in terms of the unstable frequency and its amplitude.

Contents

1	Introduction to the problem	19
1.1	The gas turbine	19
1.2	Combustion and flame types	19
1.3	Flashback, blow-off and flame stabilisation	25
1.4	Combustion instabilities phenomena	28
1.5	Prediction of thermoacoustic instabilities: state of the art	32
1.6	Structure of the work	37
2	Description of the three-step approach for prediction of combustion instabilities in gas turbines	39
2.1	FDF computation with CFD simulations	39
2.1.1	Overview of URANS method	41
2.1.2	FSC model description	45
2.1.3	Numerical determination of the FTF and FDF	47
2.2	Analytical models for FTF	51
2.2.1	Time-lag distributed FTF model for perfectly premixed, swirl-stabilised, flames	51
2.2.2	Time-lag distributed FTF model for technically premixed, swirl-stabilised, flames	55
2.3	Description of the network model approach	63
2.3.1	Waves propagation in sections	63
2.3.2	Area changes	64
2.3.3	Unsteady heat release	67
2.3.4	Boundary conditions	68
2.3.5	Elements interconnection	68
2.4	Discussion	69
3	Application of the three-step approach to a laboratory, perfectly premixed, setup	71
3.1	Description of the setup	71
3.2	CFD simulations	72
3.2.1	Numerical setup	72
3.2.2	Results of unperturbed simulations	73
3.2.3	FDF computations	75
3.3	Analytical models for the FDF	79
3.3.1	Rational time-lagged FTF model	79

3.3.2	Time-lag distributed FTF models	80
3.3.3	Time-lag distributed FDF model	85
3.4	Network model simulations	89
3.4.1	Numerical setup	89
3.4.2	Results of the linear analysis	91
3.4.3	Results of the weakly nonlinear analysis	103
3.5	Discussion	113
4	Application of the three-step approach to an industrial, technically premixed, setup	115
4.1	Description of the setup	115
4.2	Overview of the reference LES study	119
4.2.1	Description of the LES software	119
4.2.2	Description of the numerical setup	119
4.2.3	FTF numerical calculation	120
4.3	URANS simulations	121
4.3.1	Numerical setup	121
4.3.2	Results of unperturbed simulations	123
4.3.3	FDF computations	125
4.4	Analytical time-lag distributed FDF models	131
4.4.1	FTF models	131
4.4.2	FDF model 1	131
4.4.3	FDF model 2	134
4.4.4	FDF model 3	136
4.4.5	FDF model 4	137
4.4.6	FDF model 5	137
4.5	Network model simulations	138
4.5.1	Numerical setup	138
4.5.2	Results of linear analysis	139
4.5.3	Results of weakly nonlinear analyses	141
4.6	Discussion	145
5	Conclusions and future investigations	147
	Bibliography	155

List of Figures

1.1	Gas turbine main components shown on the example of an Ansaldo Energia gas turbine.	20
1.2	Scheme of open Brayton cycle.	20
1.3	Brayton cycle in the p-V diagram.	21
1.4	Brayton cycle in the T-s diagram.	21
1.5	Perfectly premixed (a), technically premixed (b), partially premixed (c), and diffusion (d) flames.	23
1.6	Diffusion flame structure [1].	24
1.7	Premixed flame structure [1].	24
1.8	Experimental images of flame flashback in (a) core flow and (b) boundary layer. Images from (a) Kröner et al. [2] and (b) Heeger et al. [3], adapted by Lieuwen [4].	26
1.9	Illustration of flames stabilised by (a) a bluff body, (b) a backward-facing step, and (c) a swirling flow [4].	26
1.10	Types of flow swirlers: (a) axial, (b) diagonal, and (c) radial.	27
1.11	Flame blow-off in the SR-71 during a high-acceleration manoeuvre [5].	27
1.12	Basic flame configurations possible for an annular, swirling flow geometry [4].	28
1.13	Explanation of the physical mechanism within the Rijke tube [6].	29
1.14	Transition piece damaged by combustion instability [7].	30
1.15	Combustion liner damaged by combustion instability [8].	31
1.16	New burner assembly (left) and burner assembly damaged by combustion instability (right) [8].	31
1.17	Scheme of a combustor as a thermoacoustic system.	32
1.18	Different types of analysis [9].	35
2.1	Law of the wall modelled with Eq. 2.26.	44
2.2	Unit impulse (left) and causal, finite-duration response (right).	49
2.3	Scheme of a perfectly premixed thermoacoustic system.	51
2.4	Unperturbed components of the velocity before and after the swirler.	52
2.5	Mean and oscillating components of the velocity before and after the swirler.	53
2.6	Characteristic convective time lags in perfectly premixed swirl-stabilised burners modelled with Eqs. 2.65-2.66.	54
2.7	UIR of the heat release to the velocity excitation [10].	55

LIST OF FIGURES

2.8	Response of the heat release to unit impulses of different components of the velocity modelled with Eqs. 2.66, 2.68, 2.70. . . .	55
2.9	FTF of the perfectly premixed flame modelled with Eqs. 2.65, 2.69, 2.71.	56
2.10	Physical mechanisms through which equivalence ratio fluctuations influence heat release fluctuations.	56
2.11	UIR of the heat release to the equivalence ratio perturbation [10].	57
2.12	Characteristic convective time lags in technically premixed, swirl-stabilised, burners; general case.	58
2.13	Response of the heat release to the unit impulse of equivalence ratio, modelled with Eq. 2.74.	58
2.14	FTF of the heat release perturbations due to the equivalence ratio perturbations modelled with Eq. 2.75.	58
2.15	Response of the heat release to the unit impulse of velocity modelled with Eq. 2.66, to the unit impulse of equivalence ratio modelled with Eq. 2.74, and the total UIR modelled with the general Eq. 2.78.	60
2.16	FTF of the heat release perturbations due to the velocity perturbations modelled with Eq. 2.65, due to the equivalence ratio perturbations modelled with Eq. 2.75, and the total FTF modelled with the general Eq. 2.77.	60
2.17	Characteristic convective time lags in technically premixed swirl-stabilised burners with fuel injection on the blades.	61
2.18	Response of the heat release to the unit impulse of velocity modelled with Eq. 2.66, to the unit impulse of equivalence ratio modelled with Eq. 2.74, the total UIR modelled with the general Eq. 2.78, and the total UIR modelled with the simplified Eq. 2.82.	61
2.19	FTF of the heat release perturbations due to the velocity perturbations modelled with Eq. 2.65, due to the equivalence ratio perturbations modelled with Eq. 2.75, the total FTF modelled with the general Eq. 2.77, and the total FTF modelled with the simplified Eq. 2.81.	62
2.20	FTFs in the complex plane in the range of frequencies 0–200 Hz. FTF of the heat release perturbations due to the velocity perturbations modelled with Eq. 2.65, due to the velocity perturbations through equivalence ratio perturbations modelled with Eq. 2.75, the total FTF modelled with the general Eq. 2.77, and the total FTF modelled with the simplified Eq. 2.81.	63
2.21	Scheme of waves propagating in a section for a low-order model.	64
2.22	Scheme of waves propagation between adjacent sections in a low-order model.	64
2.23	Elements interconnection in a low-order network model.	69
3.1	Scheme of the BRS test rig (image courtesy of Thomas Komarek).	72
3.2	Sector scheme of the numerical set-up of the BRS test rig. . . .	72
3.3	Axial velocity distribution from the unperturbed simulation. . .	74

3.4	Temperature distribution from the unperturbed simulation.	74
3.5	Normalised unperturbed heat release distribution from the simulation.	74
3.6	OH* chemiluminescence distribution from experiment and heat release distribution from the simulation.	75
3.7	Signal of the velocity excitation.	76
3.8	Fast Fourier Transform of the excitation signal shown in Fig. 3.7.	76
3.9	FTF obtained experimentally [9] and from simulations.	77
3.10	Coefficients h_k computed from FTFs obtained experimentally [9] and from simulations.	78
3.11	FTF (dashed line) and FDF (points) obtained from simulations.	79
3.12	Normalised perturbations of velocity at reference point u'_r/\bar{u}_r and heat release Q'/\bar{Q} during one period of oscillations (excitation at 240 Hz with amplitude 70%).	80
3.13	Heat release distribution in the setup at different phases of a period of oscillations (excitation at 240 Hz with amplitude 70%).	81
3.14	Heat release distribution at four instances of one period of oscillations (excitation at 240 Hz with amplitude 70%) and heat release distribution in the setup without perturbation.	82
3.15	Heat release distribution in the setup without perturbation and heat release distribution averaged over one period of oscillations (excitation at 240 Hz with amplitude 70%).	82
3.16	FTF of the BRS test rig calculated from OpenFOAM simulations and its RTL FTF model (Eq. 3.3).	83
3.17	Experimental FTF of BRS and its TLD model.	83
3.18	UIR computed from the experimental FTF [9] and modelled by Eq. 3.5.	84
3.19	FDF of BRS setup modelled with Eq. 3.7.	86
3.20	Dependencies $\tau_j(A)$ and $\sigma_j(A)$ from Tab. 3.5 (points, 'Model') and modelled by Eqs. (3.8)-(3.9) (lines, '2-modeled').	87
3.21	UIRs for different amplitudes of velocity excitations modelled by Eq. (3.5).	88
3.22	Scheme of BRS network model numerical setup.	90
3.23	Dominant frequency of oscillations and its growth rate for various lengths of the combustion chamber; $x_{fl} = 0.03$ m, $k_G = 1$, $\tau_{add} = 0$ ms.	92
3.24	Scheme of formation of ITA modes.	93
3.25	Dominant frequency of oscillations and its growth rate for various positions of the flame; $L_{c.c} = 0.7$ m, $k_G = 1$, $\tau_{add} = 0$ ms.	94
3.26	Dominant frequency of oscillations and its growth rate for various values of the parameter k_G parameter; $L_{c.c} = 0.7$ m, $x_{fl} = 0.03$ m, $\tau_{add} = 0$ ms.	95
3.27	Dominant frequency of oscillations and its growth rate for various values of the parameter τ_{add} ; $L_{c.c} = 0.7$ m, $x_{fl} = 0.03$ m, $k_G = 1$	96

LIST OF FIGURES

3.28	Dominant frequency of oscillations and its growth rate for various values of Δx_{flame} parameter; $L_{c.c} = 0.7$ m, $k_G = 1$, $\tau_{add} = \Delta x_{flame}/\bar{u}_r$	97
3.29	Dominant frequency of oscillations and its growth rate for various combustion chamber length and three values of the outlet reflection coefficient.	98
3.30	Dominant frequency of oscillations and its growth rate for various values of the outlet reflection coefficient and three combustion chamber lengths.	100
3.31	Dominant frequency of oscillations and its growth rate for various plenum lengths and three values of the inlet reflection coefficient; $R_{out} = 0$	101
3.32	History of pressure oscillations at the beginning of the combustor; $R_{in} = 1$, $L_{pl} = 5.8$ m, $R_{out} = 0$	102
3.33	Dominant frequency of oscillations and its growth rate for various plenum lengths and three values of the inlet reflection coefficient; $R_{out} = 0$	103
3.34	Validation of the linear response of the TLD flame model to small-amplitude velocity excitations.	104
3.35	Validation of the nonlinear response of the TLD flame model to velocity excitations at 100 Hz; top to bottom excitation amplitudes 30%, 50%, and 70%.	106
3.36	Validation of the nonlinear response of the TLD flame model to velocity excitations at 160 Hz; top to bottom excitation amplitudes 30%, 50%, and 70%.	107
3.37	Validation of the nonlinear response of the TLD flame model to velocity excitations at 240 Hz; top to bottom excitation amplitudes 30%, 50%, and 70%.	108
3.38	Validation of the nonlinear response of the TLD flame model to velocity excitations at 320 Hz; top to bottom excitation amplitudes 30%, 50%, and 70%.	109
3.39	Pressure perturbations at the flame with $L_{c.c.} = 0.3$ m and $T_{comb\ 2} = 1930$ K.	110
3.40	Normalised instantaneous velocity perturbations between Sections 3 and 4 of the network model setup and instantaneous A parameter with $L_{c.c.} = 0.3$ m and $T_{comb\ 2} = 1930$ K.	110
3.41	Pressure perturbations at the flame with $L_{c.c.} = 0.7$ m and $T_{comb\ 2} = 1930$ K.	110
3.42	Normalised instantaneous velocity perturbations between Sections 3 and 4 of the network model setup and instantaneous A parameter with $L_{c.c.} = 0.7$ m and $T_{comb\ 2} = 1930$ K.	111
3.43	Amplitude of pressure perturbations at the flame for different $L_{c.c.}$ and $T_{comb\ 2}$	111
3.44	Normalised amplitude of velocity perturbations after the swirler for different $L_{c.c.}$ and $T_{comb\ 2}$	111

3.45	Dominant frequency of pressure perturbations at the flame for different $L_{c.c.}$ and $T_{comb 2}$	112
3.46	Amplitude of pressure perturbations at the flame in network model simulations with the FTF obtained experimentally and using the FTF obtained from numerical simulations with $T_{comb 2} = 1930$ K.	112
3.47	Dominant frequency of pressure perturbations at the flame obtained using the FTF obtained experimentally and using the FTF obtained from numerical simulations with $T_{comb 2} = 1930$ K.	113
3.48	Unstable frequency of pressure perturbations at the flame obtained using the FTF and using the FDF obtained numerically with $T_{comb 2} = 1930$ K.	113
4.1	Scheme of the industrial test rig [11].	115
4.2	Multi-perforated outlet disk.	116
4.3	Schematic view of an industrial gas turbine test burner [12].	117
4.4	Typical FFT of two pressure transducers during a humming phenomenon.	118
4.5	Optical transducer and pressure transducer signals, logarithmic scale, arbitrary units (A.U.). Left Y axis refers to the optical transducer signal while the right Y axis refers to the pressure transducer signal.	118
4.6	Normalised heat release; LES [13].	120
4.7	Schematic probes positions for the FTF calculation in the LES [13].	121
4.8	Scheme of the numerical setup.	121
4.9	Dependence of the normalised local mixture temperature on the equivalence ratio.	122
4.10	Dependence of the normalised laminar flame speed on the equivalence ratio calculated with Cantera [14] and modelled by Eq. 4.3.	123
4.11	Normalised longitudinal component of velocity; URANS simulation.	124
4.12	Normalised temperature; URANS simulation.	124
4.13	Normalised heat release; URANS simulation.	124
4.14	Normalised laminar flame speed distribution at the CBO outlet plane; URANS simulation.	124
4.15	Heat release distributions from LES and URANS simulation.	125
4.16	Relative pressure distributions from experiment, LES [13], and URANS simulation.	126
4.17	Fast Fourier Transform of the excitation signal applied in the FTF calculation with URANS.	126
4.18	Normalised root mean square deviation of heat release; URANS FTF calculation simulations.	127
4.19	Normalised heat release from unperturbed simulation and its root mean square deviation from FTF calculation simulations; URANS simulations.	127

LIST OF FIGURES

4.20	FTFs computed with LES in AVBP [13] and with URANS in OpenFOAM.	128
4.21	Normalised root mean square deviation of heat release; URANS simulations 30% excitation at frequency $1.05 St$	129
4.22	Normalised heat release root mean square deviation from FTF calculation simulations and simulations with 30% excitation at frequency $1.05 St$; URANS simulations.	130
4.23	FDf computed with URANS in OpenFOAM.	130
4.24	FTF computed with LES and modelled with Eq. 4.5.	132
4.25	UIRs for low amplitude excitation modelled with Eq. 4.6.	132
4.26	FDf computed with URANS in OpenFOAM and FDF model 1.	133
4.27	UIRs modelled with Eq. 4.6 for low amplitude excitation.	133
4.28	Dependencies $\tau_i(A)$ and $\sigma_i(A)$ in FDF model 1.	134
4.29	FDf computed with URANS in OpenFOAM and FDF model 2.	135
4.30	UIRs modelled with Eq. 4.6.	135
4.31	Dependencies $\tau_i(A)$ and $\sigma_i(A)$ in FDF model 2.	136
4.32	Scheme of the network model numerical setup of the industrial test rig.	139
4.33	Dominant frequencies of the pressure oscillations and their growth rates for various lengths of the combustion chamber calculated using LES FTF model and URANS FTF model; outlet reflection coefficient $R_{out,1}$	140
4.34	Unstable frequencies and amplitudes of pressure oscillations for various values of the combustion chamber length calculated with the network model and the FDF model 3; outlet reflection coefficient $R_{out,1}$ measured experimentally.	142
4.35	Unstable frequencies and amplitudes of pressure oscillations for various values of the combustion chamber length calculated with the network model and the FDF model 4.	143
4.36	Unstable frequencies and amplitudes of pressure oscillations for various combustion chamber lengths and outlet reflection coefficients calculated with the network model and the FDF model 5.	144

List of Tables

2.1	Constants of the <i>SST</i> $k - \omega$ model.	43
3.1	Boundary Conditions for the BRS numerical model.	73
3.2	Coefficients of the RTL FTF model (Eq. 3.3)	80
3.3	Values of parameters τ_j and σ_j for the TLD model of the experimental and numerical FTFs, ms.	81
3.4	Values of parameters τ_j f_{h-fl} for the TLD model of the experimental and numerical FTFs, ms.	85
3.5	Values of parameters τ_j and σ_j for different amplitudes of perturbation in simulations, ms	86
3.6	Values of parameters $\tau_{j,lin}$, Θ_i , $\sigma_{j,lin}$ and Σ_j in the TLD FDF model.	87
3.7	Default values of parameters imposed in the network model.	90
3.8	Dominant frequencies and their growth rates for the case without plenum and various inlet reflection coefficient values.	103
3.9	Quality of Fit calculated by Eq. 3.14 of the heat release modelled with the nonlinear TLD flame model in Simulink with respect to the one computed with OpenFOAM simulations.	105
4.1	Values of normalised parameters τ_i and σ_i for model of FTF calculated with LES and URANS simulation.	131
4.2	Values of normalised parameters $\tau_{i,lin}$, Θ_i , $\sigma_{i,lin}$ and Σ_i for FDF models.	134
4.3	Values of parameters imposed in the network model of the industrial test rig.	138

Nomenclature

Latin

A	normalised velocity amplitude
a	thermal diffusivity
b	regress variable
CA	Computational Acoustics
CAA	Computational Aero-Acoustics
CBO	Cylindrical Burner Outlet
CFD	Computational Fluid Dynamics
C_D	constant
C_j	constant
C_μ	constant
c_p	specific heat capacity at constant pressure
c_s	speed of sound
c_n	cross-correlation
D	diffusion coefficient
DNS	Direct Numerical Simulations
F	blending function
FDF	Flame Describing Function
FEM	Finite Element Method
FTF	Flame Transfer Function
FSC	Flame Speed Closure
FVM	Finite Volume Method
f	downstream propagating acoustic wave
g	upstream propagating acoustic wave
h	enthalpy
h_n	Unit Impulse Response
K	kinetic energy
k	Turbulent Kinetic Energy (TKE)
k_G	gain dimensionless multiplier

L	length
LEE	Linearized Euler Equations
LES	Large Eddy Simulations
LNSE	Linearized Navier-Stokes Equations
l_t	turbulence length scale
M	duration of Unit Impulse Response / Mach number
m	mass flow rate
N	length of time series
n	interaction index / normal
P	production limiter
Pr	Prandtl number
p	pressure
Q	heat release rate
q	heat flux
R	ideal gas constant
R_{in}	inlet reflection coefficient
R_{out}	outlet reflection coefficient
RTL	Rational Time-Lagged
S	invariant measure of the strain / cross-sectional area
S_{ij}	strain-rate tensor
S_L	laminar flame speed
S_t	turbulent flame speed
Sc	Schmidt number
St	Strouhal number
s	entropy / stoichiometric ratio
T	temperature
TFC	Turbulent Flame Closure
TLD	Time-Lag Distributed
t	time
t_L	Lagrangian time scale of turbulence
UIR	Unit Impulse Response
URANS	Unsteady Reynolds-averaged Navier-Stokes
u	velocity
V	volume
W	molecular weight
x	space vector
Y	mass fraction
y	distance to wall
Z	operator of z -transformation

Greek

α	cycle increment (growth rate)
β	constant
Γ_{mn}	auto-correlation
γ	constant / heat capacity ratio
Δp	pressure difference
Δt	time step
δ_{ij}	Kronecker index
δ_i	unit impulse
ϵ	turbulence dissipation rate
ζ	pressure loss coefficient
Θ	normalised time delay
μ	dynamic viscosity
κ	constant
λ	thermal conductivity
ν	kinematic viscosity / number of moles
ρ	density
Σ	normalised standard deviation
σ	standard deviation
σ_{ij}	viscous stress tensor
τ	time delay
τ_{ij}	Reynolds stress
τ_w	shear stress
ϕ	equivalence ratio / phase
ϕ_{refl}	reflection coefficient phase
ξ	damping ratio
ω	Specific Dissipation Rate (SDR) / angular frequency

Subscripts

<i>ax</i>	axial
<i>b</i>	burnt
<i>beg</i>	section beginning
<i>comb</i>	combustor section
<i>c.c.</i>	combustion chamber
<i>d</i>	downstream
<i>decr</i>	area decrease
<i>end</i>	section end
<i>exc</i>	excitation
<i>F</i>	fuel
<i>fd</i>	flame development
<i>fl</i>	flame
<i>imag</i>	imaginary part of complex number
<i>incr</i>	area increase
<i>log</i>	logarithmic
<i>mix</i>	mixture
<i>O</i>	oxidizer
<i>P</i>	combustion products
<i>pl</i>	plenum
<i>R</i>	reactants
<i>r</i>	reference
<i>real</i>	real part of complex number
<i>st</i>	stoichiometric
<i>t</i>	turbulent
<i>tang</i>	tangential
<i>tot</i>	total
<i>u</i>	unburnt / upstream
<i>vis</i>	viscous

Superscripts

-	mean quantity
'	fluctuating quantity
^	Fourier transform
<i>mod</i>	model
<i>simpl</i>	simplified

Chapter 1

Introduction to the problem

1.1 The gas turbine

The gas turbine is an internal combustion engine of continuous action in which energy of compressed heated gas is transformed into rotating energy of a shaft. The main gas turbine components are the compressor, the combustion chamber and the turbine (see Fig. 1.1). Nowadays, gas turbines are widely used in aeronautics as aircraft engines, in marine for propulsion, for mechanical and electrical power generation.

The processes which occur in a gas turbine can be described by the Brayton cycle and are schematically shown in Fig. 1.2. First, the working fluid, usually air, is compressed in the compressor following the path 1-2 (see Fig. 1.3 and 1.4). Then, air is mixed with the fuel in the combustion chamber and is burnt there. Energy in the form of heat, Q_{2-3} , is supplied to the working fluid during the isobaric process 2-3. After the combustion chamber, the working fluid (now combustion products) is directed to the turbine (step 3-4). There, heated compressed gas enters the nozzle guide vanes channels, where a part of the internal energy is transformed into kinetic energy of the flow [15]. Then, the flow acts on the rotating blades and produces torque on the turbine shaft. After the turbine, the fluid at atmospheric pressure is either directed to the atmosphere or can be further used as a source of energy in the form of heat Q_{4-1} . The processes 1-2 and 3-4 are isentropic in the idealised case and adiabatic in general. Part of the rotating energy of the turbine shaft is given to the compressor; another part is the effective work of the gas turbine. It can be further used as a source of mechanical work or to produce electric energy if an electric generator is connected.

Processes that take place in the combustion chamber are discussed in this work.

1.2 Combustion and flame types

The following definition of combustion was given by Frank-Kamenetskii [16]: 'chemical reaction in conditions of progressing self-acceleration connected to

1. Introduction to the problem

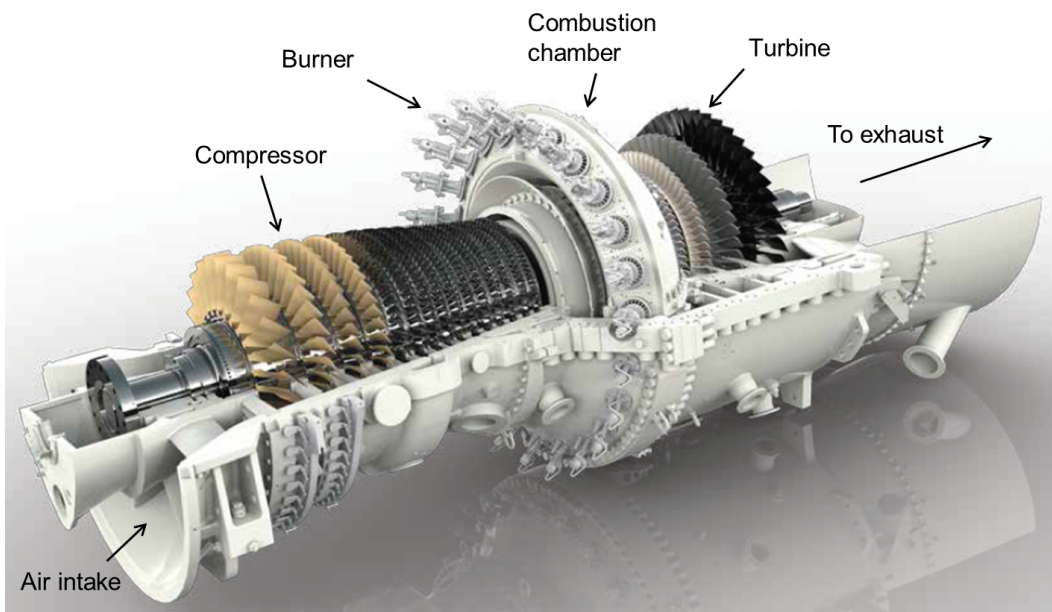


Figure 1.1: Gas turbine main components shown on the example of an Ansaldo Energia gas turbine.

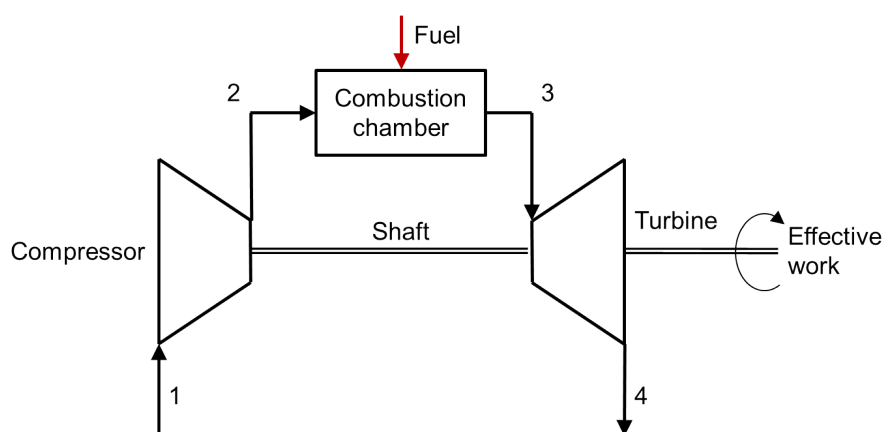


Figure 1.2: Scheme of open Brayton cycle.

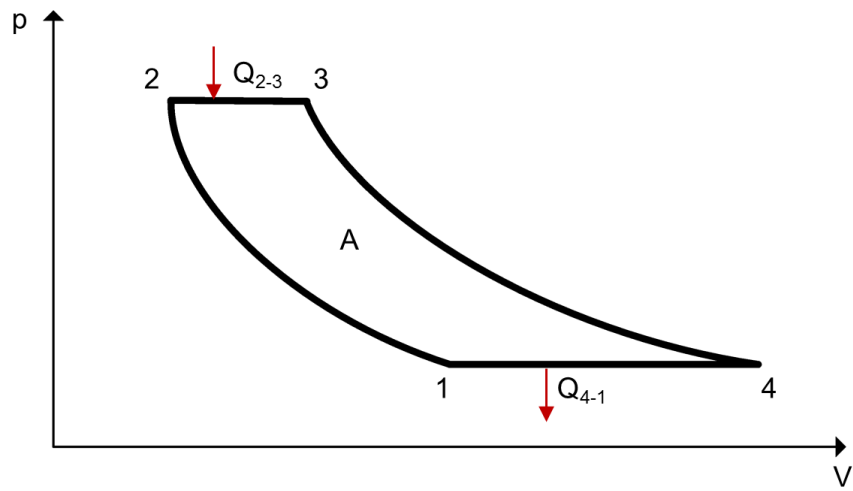


Figure 1.3: Brayton cycle in the p-V diagram.

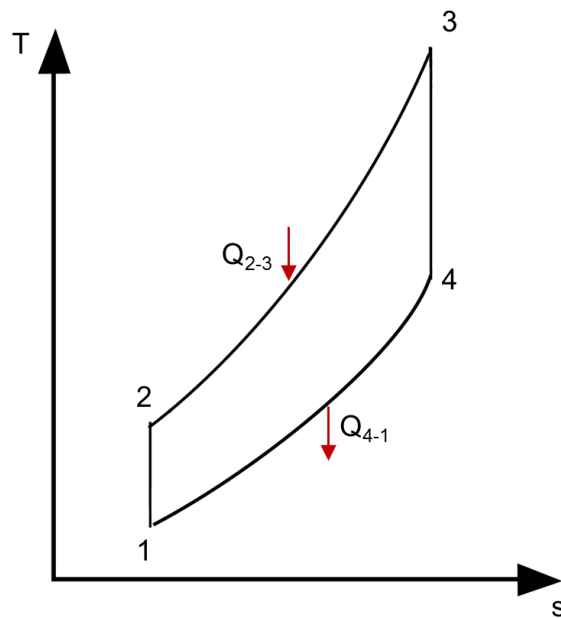


Figure 1.4: Brayton cycle in the T-s diagram.

heat accumulation or catalysing reaction products'. Combustion can be divided into four categories: perfectly premixed, technically premixed, partially premixed, and diffusion [17] (see Fig. 1.5).

Conversion of reactants into combustion products can be described by an overall unique one-step reaction of the form



where ν'_F , ν'_O and ν''_P are numbers of moles of fuel F , oxidizer O and combustion products P , respectively. The mass fractions of fuel Y_F and oxidizer Y_O correspond to the stoichiometric condition when

$$\left(\frac{Y_O}{Y_F}\right)_{st} = \frac{\nu'_O W_O}{\nu'_F W_F} = s, \quad (1.2)$$

where W_O and W_F are molecular weights of oxidizer and fuel, respectively, and s is the stoichiometric ratio. The equivalence ratio ϕ is then

$$\phi = s \left(\frac{Y_F}{Y_O}\right) = \left(\frac{Y_F}{Y_O}\right) / \left(\frac{Y_F}{Y_O}\right)_{st}. \quad (1.3)$$

It can be also recast as

$$\phi = s \left(\frac{\dot{m}_F}{\dot{m}_O}\right), \quad (1.4)$$

where \dot{m}_F and \dot{m}_O are mass flow rates of fuel and oxidizer, respectively.

Let us consider each type of combustion shown schematically in Fig. 1.5. Diffusion combustion is characterised by mixing of the fuel and the oxidizer directly in the region where the combustion occurs. Mixing of reactants is the main factor that regulates the process of diffusion combustion. Combustion occurs in the limited region where the fuel and the oxidizer are close to the stoichiometric ratio. Around this zone, there are regions of rich and lean mixture. As opposed to premixed combustion, a diffusion flame cannot propagate contrary to the flow. It is easier to design equipment with diffusion combustion and they are considered to be safer. However, such combustion is less effective than the premixed combustion, since the speed of chemical reactions is limited by the speed of the mixing. In modern gas turbine engines, this combustion is usually used to stabilise the main flame and during the engine start. The main drawback of diffusion combustion is the inability to control the combustion temperature and NO_x emissions since the maximum temperature always remains in the zone of stoichiometry mixing where NO_x emissions are mainly formed. The idealised structure of a one-dimensional diffusion flame is shown in Fig. 1.6.

In contrast to a diffusion flame, during premixed combustion fuel and oxidizer are mixed before they enter the combustion region. Schematically, premixed combustion is shown in Fig. 1.7 for idealised one-dimensional combustion. It is characterised by a gas temperature increase along the abscissa from the minimum temperature of the reactants to the maximum temperature of

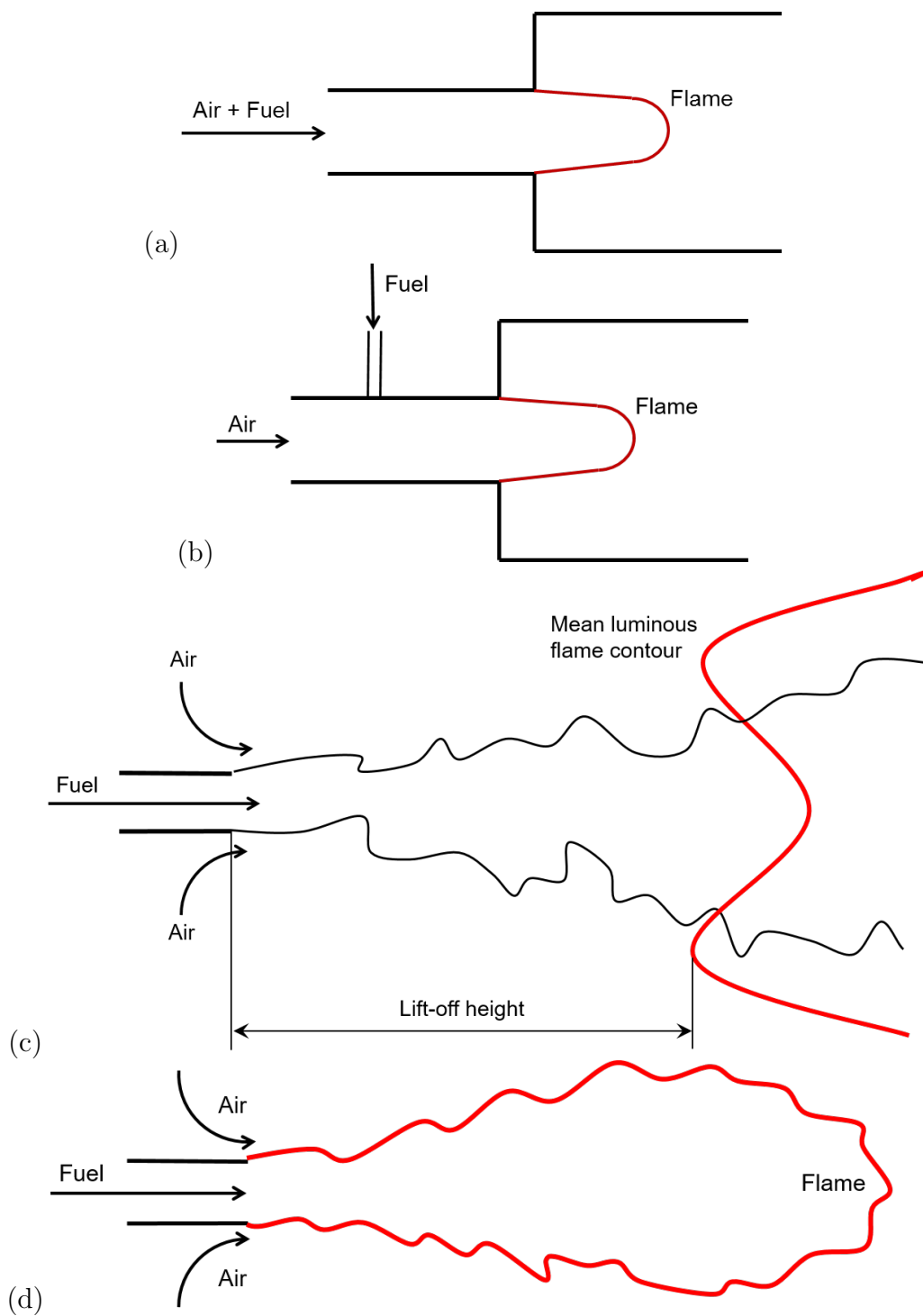


Figure 1.5: Perfectly premixed (a), technically premixed (b), partially premixed (c), and diffusion (d) flames.

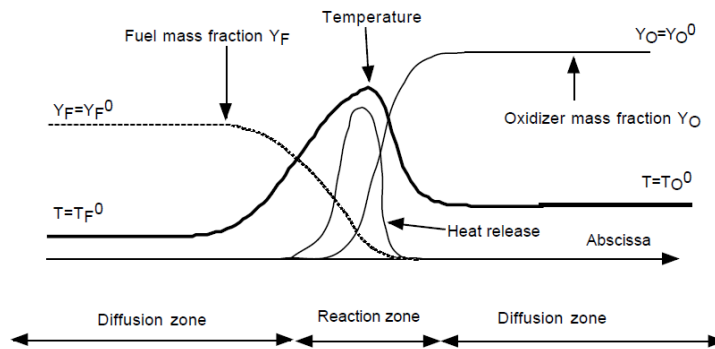


Figure 1.6: Diffusion flame structure [1].

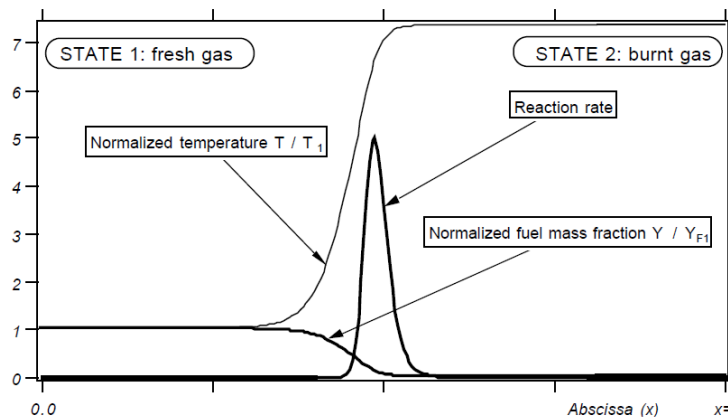


Figure 1.7: Premixed flame structure [1].

the products. A flame front defined as the region of significant temperature change consists of two main parts. In the first preliminary zone, heat and mass diffusions are most intense and chemical reactions are not yet initiated. In the reaction zone, the reaction speed rapidly increases and then decreases; in this region, chemical processes dominate on the diffusion processes. After the reaction zone, there is a zone of after-burning with negligible heat due to slow reactions occurring at the high temperatures reached in the reaction zone.

These are the principles formulated by Zeldovich, Frank-Kamenetskii and von Karman (ZFK) for the premixed flame description [17]:

- the reaction zone is located in the high-temperature zone and has the temperature close to the temperature of the combustion products;
- the thickness of the reaction zone is an order of magnitude lower than the flame front thickness for the stoichiometric mixture;
- the flame front propagates towards the reactants;

- the maximum temperature of combustion is equal to the adiabatic temperature of chemical reaction and can be estimated independently of the theory of flame propagation.

At a relatively low exit velocity a turbulent jet diffusion flame is attached to the nozzle (see Fig. 1.5(d)). When the exit velocity is increased, the flame sheet gets stretched. At certain flow velocity it is disrupted, lifts off and stabilise itself downstream the jet [18]. Such flame is called partially premixed and is schematically shown in Fig. 1.5(c).

A technically premixed flame could be considered as particular case of the perfectly premixed flame. Perfectly premixed combustion is a combustion in which fuel-oxidizer ratio in reactants mixture is unaffected by acoustic oscillations. On the contrary, fuel-oxidizer ratio is affected by eventual acoustic fluctuations in the technically premixed combustion (see Fig. 1.5). In this work setups with perfectly and technically premixed combustion are considered.

1.3 Flashback, blow-off and flame stabilisation

Machines which operate using premixed combustion are vulnerable to such undesirable phenomena as flashback and blow-off that should be avoided at the design stage.

Flashback describes the upstream propagation of a premixed flame into a region not designed for the flame to exist [4] and can occur due to several reasons:

- the flame speed exceeds the average axial flow velocity;
- flame propagation in the high-velocity core flow (see Fig. 1.8(a));
- flashback in the boundary layer (see Fig. 1.8(b));
- flashback due to combustion instabilities.

The flashback occurrence strongly depends on fuel-oxidizer composition, operating pressure and temperature, and fluid mechanics. Flashback induced by a combustion instability occurs when the instantaneous axial flow velocity decreases to low, or even negative, values during large-amplitude oscillations [19]. In fact, the flashback is often the mechanism through which combustion instabilities damage combustion systems.

The blow-off phenomenon strongly depends on the flame stabilisation technique which, thus, should be considered first. There are different techniques to stabilise the flame in high-velocity flows; the most common of them are

1. usage of pilot flames;
2. usage of bluff-body, Fig. 1.9(a);
3. sudden area increase as in Fig. 1.9(b);

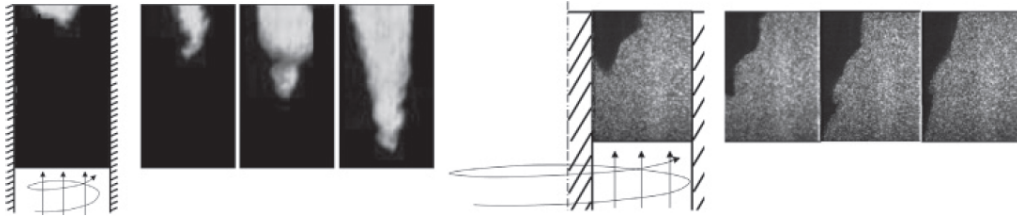


Figure 1.8: Experimental images of flame flashback in (a) core flow and (b) boundary layer. Images from (a) Kröner et al. [2] and (b) Heeger et al. [3], adapted by Lieuwen [4].

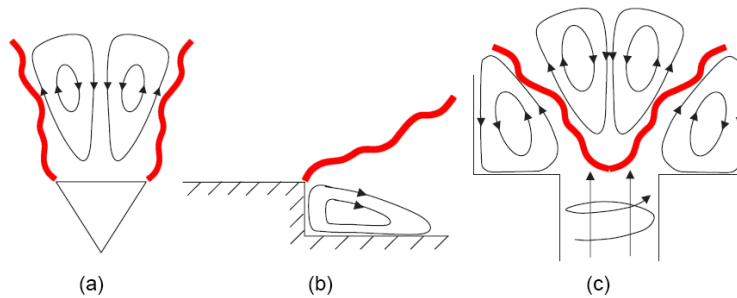


Figure 1.9: Illustration of flames stabilised by (a) a bluff body, (b) a backward-facing step, and (c) a swirling flow [4].

4. swirling the flow [20], Fig. 1.9(c).

In the second and the third case (Fig. 1.9(a), (b)), flames are stabilised in the low-velocity, high-shear regions of flow separation. In the fourth case (Fig. 1.9(c)), the flame is stabilised by a rapidly diverging jet. Basically, the flame is stabilised in the region where flame velocity and flow velocity are equal. Flames stabilised in shear layers reside in regions of very strong flow gradients and are highly stretched. In many combustors, both bluff-bodies, area increase and swirlers are used.

Three main types of swirlers - axial, diagonal and radial - are shown in Fig. 1.10. In an axial swirler the flow is supplied to the swirler in the direction of the swirler axis; scheme of axial swirler is shown in Fig. 1.10(a). The flow is supplied to the radial swirler radially; radial swirler is schematically shown in Fig. 1.10(c). Diagonal swirler has an intermediate air supply between axial and radial swirlers; it is schematically shown in Fig. 1.10(b).

Blow-off is referred to a condition under which the flame cannot be stabilised and is convected downstream by the flow [4]. It is an important issue in any practical combustion device, as it imposes fundamental operational boundaries on the combustor (see Fig. 1.11).

Determining flame stabilisation locations is also an important problem, as flames can exhibit fundamentally different shapes and lengths in situations in

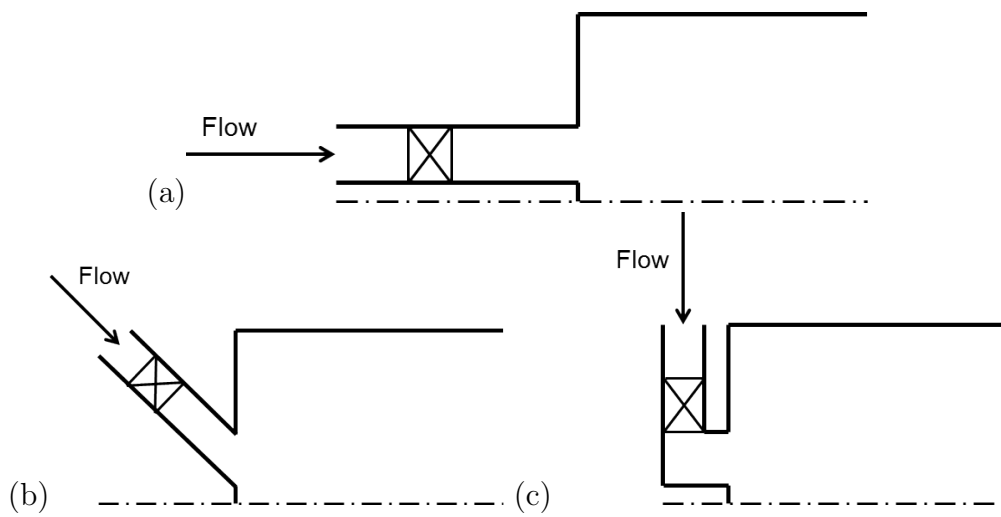


Figure 1.10: Types of flow swirlers: (a) axial, (b) diagonal, and (c) radial.



Figure 1.11: Flame blow-off in the SR-71 during a high-acceleration manoeuvre [5].

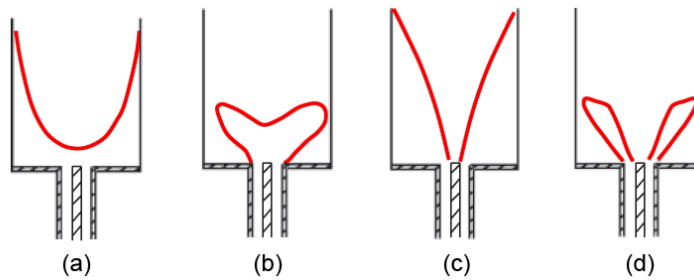


Figure 1.12: Basic flame configurations possible for an annular, swirling flow geometry [4].

which multiple stabilisation points exist. For example, Fig. 1.12 illustrates four possible premixed flame configurations in an annular, swirling combustor arrangement. In a low-velocity flow, configuration (d) is typically observed. However, the flame can exhibit one of the other three shapes if it cannot stabilise in either the inner or the outer shear layer. For example, if the flame cannot anchor in the outer shear layer, the configuration (d) will bifurcate to the configuration (c). If it cannot anchor in the inner shear layer, the configuration (c) may bifurcate to the configuration (a). These shifts in flame location can be thought of as a sequence of local blow-off events. Blow-off occurs when no stabilisation of the flame is possible.

The location/spatial distribution of the flame in a combustion chamber is a fundamental problem that has important ramifications on combustor's operation, durability, and emissions. For example, the flame location has an important influence on the stability boundary of combustion [4]. Combustor stability limits are controlled by the time delay between the creation of a fuel/air ratio disturbance (or vortex) and the moment it reaches the flame. This time delay is much longer for configurations (a) and (c) than for (b) and (d). This also illustrates that sudden changes in the combustor stability behaviour may occur when the flame abruptly bifurcates from one configuration to another.

1.4 Combustion instabilities phenomena

The history of thermoacoustic investigations dates back more than 150 years. The first thermally driven acoustic oscillations were observed by Rijke in 1859 [21]. In the experiments performed by Rijke, a vertical tube open at both ends was used. A metal wire gauze was placed in the tube at around a quarter of the tube length from its bottom. First, the gauze was heated by a flame until it became glowing red hot. After that, the flame was removed and a loud sound from the tube could be heard to last for a few seconds, before the gauze became cool [6].

The phenomena observed by Rijke was explained later as follows. Sound

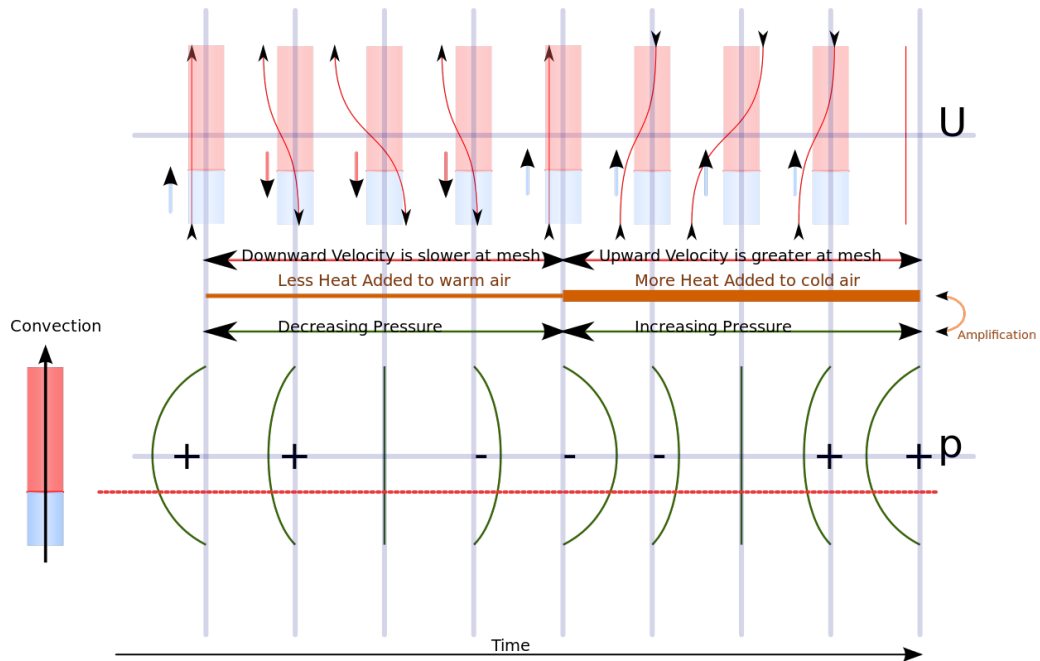


Figure 1.13: Explanation of the physical mechanism within the Rijke tube [6].

is produced by a standing wave with the half wavelength equal to the length of the tube, i.e. the fundamental frequency of the tube. The cycle of acoustic oscillations could be divided into two parts. During the first half of the period the air is pushed from both ends outside the tube, thus the pressure in the tube is decreasing (see Fig. 1.13). In particular, the air that passes through the gauze from the middle of the tube towards its bottom is already heated, thus no additional energy is supplied to the air. During the second half of the cycle, the air is pushed inside the tube from both ends, yielding an increase of the pressure in the tube. The cold air that passes from the bottom of the tube to the middle of the tube through the gauze is heated by the gauze. This makes the temperature of the air rise and, in turn, it locally increases the pressure. Because the temperature rise occurs when the pressure in the tube is increasing, additional acoustic energy is supplied to the system, maintaining acoustic oscillations.

In the 1950's the thermoacoustic phenomenon was observed in liquid propellant rocket engines [22]. At that time pressure oscillations were driven by combustion and were called combustion instabilities. These pressure oscillations could display very high amplitudes, decreasing the power of the rocket engine and sometimes even be destructive for the engine. It is difficult to understand the reason of the occurrence of combustion instabilities because of the presence of various complicated phenomena such as the hydrodynamics of the injection, the spray formation process, the transport characteristics of individual droplets, the turbulent multiphase flow conditions, and the complex

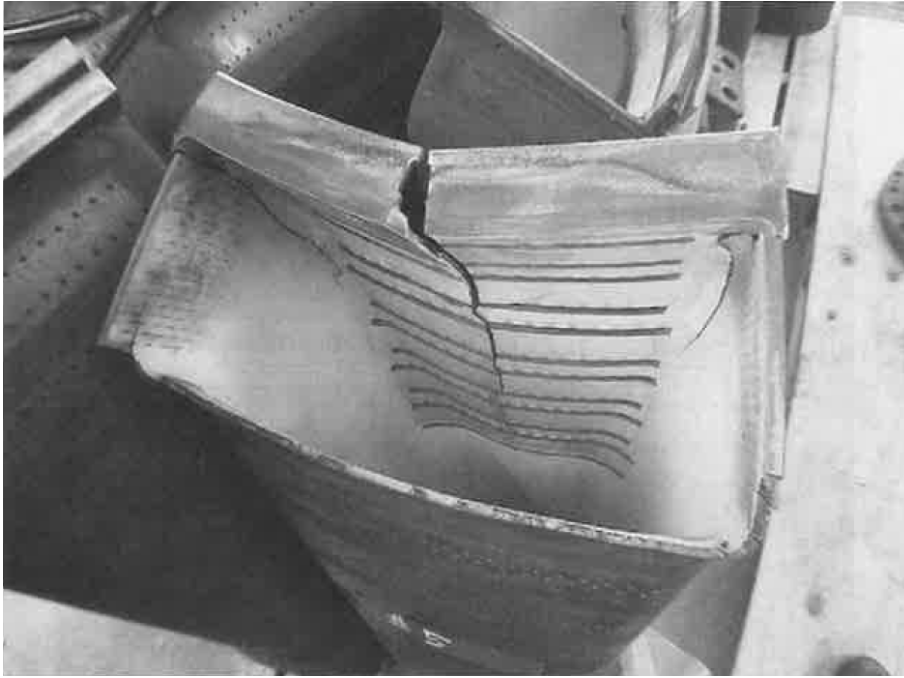


Figure 1.14: Transition piece damaged by combustion instability [7].

chemical phenomena taking place in a turbulent environment. Oefelein and Yang [23] give an extensive overview of the enormous amount of work done in the period 1962-1966 to suppress combustion instabilities in the F-1 engines installed on the Saturn-V rockets used in the US Apollo moon programme. Despite a lot of work done so far both analytically, experimentally and numerically, the thermoacoustic problem is still not fully understood and still occurs in rocket engines (see Sirignano [24]).

In the 1990's, the problem of undesirable destructive pressure oscillations arose again, this time in gas turbines. Gas turbines manufacturers were forced to reduce NOx emissions into the atmosphere. Molecules of NOx are mainly formed in gas turbines by the thermal mechanism in the high-temperature zones of combustion by the oxidation of the diatomic nitrogen in combustion air, as was shown first by Zeldovich [25] and then extended by Lavoie et al. [26]. One of the main approaches to decrease thermal NOx emissions is to lower combustion temperature by operating under lean conditions. However, gas turbines operating in the lean combustion regime are prone to combustion instabilities [27, 28]. Pressure oscillations can cause serious damage to combustion hardware, see Figs. 1.14-1.16.

It is difficult to describe the thermoacoustic problem in gas turbines combustion chambers because it involves chemical reactions, flow turbulence, heat release and propagation of acoustic waves. Combustion instabilities in gas turbines are usually seen as a coupling between unsteady combustion, acoustics of combustion chamber and turbulent flow (see Fig. 1.17). Unsteady flame heat release acts as a monopole acoustic source and produces acoustic waves. In turn, the waves influence the mass flow rate of the air-fuel mixture that



Figure 1.15: Combustion liner damaged by combustion instability [8].

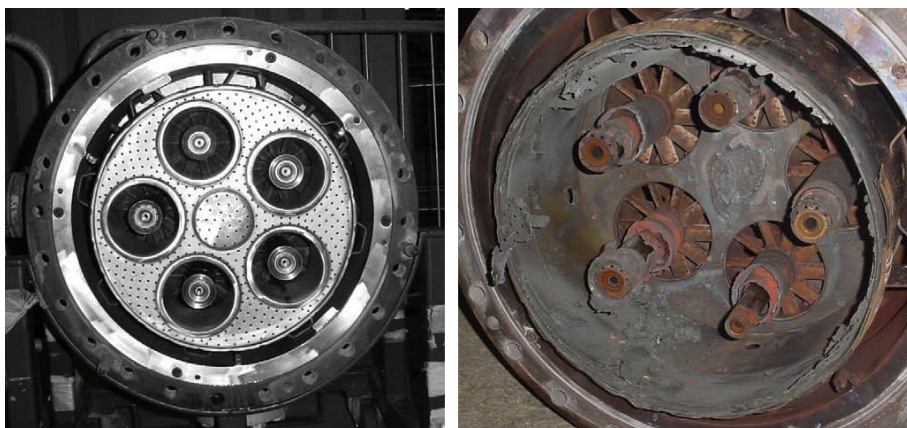


Figure 1.16: New burner assembly (left) and burner assembly damaged by combustion instability (right) [8].

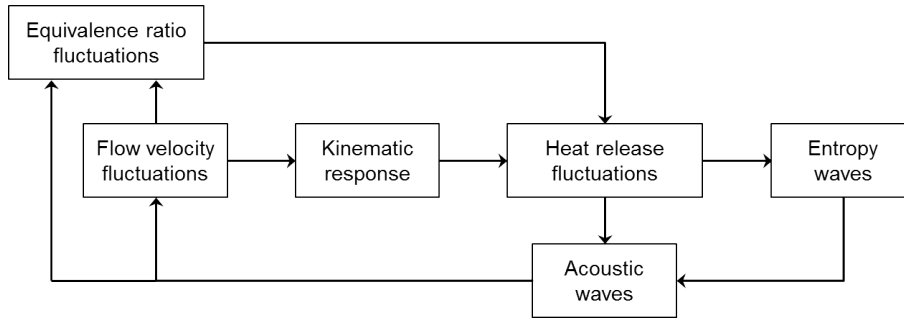


Figure 1.17: Scheme of a combustor as a thermoacoustic system.

goes to combustion and the stoichiometry of this mixture. Mass flow fluctuations themselves also contribute to perturbations of the equivalence ratio of the mixture. Equivalence ratio fluctuations and mass flow perturbations produce heat release fluctuations through the kinematic response and the loop repeats. Apart from acoustic waves, heat release oscillations produce also entropy waves that are convected to the outlet of the combustion chamber with the flow. When entropy perturbations pass through a nozzle that is typically placed at the outlet of combustor systems, they produce acoustic waves, as was noted by Marble and Candel [29].

1.5 Prediction of thermoacoustic instabilities: state of the art

There are different approaches to study combustion instabilities as well as different ways to classify these approaches. Thermoacoustic phenomena could be studied experimentally, analytically, performing numerical and semi-analytical simulations. Performing experimental thermoacoustic analysis in gas turbines requires both large expenditures for the construction of experimental test rig and operating expenses for running test campaigns. In this case, a very precise and reliable information could be obtained but the cost of the final product - the gas turbine - might be significantly augmented. So far, the completely experimental thermoacoustic analysis was applied to rocket engines used in space programmes (see Oefelein and Yang [23]). On the other hand, it is possible to perform completely analytical or semi-analytical thermoacoustic analyses, as done for example by Dowling and Stow [30]. In between, there are various numerical approaches. These approaches are usually considered to yield results close to those of the experimental analyses, but are cheaper and require fewer efforts.

CFD analysis

There are different approaches to perform complete simulations of the unsteady flame-acoustic interaction of combustion systems. This means perform-

ing unsteady Computational Fluid Dynamics (CFD) simulations of the whole thermoacoustic system. They are Unsteady Reynolds-averaged Navier-Stokes (URANS) simulations, Large Eddy Simulations (LES) and Direct Numerical Simulations (DNS) [1]. These methods differ by the range of turbulent scales that are modeled versus those that are resolved. DNS resolves the entire range of turbulent length scales, thus this method gives the highest possible precision. Using the LES technique, the smallest scales of the turbulent flow are modelled, while the largest and most important scales are resolved. In the URANS approach, all the turbulent scales are modelled, which makes it computationally the less expensive approach. The price of the DNS precision is the computational cost that depends cubically on the Reynolds number of the flow under consideration. Because of its high cost, DNS methods up to now have been applied only to simulate closed-loop combustion-acoustic interaction of laminar flames with very small computational domain [31, 32]. The LES was recently used to analyse the onset of thermoacoustic instabilities in a laboratory-scale combustor [33], a self-excited azimuthal mode in a helicopter combustion chamber [34], and transverse and radial modes in a liquid rocket engine [35]. LES methods give very good precision and continuous improvement of High-Performance Computing clusters computational capabilities will make its use more common. Nevertheless, nowadays it still remains computationally expensive. This is the reason for the use of URANS CFD calculations in this work. A detailed description of the URANS method is presented in section 2.1.1.

Decoupled analysis

Since the thermoacoustic problem is a multiscale phenomenon, in most thermoacoustic studies combined approaches are employed. This means that the analysis of turbulent reacting flow is conducted apart from the acoustic analysis, and it is done for the sake of reducing the computational time. Length scales of low-frequency acoustic oscillations, as the ones studied in this work, are often considered to be much larger than chemical and turbulent scales. This makes possible to perform simulations of turbulent combustion and acoustics separately, using different tools. This decoupling is artificial but it helps to simplify the analysis. The heat response to acoustic and stoichiometry perturbations is usually computed experimentally [36, 37, 38] or numerically [9, 39] performing unsteady analysis and is the input for the network model. Because of the high costs, difficulties and uncertainties of the experimental heat response computation [40], CFD methods are widely used now. For the acoustic analysis, either network models, Computational Acoustics (CA) or Computational Aero-Acoustics (CAA) methods are employed.

Acoustic network models

The analysis of linear waves is made easier when the cross-section dimension of the combustor is small compared with the acoustic wavelength [41]. Then, acoustic modes with variations across the cross-sectional are 'cut-off',

decaying with the axial position rather than propagating, and variations of the acoustic waves across the cross-section can be neglected. This leads to plane waves in a cylindrical combustor and axial and circumferential waves in an annular combustor. The frequencies of interest for combustion instabilities in gas turbines are sufficiently low that this is often a good approximation. Then, the linear wave equations can be solved semi-analytically by a network approach [42, 43, 44, 45]. This enables physical insight into important mechanisms. The setup is divided into a set of ducts with constant cross-section and constant thermophysical properties. Acoustic waves propagate along the ducts and are connected between neighboring ducts through transfer matrices [46]. The Green's function approach introduced by Heckl [47] is similar to the network model approach. The flame is modelled in the network model as one or as a number of compact heat sources [48]. Because of its relatively simple description, the network model approaches can be considered as semi-analytical.

Helmholtz equation, Linearized Euler Equations, and Linearized Navier-Stokes Equations

The following groups of analyses are the Computational Acoustics and Computational Aero-Acoustics methods. Both of these approaches are applicable to complex three-dimensional geometries of gas turbines combustion systems. The CA approach solves the inhomogeneous Helmholtz equation using e.g. the Finite Element Method (FEM) (see Camporeale et al. [49]). In this approach, mean flow and viscous effects on the acoustic field are neglected. In the CAA approach either the Linearized Euler Equations (LEE) [50, 51] or the Linearized Navier-Stokes Equations (LNSE) are resolved [51]. Both the LEE and the LNSE approaches take into account the mean flow. The difference between the two approaches is that LEE neglects viscous effects, while LNSE takes them into consideration. Despite its simplifications, various Helmholtz solvers are widely used in the industrial setting to forecast combustion instabilities.

Frequency-domain versus time-domain analysis

Numerical tools for thermoacoustic analysis can be divided in another way into two large groups: frequency domain analyses [49, 52] and time domain simulations [53, 54]. The first type of analysis is usually used in the linear setting, i.e. to predict whether the setup is linearly stable or not [49]. It can also be used to predict the amplitude of unstable pressure fluctuations. To accomplish this task, Silva et al. [55] propose to perform simulations for each amplitude of acoustic oscillations that is characterised by its own Flame Transfer Function (FTF). The value of acoustic oscillations amplitude that corresponds to zero growth rate is considered as the amplitude of saturated oscillations. The procedure requires performing a set of several simulations with different FTFs. On the contrary, using the time-domain analysis unstable frequencies and their amplitudes are computed straightforwardly.

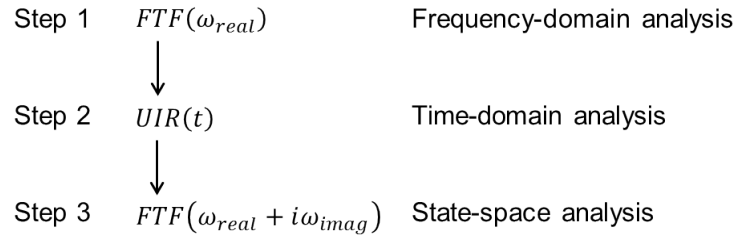


Figure 1.18: Different types of analysis [9].

Moreover, a reliable analysis in the frequency domain requires knowledge of the heat release response to acoustic and stoichiometry perturbations not only on various real but also on different imaginary frequencies. In order to calculate the FTF dependence on the real and imaginary frequencies, first the FTF dependence on the real frequencies is computed either experimentally or numerically performing periodic excitation. Then, the time-domain representation of the FTF – the Unit Impulse Response (UIR) is calculated from the FTF depending on the real frequencies (see Fig. 1.18). Another way of the UIR numerical calculation is using a broadband excitation and a Wiener-Hopf inversion for the UIR reconstruction. Afterwards, the FTF dependence on both the real and imaginary frequencies can be calculated from the UIR.

It is possible to assume that imaginary parts of complex frequencies ω_{imag} are small and perform the frequency-domain analysis taking the first $FTF(\omega_{real})$ (see Fig. 1.18). This is done for example in various numerical tools which solve Helmholtz equation. So-called state-space models [56] use the last $FTF(\omega_{real} + i\omega_{imag})$ to perform stability analysis in the frequency domain. The *taX* network model [57], the *Ta3* network model [42, 45], and the Green’s function approach [47, 58, 59] are examples of state-space model. Meanwhile, in time-domain simulations, the UIR from the second step is taken and simulations are straightforward.

Flame Transfer Function modelling

Lastly, thermoacoustic analyses can be differentiated in the way the heat release response to acoustic excitations (or excitations of equivalence ratio) is inserted either in a network model or in a CA solver.

1. The easiest way is to model the unsteady heat release as a compact element – a point in an acoustic network model or a thin sheet in a CA solver. This is usually an acceptable assumption since the flame length is much lower than the wavelength of low frequencies of interest. The FTF can be modelled with Crocco’s $n - \tau$ model [60]

$$FTF(\omega) = n(\omega)e^{-i\omega\tau(\omega)}, \quad (1.5)$$

where n is the interaction index, i is the imaginary unit, ω is the angular frequency, and τ is the time delay. This FTF representation is called

"Global FTF". Once the FTF is computed either experimentally or numerically, the dependencies of n and τ on ω are known. Then, one frequency is considered and simulations in a network model or a CA solver are performed with n and τ specific for the considered frequency to determine the stability of the thermoacoustic system at this frequency. This procedure is repeated for each frequency of interest. It is possible to use this approach both in network model [30] analysis and in CA/CAA analyses [61]. Despite its simplicity, the drawback of this method is the requirement of performing a large number of simulations.

2. Kim et al. [48] proposed to use several unsteady heat releases in the network model. For this objective they divided the flame zone in several sections and measured the interaction index n and the time delay τ (see Eq. 1.5) for each zone for the frequencies of interest. Then, unsteady heat release is presented in the network model as the set of compact elements each with its own $n(\omega)$ and $\tau(\omega)$. This FTF representation is called "Local FTFs". Kim et al. [48] reported that they had obtained better agreement of the experimental data with the local FTFs than with the global FTF when the flame length had been larger than 10% of the wavelength of the unstable acoustic mode. When the flame was within 10% of the wavelength of the acoustic mode, the usage of the local FTFs and the global FTF gave the same result [48].
3. An approach similar to the previous one was implemented in CA solvers by various researchers [52, 62, 13]. The idea is to obtain the distribution of the fluid particle flight time from the fuel injection point to different points at the flame from CFD calculations. The last is assumed to be the spatial distribution of the time lag τ in Eq. 1.5. The distribution of the interaction index n is assumed to be proportional to the distribution of the unperturbed heat release distribution. In this way two things are considered: the acoustic non-compactness of the flame and the fact that different points of the flame respond to excitation with different time delays. In this approach n and τ do not depend on frequency. Up to now, applications of this approach took into account only one driving mechanism of heat release oscillations – the response to equivalence ratio excitations. Considering also another driving mechanisms would improve the stability prediction.
4. When the flame is acoustically compact for the studied frequencies, the previous approach can be also translated into the network model approach. This implies that the flame is considered in the network model as a compact element but the FTF model takes into account different flight times to different flame points [63, 64, 65, 38]. n and τ do not depend on frequency in this approach as well. This approach of the FTF modelling has several advantages with respect to the first two approaches: the number of simulations is reduced and since the model parameters have physical meaning, their change with increasing the excitation amplitude can be traced and explained.

The very brief description of the used method

As it can be seen, there is a large variety of approaches to investigate combustion instabilities in gas turbines. To start investigating these phenomena, first, the approach and tools that best fit certain needs have to be determined. In this work combustion instabilities in a laboratory and an industrial setups are investigated. The heat release response to acoustic oscillation is computed performing URANS simulations since they give reasonable precision at low frequencies of excitation and are faster than LES, all important reasons from the industrial point of view. Excitation in a broad range of frequencies is done at different amplitudes. The computed FDFs are approximated with appropriate distributed time-lags models. In both setups under investigation, the cross-section dimension is small compared to the acoustic wavelength. Thus, a network model is used to study closed-loop combustion-acoustic interaction at low frequencies. There are a lot of works that perform thermoacoustic analysis in frequency domain using network models. There are much less works that perform time-domain simulations. Some of them are concentrated on simple thermoacoustic systems such as Rijke tube [54, 66], some are applied to more complicated laboratory setups [67, 68, 69], and some to industrial test rigs [70]. Mean flow is taken into account in the network model. Both unstable frequencies of pressure perturbations and their amplitudes are calculated. The approach used in this work consists of three parts, thus it is called three-step approach.

1.6 Structure of the work

The thesis is organised as follows. The second chapter gives details on the three-step approach. Overview of URANS method is given in section 2.1.1. Description of the used Flame Speed Closure model is represented in section 2.1.2. Numerical determination of the FTF is explained in section 2.1.3. Sections 2.2.1 and 2.2.2 explain the physical meaning of parameters in distributed time-lags models for perfectly premixed and technically premixed flames respectively. Section 2.3 describes the one-dimensional network model used in this work.

The three-step approach is applied to a laboratory test rig with a perfectly premixed flame in chapter 3. Description of the setup is given in section 3.1. The Flame Describing Function of the test rig is computed in section 3.2 and is then approximated in section 3.3 with two analytical models. Particularly, the presented in literature distributed time-lag FTF model is extended to the nonlinear regime, introducing a dependence of the model parameters on the amplitude of excitation. The network model of the laboratory test rig is presented in section 3.4.1. Results of linear simulations are presented in section 3.4.2. Various parametric analyses are performed in this section in order to find the ways to suppress acoustic modes associated with the flame. Section 3.4.3 gives results of the weakly non-linear analysis. The main outcome of this section is that the frequency of the acoustic mode associated with the

flame strongly depends on the amplitude of the oscillations. The conclusions of chapter 3 are discussed in section 3.5.

In chapter 4, the three-step approach is utilised to perform thermoacoustic analysis of an industrial test rig with a technically premixed flame. The experimental setup is discussed in section 4.1. The overview of a reference LES study is given in section 4.2. Section 4.3 presents the results of URANS simulations. In particular, the results of the unperturbed simulations are presented and discussed in section 4.3.2 and the FDF computed with URANS is presented and discussed in section 4.3.3. Time-lag distributed models of the FTFs computed with LES and URANS are presented in section 4.4.1. Two models of the FDF computed with URANS are presented in sections 4.4.2 and 4.4.3. Two FDF models based on the FTF computed with LES and the two FDF models from sections 4.4.2 and 4.4.3 are presented in sections 4.4.4 and 4.4.5, respectively. The hybrid FDF based on the LES FTF model and the FDF model of the laboratory test rig is presented in section 4.4.6. Stability analysis of the industrial test rig is conducted with the help of network model in section 4.5. Results of linear analysis of the test rig are presented in section 4.5.2 and of the weakly nonlinear analysis – in section 4.5.3. The conclusions of the thermoacoustic investigation of the industrial test rig are presented in section 4.6.

The conclusions of the present work and indications for future investigations are presented in chapter 5.

Chapter 2

Description of the three-step approach for prediction of combustion instabilities in gas turbines

Several of thermoacoustic systems have a longitudinal dimension larger than the dimensions along the other directions. Acoustic study of these systems can be concentrated only on longitudinal acoustic waves. An acoustic network model is an optimum approach to study the excitation of these waves by unsteady combustion because it is fast and accurate [43].

In order to perform closed-loop thermoacoustic analysis with a network model, it is necessary to know the flame response to flow perturbations. To compute the latter, unsteady CFD simulations could be run. The computed flame response to being used in the network model must be preliminarily validated with an appropriate model.

In this work, a three-step approach for the prediction of combustion instabilities is proposed. The first step is to compute the flame response to flow excitations performing URANS simulations with the Flame Speed Closure model. Justification of using this model is given in section 2.1. The second step is to approximate the calculated flame response with a time-lag-distributed model. The necessity and rationalisation of using this model are explained in section 2.2. The network model approach is introduced in section 2.3.

2.1 FDF computation with CFD simulations

The combustion process in gas turbines is a complicated phenomenon that includes flow turbulence, chemical reactions and heat release. There are three main approaches to investigate numerically the dynamics of turbulent flows:

1. Direct Numerical Simulations (DNS),
2. Large Eddy Simulations (LES),

3. Unsteady Reynolds-Averaged Navier-Stokes (URANS) simulations.

These three approaches differ by the range of turbulence scales that are resolved and modelled. In the DNS approach all spatial scales from the smallest Kolmogorov scale [71] up to the largest integral scale are resolved [72]. In the LES approach, the largest spatial scales that contain more energy are resolved, while the smallest and the most computationally expensive to resolve space scales are modelled [73]. An overview of LES application to combustion modelling is presented by Pitsch [74]. The URANS approach is the less computationally expensive one because all scales of turbulence are modelled. This makes the URANS approach preferable from an industrial point of view.

The simplest way to model heat release due to combustion is the Arrhenius approach described, e.g. by Poinot and Veynante [1]. It completely neglects the influence of turbulence on combustion. This approach can be used only when chemical time scales are much larger than the turbulent time scales. It could be applied to supersonic combustion but is not suitable for turbulent combustion in gas turbines.

The Eddy Break-Up (EBU) model proposed by Spalding [75], as opposed to the Arrhenius approach, assumes that turbulent combustion is mainly governed by turbulent mixing but not by the chemistry. The justification of such assumption is that chemical reactions happen very fast compared to turbulent mixing. The EBU model assumes that combustion is completed at the moment of mixing. This assumption makes this model suitable for the diffusion-driven combustion but not for premixed combustion. To overcome this limitation, the EBU model was coupled with the Arrhenius approach by Magnussen and Hjertager [76]. The combined approach is often called Eddy Dissipation Model (EDM).

Another model is the Flamelet Generated Manifold (FGM) model proposed by van Oijen and de Goey [77]. In this approach, chemistry is incorporated into the turbulent heat release through probability density functions. The weak point of this model is that the parameters of the used probability density functions are quite vague, as noticed in the comments provided by Bilger to the work of Peters [78] (the Bilger's comments can be found at the end of the Peter's article).

Another family of models uses turbulent flame speed to close the heat release problem [79, 80, 81]. In these models, chemical calculations are enclosed in laminar flame speed that is pre-computed with respect to CFD calculations. These models are physically reasonable among the models that do not require high CPU costs. The turbulent flame speed is represented through a laminar flame speed and turbulent quantities. These models are simple, robust, and have been extensively tested versus various experimental data. These models were successfully used for prediction not only of steady flames [82] but also for flame dynamics [36, 9, 83].

2.1.1 Overview of URANS method

The numerical tool employed is OpenFOAM version 2.3.0 [84] developed by Weller et al. [85]. The equations in this section are written in the way they are implemented in OpenFOAM. These equations are solved in OpenFOAM using Finite Volume Method (FVM) [86].

Averaged governing equations

In the URANS approach any quantity f (velocity, pressure, enthalpy, etc.) is represented as the sum of its mean component \bar{f} and fluctuating part f' :

$$f = \bar{f} + f'. \quad (2.1)$$

Since combustion simulations deal with flows with different density, mass-weighted averages (or Favre averages [87]) quantities are used instead of Reynolds averaged quantities [1]:

$$\tilde{f} = \frac{\overline{\rho f}}{\bar{\rho}}, \quad (2.2)$$

where $\bar{\rho}$ is the mean density. Any quantity is then split as

$$f = \tilde{f} + f'', \quad (2.3)$$

where $\widetilde{f''} = 0$.

The equations to be solved are Favre-averaged equations of conservation of mass, momentum and enthalpy

$$\frac{\partial \bar{\rho}}{\partial t} + \frac{\partial}{\partial x_i}(\bar{\rho} \tilde{u}_i) = 0, \quad (2.4)$$

$$\frac{\partial \bar{\rho} \tilde{u}_i}{\partial t} + \frac{\partial}{\partial x_i}(\bar{\rho} \tilde{u}_i \tilde{u}_j) = -\frac{\partial \bar{p}}{\partial x_j} + \frac{\partial}{\partial x_i} \left(\bar{\sigma}_{i,j} - \bar{\rho} \widetilde{u_i'' u_j''} \right), \quad (2.5)$$

$$\frac{\partial \bar{\rho} \tilde{h}}{\partial t} + \frac{\partial}{\partial x_i}(\bar{\rho} \tilde{u}_i \tilde{h}) + \frac{\partial \bar{\rho} \tilde{K}}{\partial t} + \frac{\partial}{\partial x_i}(\bar{\rho} \tilde{u}_i \tilde{K}) = \frac{\partial \bar{p}}{\partial t} - \frac{\partial}{\partial x_i} \left(\bar{q} + \bar{\rho} \widetilde{u_i'' h''} \right), \quad (2.6)$$

where the averaged enthalpy \tilde{h} is the sum of sensible enthalpy and chemical enthalpy of formation. Thus, no source term due to chemical reaction is needed in Eq. 2.6. \tilde{K} in Eq. 2.6 is the averaged kinetic energy $\tilde{K} = 0.5 \tilde{u}_i \tilde{u}_i$.

The viscous stress tensor $\bar{\sigma}_{ij}$ is defined as

$$\bar{\sigma}_{ij} = \tilde{\mu} \left(2\tilde{S}_{ij} - \frac{2}{3} \frac{\partial \tilde{u}_k}{\partial x_k} \delta_{ij} \right), \quad (2.7)$$

with δ_{ij} the Kronecker index, $\tilde{\mu} = \bar{\rho} \tilde{\nu}$ the mean dynamic viscosity, $\tilde{\nu}$ the mean kinematic viscosity, and the Favre-averaged strain-rate tensor \tilde{S}_{ij} defined as

$$\tilde{S}_{ij} = \frac{1}{2} \left(\frac{\partial \tilde{u}_i}{\partial x_j} + \frac{\partial \tilde{u}_j}{\partial x_i} \right). \quad (2.8)$$

Reynolds stresses $\widetilde{\rho u_i'' u_j''}$ in this work are closed with the *SST* $k - \omega$ turbulence model described below.

The averaged heat flux is represented in the form

$$\bar{q} = -\lambda \frac{\partial T}{\partial x_i} = -\tilde{\lambda} \frac{\partial \tilde{T}}{\partial x_i} = -\frac{\tilde{\mu}}{Pr} \frac{\partial \tilde{h}}{\partial x_i}, \quad (2.9)$$

where $\tilde{\lambda}$ is the mean thermal conductivity and Pr is the Prandtl number $Pr = \frac{\tilde{\nu}}{\tilde{a}}$ with \tilde{a} the mean thermal diffusivity, $\tilde{a} = \frac{\tilde{\lambda}}{\tilde{\rho} \tilde{c}_p}$ with \tilde{c}_p the mean specific heat capacity at constant pressure.

The turbulent heat flux $\widetilde{\rho u_i'' h''}$ is modelled using gradient assumption

$$\widetilde{\rho u_i'' h''} = -\frac{\mu_t}{Pr_t} \frac{\partial \tilde{h}}{\partial x_i}, \quad (2.10)$$

where μ_t is the turbulent viscosity computed with a turbulence model, and Pr_t is the turbulent Prandtl number defined by $Pr_t = \frac{\tilde{\mu}_t}{\tilde{\rho} \tilde{a}_t}$ with \tilde{a}_t the turbulent thermal diffusivity.

SST $k - \omega$ turbulence model

The *SST* $k - \omega$ is a linear eddy viscosity turbulence model developed by Menter [88, 89]. This model blends the freestream independence of the $k - \epsilon$ model [90, 91] with the robust and accurate turbulence treatment in the near wall region of the Wilcox $k - \omega$ model [92]. In the *SST* $k - \omega$ turbulence model the Reynolds stresses $\widetilde{\rho u_i'' u_j''}$ are modelled using the Boussinesq assumption:

$$-\widetilde{\rho u_i'' u_j''} = \tau_{ij} = \mu_t \left(2\tilde{S}_{ij} + \frac{2}{3}\delta_{ij} \frac{\partial \tilde{u}_k}{\partial x_k} \right) - \frac{2}{3}\tilde{\rho} k \delta_{ij}, \quad (2.11)$$

where k is the Turbulent Kinetic Energy (TKE) defined as

$$k = \frac{1}{2} \sum_{i=1}^3 \widetilde{u_i'' u_i''}. \quad (2.12)$$

The turbulent viscosity is found by solving the transport equation for the TKE, k , and the Specific Dissipation Rate (SDR) ω :

$$\frac{\partial(\tilde{\rho}k)}{\partial t} + \frac{\partial(\tilde{\rho} \tilde{u}_i k)}{\partial x_i} = \tilde{P} - \beta^* \tilde{\rho} k \omega + \frac{\partial}{\partial x_i} \left[(\tilde{\mu} + \sigma_k \mu_t) \frac{\partial k}{\partial x_i} \right], \quad (2.13)$$

$$\frac{\partial(\tilde{\rho}\omega)}{\partial t} + \frac{\partial(\tilde{\rho} \tilde{u}_i \omega)}{\partial x_i} = \frac{\gamma \tilde{\rho}}{\mu_t} \tilde{P} - \beta \tilde{\rho} \omega^2 + \frac{\partial}{\partial x_i} \left[(\tilde{\mu} + \sigma_\omega \mu_t) \frac{\partial \omega}{\partial x_i} \right] + 2(1-F_1) \frac{\tilde{\rho} \sigma_{\omega 2}}{\omega} \frac{\partial k}{\partial x_i} \frac{\partial \omega}{\partial x_i}, \quad (2.14)$$

Table 2.1: Constants of the *SST* $k - \omega$ model.

i	σ_{ki}	$\sigma_{\omega i}$	γ_i	β_i
1	0.85	0.5	5/9	0.075
2	1.0	0.856	0.44	0.0828

where the blending function F_1 is defined as

$$F_1 = \tanh \left(\left\{ \min \left[\max \left(\frac{\sqrt{k}}{\beta^* \omega y}, \frac{500\nu}{y^2 \omega} \right), \frac{4\bar{\rho}\sigma_{\omega 2}k}{CD_{k\omega}y^2} \right] \right\}^4 \right), \quad (2.15)$$

where y is the distance to the nearest wall and $CD_{k\omega}$ is calculated as

$$CD_{k\omega} = \max \left(2\bar{\rho}\sigma_{\omega 2} \frac{1}{\omega} \frac{\partial k}{\partial x_i} \frac{\partial \omega}{\partial x_i}, 10^{-10} \right); \quad (2.16)$$

the constant β^* in Eqs. 2.13-2.15 is equal to 0.09. The other constants σ_{ki} , $\sigma_{\omega i}$, γ_i , and β_i in Eqs. 2.13-2.16 defined in general as ϕ are calculated from constants ϕ_1 and ϕ_2 as

$$\phi = \phi_1 + (1 - F_1)\phi_2, \quad (2.17)$$

with ϕ_1 and ϕ_2 given in Tab. 2.1.

Finally, the turbulent viscosity is computed as

$$\tilde{\mu}_t = \frac{0.31\bar{\rho}k}{\max(0.31\omega, SF_2)}, \quad (2.18)$$

where S is the invariant measure of the strain $S = \sqrt{2\tilde{S}_{ij}\tilde{S}_{ji}}$ and F_2 is a second blending function:

$$F_2 = \tanh \left\{ \left[\max \left(\frac{2\sqrt{k}}{\beta^* \omega y}, \frac{500\nu}{y^2 \omega} \right) \right]^2 \right\}. \quad (2.19)$$

A production limiter is used in the *SST* $k - \omega$ turbulence model to prevent the build-up of turbulence in stagnation regions

$$\tilde{P} = \min(P, 10\beta^* \bar{\rho}k\omega), \quad (2.20)$$

with

$$P = \tau_{ij} \frac{\partial \tilde{u}_i}{\partial x_j}. \quad (2.21)$$

Near wall treatment

The following conditions are used for TKE, SDR and the turbulent viscosity at the walls. The TKE at the walls is set to zero:

$$k_w = 0. \quad (2.22)$$

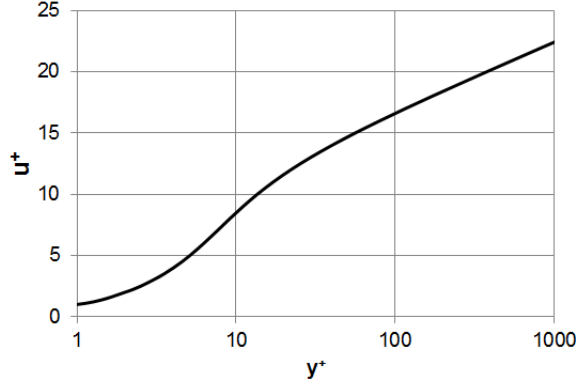


Figure 2.1: Law of the wall modelled with Eq. 2.26.

One of the benefits of using a turbulence model of the $k - \omega$ family, in particular the *SST* $k - \omega$ turbulence model, is the possibility of using scalable wall functions. Such approach automatically switches from a low-Reynolds number formulation to a wall function treatment, depending on grid density [93]

$$\omega = \sqrt{\omega_{vis}^2 + \omega_{log}^2}, \quad (2.23)$$

where ω_{vis} and ω_{log} are solutions for ω in the viscous and the logarithmic near-wall regions, respectively, and are calculated as follows [84]:

$$\omega_{vis} = \frac{6\tilde{\mu}}{\bar{\rho}\beta_1 y^2}, \quad (2.24)$$

$$\omega_{log} = \frac{\sqrt{k}}{C_\mu^{0.25} \kappa y}, \quad (2.25)$$

where $\beta_1 = 0.075$, $C_\mu = 0.09$ and $\kappa = 0.41$ are model constants.

The boundary condition for the turbulent viscosity μ_t provides a condition, based on velocity, using Spalding's law to give a continuous μ_t profile to the wall. This boundary condition is a generic wall function that uses field of velocity u instead of TKE k and ensures that a general law for the velocity shown in Fig. 2.1 is fulfilled:

$$y^+ = u^+ + \frac{1}{E} \left[\exp(\kappa u^+) - 1 - \kappa u^+ - 0.5(\kappa u^+)^2 - \frac{1}{6}(\kappa u^+)^3 \right], \quad (2.26)$$

where $E = 9.8$ is a constant, y^+ and u^+ are dimensionless distance from the cell centre to the wall and the dimensionless velocity, calculated as follows

$$y^+ = \frac{y u_\tau \bar{\rho}}{\tilde{\mu}}, \quad (2.27)$$

$$u^+ = \frac{\tilde{u}}{u_\tau}, \quad (2.28)$$

where u_τ is the friction velocity defined as

$$u_\tau = \sqrt{\frac{\tau_w}{\bar{\rho}}}, \quad (2.29)$$

and τ_w is the shear stress at the wall:

$$\tau_w = (\mu_t + \mu) \left| \frac{\partial \tilde{u}}{\partial n} \right|. \quad (2.30)$$

2.1.2 FSC model description

In order to model the behaviour of the flame, we apply the Flame Speed Closure (FSC) model, proposed by Lipatnikov and Chomiak [81]. Comparing to the Turbulent Flame Closure (TFC) model developed by Karpov et al. [80], the FSC model describes the propagation of the flame not only in the case of fully developed turbulence but also in the limit case of the absence of turbulence. Moreover, the FSC model takes into account that the turbulent diffusivity and the turbulent flame speed depend on the time delay which occurs when a fluid particle travels from the burner exit plane to the combustion zone. The key variable in the FSC model is the progress variable b , also referred to as normalised fuel mass fraction or normalised temperature; this is defined by

$$b = \frac{T_b - T}{T_b - T_u}, \quad (2.31)$$

where T is the temperature at the current point, T_b and T_u are the temperatures of the burnt and unburnt gas, respectively. Thus, $b = 1$ in regions of unburnt gas and $b = 0$ in regions of burnt gas. The progress variable propagation is governed by the transport equation:

$$\begin{aligned} \frac{\partial \bar{\rho} \tilde{b}}{\partial t} + \nabla \cdot (\bar{\rho} \tilde{u} \tilde{b}) - \nabla \cdot [\bar{\rho} (D + D_{t,t}) \nabla \tilde{b}] = \\ = - \frac{S_{L,0}^2}{4(D + D_{t,t})} \rho_u (1 - \tilde{b}) \tilde{b} - \rho_u S_{t,t} |\nabla \tilde{b}|, \end{aligned} \quad (2.32)$$

where D is the molecular diffusivity, ρ_u is the density of the unburnt gas, and $S_{L,0}$ is the unperturbed laminar flame speed. $D_{t,t}$ and $S_{t,t}$ are variants of the turbulent diffusion coefficient and the turbulent flame velocity, respectively. They are characterised by their dependence on the time t_{fd} a fluid particle takes to travel from the burner exit plane to the current axial position x ,

$$t_{fd} = \frac{x - x_{fh}}{u_{FSC}}, \quad (2.33)$$

where x_{fh} is the position of the burner exit plane (flame holder), and u_{FSC} is the axial flow velocity area-averaged over the burner exit plane at x_{fh} .

The time-dependent coefficient of turbulent diffusion is calculated from

$$D_{t,t} = D_t [1 - \exp(-t_{fd}/t_L)], \quad (2.34)$$

where D_t is the coefficient of turbulent diffusion, and t_L is the Lagrangian time scale of turbulence. D_t is given by $D_t = \mu_t/(\rho Sc_t)$, where Sc_t is the turbulent Schmidt number. Authors of the model [81] suggest to take $Sc_t = 0.3$. Such low value aims to increase the diffusion of the flame far from the flame holder, meanwhile the multiplier $[1 - \exp(-t_{fd}/t_L)]$ in Eq. 2.34 decreases the diffusion close to the flame holder [94]; t_L is given by $t_L = D_t/(u'_{turb})^2$, where u'_{turb} is the root-mean-square of the turbulent velocity fluctuations.

The time-dependent turbulent flame velocity is calculated from

$$S_{t,t} = S_t \left\{ 1 + \frac{t_L}{t_{fd}} \left[\exp(-t_{fd}/t_L) - 1 \right] \right\}^{0.5}, \quad (2.35)$$

where S_t is the turbulent flame speed, given by

$$S_t = 0.52(u'_{turb})^{0.75} S_{L,0}^{0.5} a_u^{-0.25} l_t^{0.25}, \quad (2.36)$$

where a_u is the thermal diffusivity of the unburnt mixture and l_t is the turbulence length scale given by

$$l_t = C_D \frac{(u'_{turb})^3}{\epsilon}, \quad (2.37)$$

where C_D is the model dimensionless constant and ϵ is the turbulence dissipation rate. The authors of model [81] suggest the value for the constant $C_D = 0.3$.

In case of perfectly premixed flame any thermophysical quantity of the mixture (enthalpy, heat capacity, viscosity, density) denoted by ψ can be calculated through corresponding quantities of reactants and combustion products as

$$\psi_{mix} = \frac{\tilde{b}}{W_R} \psi_R + \frac{1 - \tilde{b}}{W_P} \psi_P, \quad (2.38)$$

where W is the molecular weight, R denotes reactants, and P denotes combustion products.

For technically-premixed flame the additional transport equation for the mixture fraction \tilde{f}_t is solved

$$\frac{\partial \tilde{\rho} \tilde{f}_t}{\partial t} + \nabla \cdot (\tilde{\rho} \tilde{u} \tilde{f}_t) - \nabla \cdot \left[\tilde{\rho} (D + D_t) \nabla \tilde{f}_t \right] = 0. \quad (2.39)$$

The mixture mass fraction of fuel, oxidizer and combustion products are calculated as

$$\tilde{Y}_F = \tilde{b} \tilde{f}_t + (1 - \tilde{b}) \max \left(\tilde{f}_t - \frac{1 - \tilde{f}_t}{s}, 0 \right), \quad (2.40)$$

$$\tilde{Y}_O = 1 - \tilde{f}_t - (\tilde{f}_t - \tilde{Y}_F) s, \quad (2.41)$$

$$\tilde{Y}_P = 1 - \tilde{Y}_F - \tilde{Y}_O, \quad (2.42)$$

where s is the stoichiometric ratio defined by Eq. 1.2. In case of technically premixed flame any thermophysical quantity of the mixture (enthalpy, heat capacity, viscosity, density) denoted by ψ can be calculated through corresponding quantities of fuel, oxidizer, and combustion products as

$$\psi_{mix} = \frac{\tilde{Y}_F}{W_F} \psi_F + \frac{\tilde{Y}_O}{W_O} \psi_O + \frac{\tilde{Y}_P}{W_P} \psi_P. \quad (2.43)$$

I have implemented the FSC model into the solver *XiFoam* of OpenFOAM 2.3.0, which is a solver for the simulation of compressible premixed/technically-premixed combustion and which includes turbulence modelling. It uses the compressible PIMPLE algorithm, which combines the algorithm of the PISO (Pressure-Implicit Split-Operator) and the SIMPLE (Semi-Implicit Method for Pressure-Linked Equations) algorithms.

The heat release rate in a particular cell, denoted here by ΔQ , is proportional to the right-hand-side of Eq. 2.32,

$$\Delta Q = Y_F H_R \left[\frac{S_{L,0}^2}{4(D + D_{t,t})} \rho_u (1 - \tilde{b}) \tilde{b} + \rho_u S_{t,t} |\nabla \tilde{b}| \right], \quad (2.44)$$

where H_R is the lower heating value of the fuel. For the purpose of calculating the FTF or FDF, the volume integral of ΔQ over the whole domain is calculated.

2.1.3 Numerical determination of the FTF and FDF

The dynamic response of a flame to a flow perturbation can be represented in the frequency domain by its *Flame Transfer Function* (FTF), defined by

$$FTF(\omega) = \frac{\hat{Q}(\omega)/\bar{Q}}{\hat{u}_r(\omega)/\bar{u}_r}; \quad (2.45)$$

this is the ratio between heat release rate fluctuations $\hat{Q}(\omega)$ (normalised with the mean heat release rate \bar{Q}) and the velocity fluctuation $\hat{u}_r(\omega)$ at a reference position x_r upstream of the flame (normalised with the mean velocity \bar{u}_r).

In general, heat release oscillations could be caused by equivalence ratio fluctuations, as shown in Fig. 1.17. It will be shown in section 2.2 that for the gas turbines investigated in this work it is reasonable to assume that equivalence ratio fluctuations depend only on velocity fluctuations.

The FTF is a linear concept. It can be extended into the nonlinear domain by measuring the FTF spectrum for several velocity amplitudes, thus creating a family of curves along the frequency axis. This is called the *Flame Describing Function* (FDF),

$$FDF(\omega, A) = \frac{\hat{Q}(\omega, A)/\bar{Q}}{\hat{u}_r(\omega, A)/\bar{u}_r}, \quad (2.46)$$

where A is the velocity amplitude. The FDF has been shown by several researchers, notably by Noiray et al. [95] to be a versatile tool for modelling nonlinear effects, such as limit cycle oscillations.

In principle, the FTF can be computed for a given combustion system by imposing a harmonic velocity perturbation, measuring the resulting heat release rate and calculating the ratio of relative Fourier transforms (see Eq. 2.45). This procedure should be repeated for each frequency of interest. However, this is time-consuming taking into account wide range of frequencies of interest. Assuming that the combustion system is linear time invariant, it is possible to compute the FTF with just one simulation. This is done by exciting the velocity with a broadband signal and calculating the correlation between the velocity at the reference point and the heat release. This method is called Wiener-Hopf inversion and was initially applied to thermoacoustic systems by Polifke et al. [96].

The CFD simulations give us discrete time series of the velocity u_r (at a reference position) and of the global rate of heat release Q of the flame:

$$u_r(t_0), u_r(t_1), u_r(t_2), \dots, u_r(t_N), \quad (2.47a)$$

$$Q(t_0), Q(t_1), Q(t_2), \dots, Q(t_N), \quad (2.47b)$$

where $t_n = n\Delta t$ ($n = 0, 1, \dots, N$) are the discrete times at which results for u_r and Q are available. These results include both the mean part (denoted by over-bar) and the perturbation (denoted by prime),

$$u_r(t) = \bar{u}_r + u_r'(t) \quad (2.48a)$$

$$Q(t) = \bar{Q} + Q'(t). \quad (2.48b)$$

The aim is to determine the FTF from this data. This is done in a 4-step approach, following [96].

Step 1: Calculation of the mean and perturbation quantities.

The mean values are first calculated as averages over the time series,

$$\bar{u}_r = \frac{1}{N+1} \sum_{n=0}^N u_r(t_n) \quad (2.49a)$$

$$\bar{Q} = \frac{1}{N+1} \sum_{n=0}^N Q(t_n), \quad (2.49b)$$

and then obtain the perturbation quantities from

$$u_r'(t_n) = u_r(t_n) - \bar{u}_r \quad (2.50a)$$

$$Q'(t_n) = Q(t_n) - \bar{Q} \quad (2.50b)$$

In order to keep the notation simple, $u_r'(t_n)$ and $Q'(t_n)$ are abbreviated by u_n and Q_n .

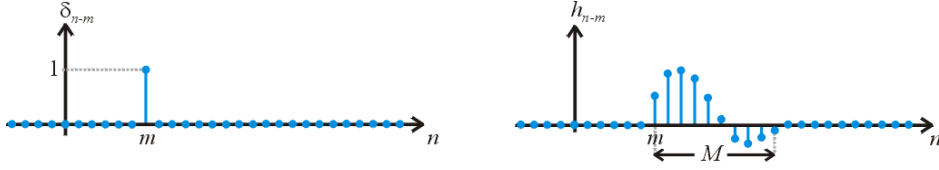


Figure 2.2: Unit impulse (left) and causal, finite-duration response (right).

Step 2: Representation in terms of concepts from the digital signal processing.

In the digital signal processing, the unit impulse is defined by

$$\delta_{n-m} = \begin{cases} 1 & \text{if } n = m \\ 0 & \text{if } n \neq m \end{cases} \quad (2.51)$$

The flame is treated as a single-input single-output system and denote the response to δ_{n-m} by h_{n-m} ; h is called the unit impulse response (UIR, or Green's function in mathematics terminology). δ and h can be used as building blocks to represent any input and output signal in terms of a convolution. For the flame, the velocity (input) can be written as

$$u_n = u_0\delta_n + u_1\delta_{n-1} + \dots + u_N\delta_{n-N} \quad (2.52)$$

and the heat release (output) as

$$Q_n = u_0h_n + u_1h_{n-1} + \dots + u_Nh_{n-N}. \quad (2.53)$$

In the step from 2.52 to 2.53, the flame is assumed linear. Two further, physically motivated, assumptions about the flame are made:

- It is causal (i.e. there is no response before the impulse): $h_n = 0$ for $n < m$.
- Its response has finite duration: $h_n = 0$ for $n > m + M$.

These assumptions are illustrated in figure 2.2, which shows the excitation by a unit impulse at $t_n = t_m$ of the left, and the corresponding response (nonzero only in the interval between t_m and t_{m+M}) on the right.

Equation 2.53 can then be reduced to a shorter sum,

$$Q_n = \sum_{m=0}^M u_m h_{n-m} = \sum_{m=0}^M u_{n-m} h_m, \quad n = M, \dots, N. \quad (2.54)$$

Step 3: System identification to determine the UIR coefficients

The coefficients h_m could in principle be determined by deconvolution, i.e. by solving the linear Eq. 2.54; however, if the results for Q_n and u_n are corrupted (e.g. due to numerical noise), the results for h_m will inevitably be corrupted as well. This effect can be minimised by using an *averaged* form of Eq. 2.54. To this end, the cross-correlation of u and Q is introduced

$$c_n = \sum_{k=M}^N Q_k u_{k-n}, \quad n = 0, 1, \dots, M \quad (2.55)$$

and the auto-correlation of u

$$\Gamma_{mn} = \sum_{k=M}^N u_{k-m} u_{k-n}, \quad m, n = 0, 1, \dots, M, \quad (2.56)$$

where c_n is a vector with $M + 1$ components, and Γ_{mn} is an $(M + 1) \times (M + 1)$ matrix. Now Eq. 2.54 is multiplied by u_{k-n} and take the sum (average) from $k = M$ to N :

$$\sum_{k=M}^N Q_k u_{k-n} = \sum_{k=M}^N \sum_{m=0}^M u_{k-m} u_{k-n} h_m = \sum_{m=0}^M \left[\sum_{k=M}^N u_{k-m} u_{k-n} \right] h_m. \quad (2.57)$$

The sum on the left is the cross-correlation c_n , and the sum in square brackets is the auto-correlation Γ_{mn} , so Eq. 2.57 can be written as

$$c_n = \sum_{m=0}^M \Gamma_{mn} h_m. \quad (2.58)$$

This is the Wiener-Hopf equation. It is a linear equation for the coefficients h_m of the impulse response function.

Step 4: Transform into the frequency domain.

Once Eq. 2.58 is solved, h_n is transformed into the frequency domain via the z -transform, which can be applied to a time-series, e.g. to h_n , by

$$Z[h] = \sum_{n=0}^N h_n z^{-n}. \quad (2.59)$$

According to the convolution theorem for the z -transform [97], the time-domain Eq. 2.54 corresponds to the z -domain equation

$$Z[Q] = Z[u] Z[h]. \quad (2.60)$$

It can be, therefore, conclude that the z -transform of h is the FTF in the z -domain. It is possible to go from the z -domain into the *frequency*-domain if $z = e^{i\omega\Delta t}$ is chosen [98]:

$$\hat{h}(\omega) = \left[\sum_{n=0}^M h_n z^{-n} \right]_{z=e^{i\omega\Delta t}} = \sum_{n=0}^M h_n e^{-i\omega n \Delta t}, \quad (2.61)$$

where $\hat{h}(\omega)$ denotes the discrete-time Fourier transform of the series h_n . The normalised form of the FTF then follows from

$$FTF(\omega) = \frac{\hat{Q}(\omega)/\bar{Q}}{\hat{u}(\omega)/\bar{u}} = \hat{h}(\omega) \quad (2.62)$$

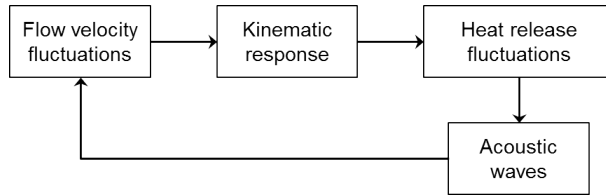


Figure 2.3: Scheme of a perfectly premixed thermoacoustic system.

Unfortunately, advanced methods, such as WHI can be used only in linear cases, i.e. the response of the flame to small amplitude velocity perturbations. Thus, in order to compute the FDF only one frequency excitation with one amplitude per simulation have to be applied.

2.2 Analytical models for FTF

It is possible to describe a transfer function of a linear system with a rational expression with a time lag of the form [99]:

$$TF(\omega) = \frac{\sum_{n=0}^N a_n (i\omega)^n}{\sum_{m=0}^M b_m (i\omega)^m} e^{-i\omega\tau}, \quad (2.63)$$

where τ is the time delay, M is the order of the transfer function; the order of the polynomial M in the denominator is larger than the order of the polynomial N in the numerator.

Increasing the values of M and N it is possible to achieve a very good fit to the computed Transfer Function. This makes the transfer function model in Eq. 2.63 suitable for linear calculations of thermoacoustic stability. It is possible to calculate the optimum values of parameters a_n and b_m for each amplitude of excitation characterised by its own transfer function. However, parameters a_n and b_m , in general, do not have a physical meaning. This makes the task of finding the dependence of a_n and b_m on the amplitude of the excitation not always possible, especially for high values of M and N . There is a need in a simple Flame Transfer Function model with relatively small amount of parameters that have physical meaning to make nonlinear simulations.

2.2.1 Time-lag distributed FTF model for perfectly premixed, swirl-stabilised, flames

Fluctuations of equivalence ratio are absent in perfectly premixed combustors. Moreover, as evidenced by Strobio Chen et al. [100] entropy fluctuations generated by perfectly premixed flames are negligible. Thus, the scheme of the perfectly premixed thermoacoustic system shown in Fig. 1.17 could be simplified to the scheme shown in Fig. 2.3. Heat release fluctuations, in this case, become dependent only on the upstream velocity perturbations.

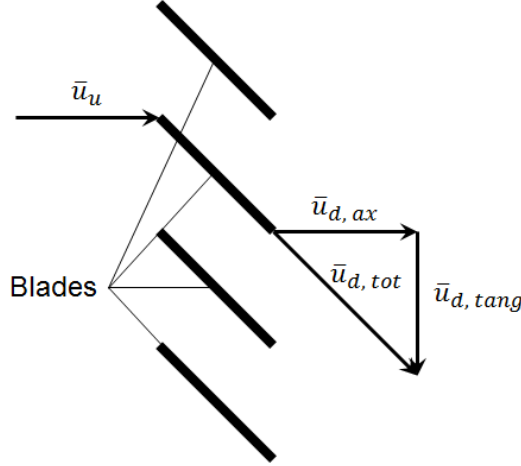


Figure 2.4: Unperturbed components of the velocity before and after the swirler.

$$\frac{\hat{Q}_{perf\ prem}(\omega)}{\bar{Q}} = \frac{\hat{Q}_u(\omega)}{\bar{Q}} = FTF_u(\omega) \frac{\hat{u}(\omega)}{\bar{u}}, \quad (2.64)$$

It is a common practice of gas turbines manufacturers to stabilise flames in gas turbines' combustors using swirled burners. Let us consider an axial swirler in a constant cross-section burner duct. First, consider unperturbed flow passing through the swirler. When the unperturbed flow goes through the blades of a swirled burner, it changes its direction (see Fig. 2.4). The velocity vector before the swirler consists only of the axial component $\bar{u}_{u, tot} = \bar{u}_{u, ax} = \bar{u}_u$, while the velocity vector after the swirler $\bar{u}_{d, tot}$ consists of axial, $\bar{u}_{d, ax}$, and tangential, $\bar{u}_{d, tang}$, components. The swirler causes a pressure drop for the flow passing through it, that is compensated by an increase in the velocity vector magnitude. Taking into account that density before and after the swirler is almost the same, from the conservation of mass one can recover that the axial component of the velocity vector after the swirler remains almost the same as before the swirler.

Now, let us consider the flow excited by an upstream perturbation u'_u (see Fig. 2.5). When such perturbation goes through the swirler, its axial component $u'_{d, ax}$ remains almost as before the swirler u'_u . Similarly to the mean velocity, a perturbation of the tangential component of velocity $u'_{d, tang}$ is produced.

Komarek and Polifke [36] have shown that the response of perfectly premixed swirl-stabilised flame to velocity fluctuations depends on oscillations of two components of velocity – axial and tangential – and have proposed to write the time-lag-distributed model of the flame response to upstream velocity fluctuations as:

$$FTF_u^{mod}(\omega) = e^{-i\omega\tau_1 - 0.5(\omega\sigma_1)^2} + e^{-i\omega\tau_2 - 0.5(\omega\sigma_2)^2} - e^{-i\omega\tau_3 - 0.5(\omega\sigma_3)^2}, \quad (2.65)$$

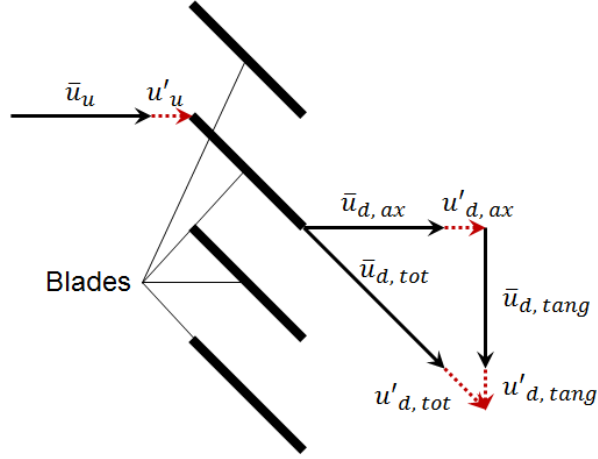


Figure 2.5: Mean and oscillating components of the velocity before and after the swirler.

where τ_i is the time delay and σ_i is its standard deviation. The response of the flame to the axial perturbations of the velocity is modelled with the parameters τ_1 and σ_1 . The parameters τ_2 , σ_2 , τ_3 and σ_3 model the response of the heat release to the tangential perturbations of the velocity produced by a swirler.

The physical meaning of parameters τ_i and σ_i is better understood if the frequency domain representation of the FTF is switched to its time domain representation, i.e. to the Unit Impulse Response (UIR). The analytical form of the UIR corresponding to the FTF of Eq. 2.65 is

$$UIR_u^{mod}(t) = \frac{1}{\sigma_1\sqrt{2\pi}}e^{-\frac{1}{2}\left(\frac{t-\tau_1}{\sigma_1}\right)^2} + \frac{1}{\sigma_2\sqrt{2\pi}}e^{-\frac{1}{2}\left(\frac{t-\tau_2}{\sigma_2}\right)^2} - \frac{1}{\sigma_3\sqrt{2\pi}}e^{-\frac{1}{2}\left(\frac{t-\tau_3}{\sigma_3}\right)^2}, \quad (2.66)$$

and the instantaneous heat release is computed as the convolution of the history of velocity perturbations and the Unit Impulse Response

$$Q'(t) = \frac{\bar{Q}}{\bar{u}} \int_0^\infty UIR_u^{mod}(t' - t)u'(t)dt'. \quad (2.67)$$

where t' is the integration variable.

Thus, Eq. 2.66 models the response of the heat release to upstream velocity oscillations with the help of three Gaussian functions with peaks at τ_i and standard deviations σ_i . In particular, the first terms on the RHS of Eqs. 2.65-2.66

$$UIR_{u,ax}^{mod}(t) = \frac{1}{\sigma_1\sqrt{2\pi}}e^{-\frac{1}{2}\left(\frac{t-\tau_1}{\sigma_1}\right)^2}, \quad (2.68)$$

$$FTF_{u,ax}^{mod}(\omega) = e^{-i\omega\tau_1 - 0.5(\omega\sigma_1)^2} \quad (2.69)$$

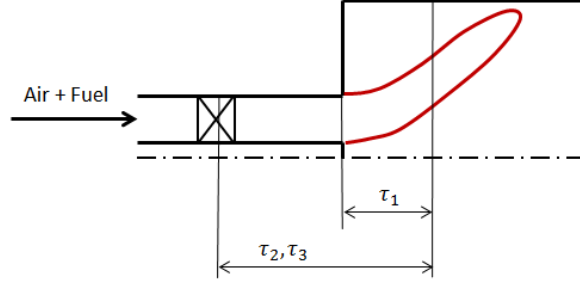


Figure 2.6: Characteristic convective time lags in perfectly premixed swirl-stabilised burners modelled with Eqs. 2.65-2.66.

model the response of the heat release to axial perturbations of velocity. The pair of parameters τ_1, σ_1 models the time that fluid particles spend while traveling from the zones where the flame is anchored to different points at the flame (see Fig. 2.6).

The integral of the heat release response to the unit impulse of the axial velocity perturbation modelled with Eq. 2.68, $\int_0^\infty UIR_{u, ax}^{mod}(t)dt$, is equal to 1. This means that the increase of the axial component of velocity will increase the heat release by the same normalised quantity $\delta u_{ax}/\bar{u}_{ax} = \delta Q/\bar{Q}$. The mixture mass flow rate is enhanced when the axial component of velocity increases; the increase in heat release will not influence the temperature of the burnt gases. In other words, perturbations of velocity in perfectly premixed flames do not create perturbations of entropy downstream of the flame.

The response of the heat release to the impulse of the tangential velocity and the respective FTF are modelled by the second and the third terms on the RHS of Eqs. 2.65-2.66

$$UIR_{u, tang}^{mod}(t) = \frac{1}{\sigma_2\sqrt{2\pi}}e^{-\frac{1}{2}\left(\frac{t-\tau_2}{\sigma_2}\right)^2} - \frac{1}{\sigma_3\sqrt{2\pi}}e^{-\frac{1}{2}\left(\frac{t-\tau_3}{\sigma_3}\right)^2}, \quad (2.70)$$

$$FTF_{u, tang}^{mod}(\omega) = e^{-i\omega\tau_2-0.5(\omega\sigma_2)^2} - e^{-i\omega\tau_3-0.5(\omega\sigma_3)^2}. \quad (2.71)$$

The parameters $\tau_2, \sigma_2, \tau_3,$ and σ_3 model the time that fluid particles spend to travel from the swirler to the flame (see Fig. 2.6). The integral of the heat release response to the unit impulse of the tangential velocity perturbation modelled with Eq. 2.70, $\int_0^\infty UIR_{u, tang}^{mod}(t)dt$, is equal to 0. This means that the increase of the tangential component of velocity will not modify the heat release in the quasi-steady perspective with respect to its unperturbed value.

As an example, let us consider the response of heat release to the impulse of velocity excitation [10]. Looking at the UIR in Fig. 2.7 it can be seen that this UIR could be modelled with Eq. 2.66. Taking into account the time step $\Delta t = 2.5 \times 10^{-5}$ s, it is possible to recover the values of parameters in the model: $\tau_1 = 1.65$ ms, $\sigma_1 = 0.55$ ms, $\tau_2 = 2.7$ ms, $\sigma_2 = 0.4$ ms, $\tau_3 = 3.7$ ms, and $\sigma_3 = 0.5$ ms. These values are estimated in order to reproduce qualitatively the UIR presented in Fig. 2.7 and to estimate the order of each value in the

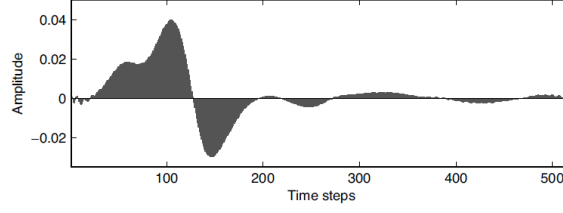


Figure 2.7: UIR of the heat release to the velocity excitation [10].

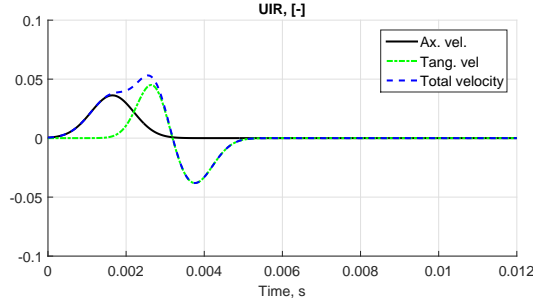


Figure 2.8: Response of the heat release to unit impulses of different components of the velocity modelled with Eqs. 2.66, 2.68, 2.70.

model 2.66. The response of the heat release to the axial impulse of velocity, to the tangential impulse of velocity and to the total perturbations of velocity modelled with Eqs. 2.68, 2.70, 2.66 are shown in Fig. 2.8. The respective FTFs are shown in Fig. 2.9.

Models 2.65-2.66 could be extended to the nonlinear regime of excitation, assuming dependence of parameters τ_i and σ_i on the amplitude of excitation A . A FDF model for perfectly premixed swirl-stabilised flame is presented in Section 3.3.3.

2.2.2 Time-lag distributed FTF model for technically premixed, swirl-stabilised, flames

Lieuwen et al. [101] have shown that in lean technically-premixed combustors the unsteady heat release could depend not only on flow fluctuations but also on equivalence ratio fluctuations [102]:

$$\frac{\hat{Q}_{part\ prem}(\omega)}{\bar{Q}} = FTF_u(\omega) \frac{\hat{u}(\omega)}{\bar{u}} + FTF_\phi(\omega) \frac{\hat{\phi}(\omega)}{\bar{\phi}}. \quad (2.72)$$

Similarly to Eq. 2.64, the dependence of the heat release oscillations on upstream equivalence ratio perturbations can be written as

$$\frac{\hat{Q}_\phi(\omega)}{\bar{Q}} = FTF_\phi(\omega) \frac{\hat{\phi}(\omega)}{\bar{\phi}}. \quad (2.73)$$

2. Description of the three-step approach for prediction of combustion instabilities in gas turbines

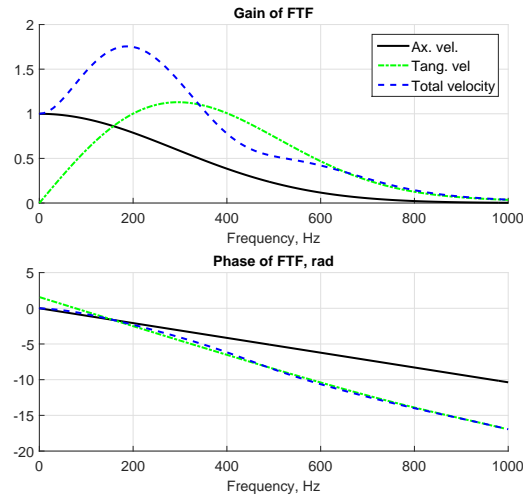


Figure 2.9: FTF of the perfectly premixed flame modelled with Eqs. 2.65, 2.69, 2.71.

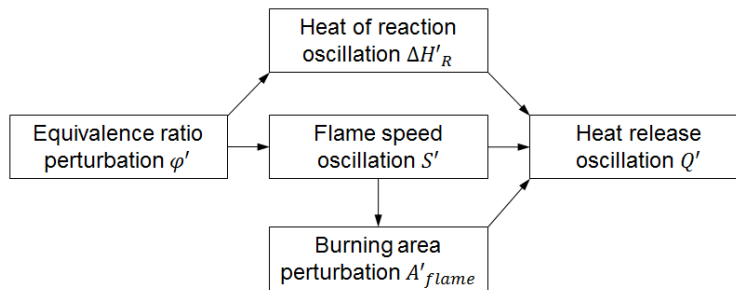


Figure 2.10: Physical mechanisms through which equivalence ratio fluctuations influence heat release fluctuations.

Cho and Lieuwen [103] have shown that the equivalence ratio fluctuations influence the heat release through three mechanisms: heat of reaction oscillations, flame speed oscillations and flame surface area oscillations that, in turn, are provoked by the flame speed oscillations (see Fig. 2.10).

Albayrak et al. [104] have shown analytically that the responses of the heat release to the heat of reaction perturbation and the flame speed perturbation provoked by the positive impulse of equivalence ratio are positive. Meanwhile, the heat release response to the positive impulse of equivalence ratio through the flame surface area perturbation is negative.

Let us consider the heat release response to the impulse of equivalence ratio perturbation from the work by Huber and Polifke [10]. Observing the UIR in Fig. 2.11 it can be seen that this UIR can be modelled similarly to Eq. 2.66:

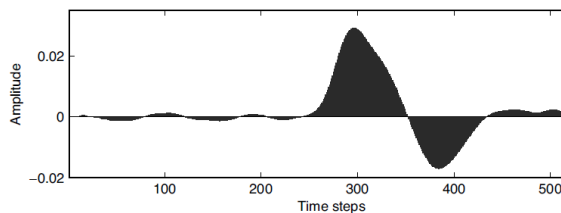


Figure 2.11: UIR of the heat release to the equivalence ratio perturbation [10].

$$UIR_{\phi}^{mod}(t) = \frac{1}{\sigma_4\sqrt{2\pi}}e^{-\frac{1}{2}\left(\frac{t-\tau_4}{\sigma_4}\right)^2} + \frac{1}{\sigma_5\sqrt{2\pi}}e^{-\frac{1}{2}\left(\frac{t-\tau_5}{\sigma_5}\right)^2} - \frac{1}{\sigma_6\sqrt{2\pi}}e^{-\frac{1}{2}\left(\frac{t-\tau_6}{\sigma_6}\right)^2}, \quad (2.74)$$

where parameters τ_4 , σ_4 , τ_5 , and σ_5 model the positive heat release response to the increase of the heat of reaction and to the increase of the flame speed due to the positive increment of the equivalence ratio, and parameters τ_6 and σ_6 model the negative heat release response to the positive increment of the equivalence ratio through the flame area change. All the parameters τ_4 , σ_4 , τ_5 , σ_5 , τ_6 , and σ_6 model the time that a fluid particle spends to travel from the point of the fuel injection to the different points at the flame (see Fig. 2.12). The FTF model that corresponds to Eq. 2.74 is

$$FTF_{\phi}^{mod}(\omega) = e^{-i\omega\tau_4-0.5(\omega\sigma_4)^2} + e^{-i\omega\tau_5-0.5(\omega\sigma_5)^2} - e^{-i\omega\tau_6-0.5(\omega\sigma_6)^2}. \quad (2.75)$$

The integral of the heat release response to the unit impulse of the equivalence ratio perturbation modelled with Eq. 2.74, $\int_0^{\infty} UIR_{\phi}^{mod}(t)dt$, is equal to 1. This means that the increase of the equivalence ratio will increase the heat release by the same normalised quantity $\delta\phi/\bar{\phi} = \delta Q/\bar{Q}$. Because the mixture mass flow rate remains the same when the equivalence ratio increases, the increase in the heat release will influence the temperature of the burnt gases. In other words, perturbations of equivalence ratio in technically premixed flames create perturbations of entropy downstream of the flame.

Taking into account the time step $\Delta t = 2.5 \times 10^{-5} s$, it is possible to recover the values of parameters in the model expressed by Eq. 2.74 for the UIR shown in Fig. 2.11: $\tau_4 = 7.5ms$, $\sigma_4 = 0.33ms$, $\tau_5 = 8.0ms$, $\sigma_5 = 0.45ms$, $\tau_6 = 9.5ms$, and $\sigma_6 = 0.5ms$. These values are estimated in order to reproduce qualitatively the UIR presented in Fig. 2.11 and to estimate the order of each value in the model 2.74. The response of the heat release to the impulse of equivalence ratio perturbation modelled with Eq. 2.74 is shown in Fig. 2.13. The corresponding FTF is shown in Fig. 2.14.

Many gas turbines burners are designed in such a way: the pressure drop of the gas passing through the burner is one order of magnitude higher than the pressure drop of the air. In a gas turbine combustion chamber equipped with such burners, the acoustic perturbations excite oscillations of the air mass flow through the burners, while, the gas flow remains almost unperturbed. This

2. Description of the three-step approach for prediction of combustion instabilities in gas turbines

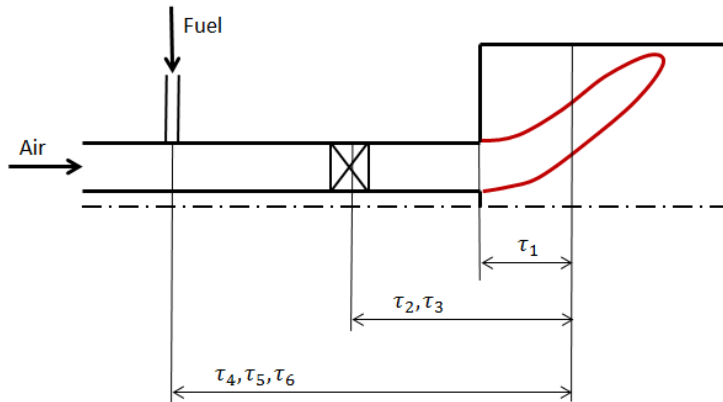


Figure 2.12: Characteristic convective time lags in technically premixed, swirl-stabilised, burners; general case.

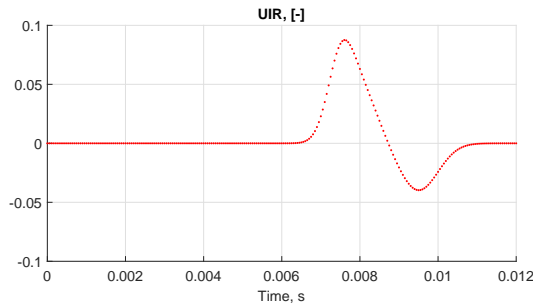


Figure 2.13: Response of the heat release to the unit impulse of equivalence ratio, modelled with Eq. 2.74.

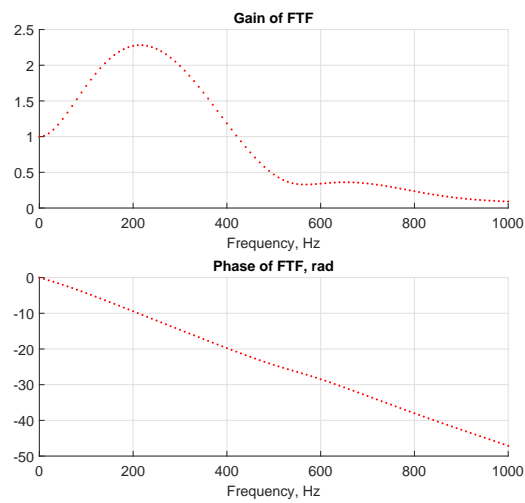


Figure 2.14: FTF of the heat release perturbations due to the equivalence ratio perturbations modelled with Eq. 2.75.

allows to make the assumption that the normalised perturbations of equivalence ratio ϕ are equal to the normalised fluctuations of flow velocity u in the burner and these perturbations are in antiphase to each other [105]:

$$\frac{\phi'}{\bar{\phi}} = -\frac{u'}{\bar{u}}. \quad (2.76)$$

Note that Eq. 2.76 does not hold under two conditions:

- at part loads far from the base load since the fuel pressure drop is reduced;
- not acoustically compact fuel mixing section.

For such burners, it is possible to write a model for the total FTF and the total UIR:

$$FTF_{tot}^{mod}(\omega) = FTF_u^{mod}(\omega) - FTF_\phi^{mod}(\omega), \quad (2.77)$$

$$UIR_{tot}^{mod}(\omega) = UIR_u^{mod}(\omega) - UIR_\phi^{mod}(\omega), \quad (2.78)$$

where FTF_u^{mod} , FTF_ϕ^{mod} , UIR_u^{mod} , and UIR_ϕ^{mod} are modelled with Eqs. 2.65, 2.75, 2.66, and 2.74, respectively. The fluctuations of the flame heat release Q' for such burners depend only on the velocity fluctuations, u'_r , at a reference position r upstream of the flame

$$\frac{\hat{Q}(\omega)}{\bar{Q}} = FTF_{tot}^{mod}(\omega) \frac{\hat{u}_r(\omega)}{\bar{u}_r}, \quad (2.79)$$

$$Q'(t) = \frac{\bar{Q}}{\bar{u}_r} \int_0^\infty UIR_{tot}^{mod}(t' - t) u'_r(t) dt'. \quad (2.80)$$

The total UIR and the total FTF are shown in Figs. 2.15 and 2.16, respectively. The negative sign before the second term in model 2.78 implies that the positive increment of velocity upstream the flame will produce the decay of equivalence ratio as exemplified by assumption 2.76. This is why the UIR of the heat release to the equivalence ratio perturbation modelled with Eq. 2.74 is shown in Fig. 2.15 with the opposite sign with respect to Fig. 2.13. For the same reason, the phase of the FTF of the heat release perturbations due to the equivalence ratio perturbations shown in Fig. 2.16 has the value π for zero frequency and the whole phase of the FTF is shifted up on the value π with respect to the FTF in Fig. 2.14.

At this point, the model for the FTF consists of 12 parameters and it could be cumbersome to determine all of them. For burners that have the fuel injection at the swirler blades (see Fig. 2.17), values of the characteristic time delays τ_4 and τ_6 are close to the values of τ_2 and τ_3 respectively, because of their physical meaning, and they cancel the resulting effect of each other (see Figs. 2.17, 2.18). Thus, models 2.77, 2.78 can be further simplified to include only 4 parameters [105, 38]

$$FTF_{tot}^{mod, simpl}(\omega) = e^{-i\omega\tau_1 - 0.5(\omega\sigma_1)^2} - e^{-i\omega\tau_2 - 0.5(\omega\sigma_2)^2}, \quad (2.81)$$

2. Description of the three-step approach for prediction of combustion instabilities in gas turbines

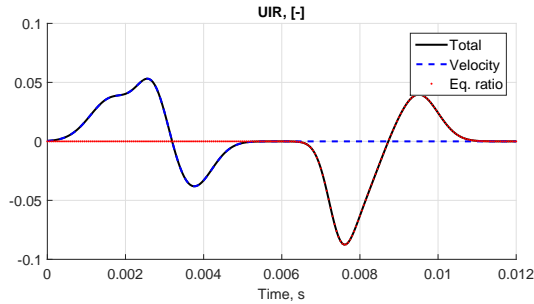


Figure 2.15: Response of the heat release to the unit impulse of velocity modelled with Eq. 2.66, to the unit impulse of equivalence ratio modelled with Eq. 2.74, and the total UIR modelled with the general Eq. 2.78.

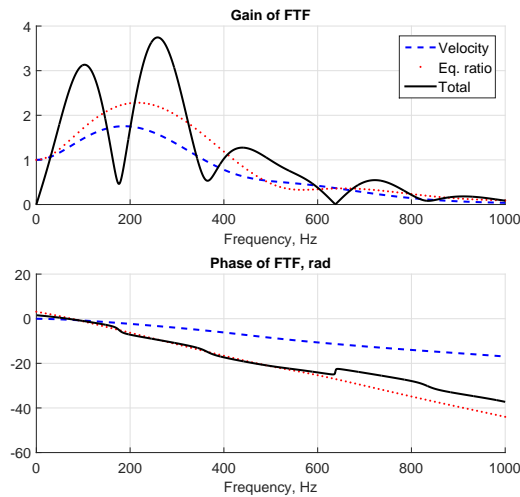


Figure 2.16: FTF of the heat release perturbations due to the velocity perturbations modelled with Eq. 2.65, due to the equivalence ratio perturbations modelled with Eq. 2.75, and the total FTF modelled with the general Eq. 2.77.

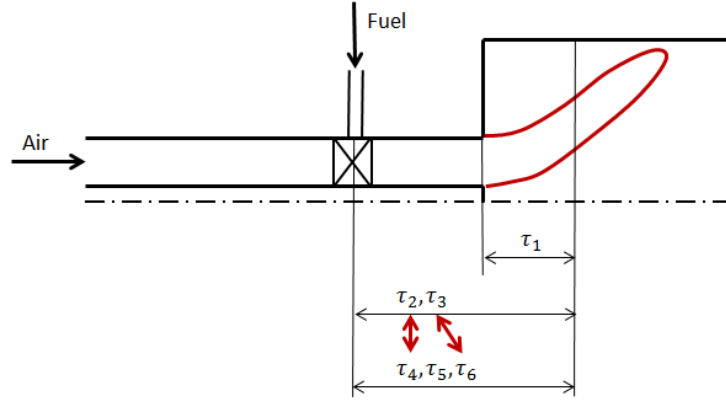


Figure 2.17: Characteristic convective time lags in technically premixed swirl-stabilised burners with fuel injection on the blades.

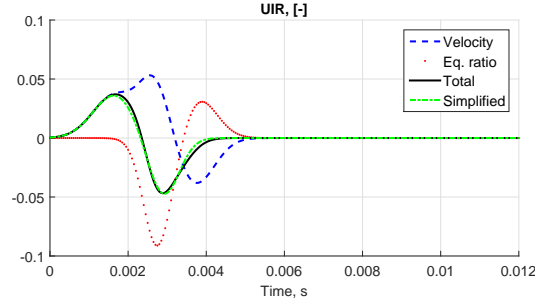


Figure 2.18: Response of the heat release to the unit impulse of velocity modelled with Eq. 2.66, to the unit impulse of equivalence ratio modelled with Eq. 2.74, the total UIR modelled with the general Eq. 2.78, and the total UIR modelled with the simplified Eq. 2.82.

$$UIR_{tot}^{mod, simpl}(t) = \frac{1}{\sigma_1 \sqrt{2\pi}} e^{-\frac{1}{2} \left(\frac{t-\tau_1}{\sigma_1} \right)^2} - \frac{1}{\sigma_2 \sqrt{2\pi}} e^{-\frac{1}{2} \left(\frac{t-\tau_2}{\sigma_2} \right)^2}. \quad (2.82)$$

The total FTF and the total UIR of the technically-premixed swirl-stabilised burners with the fuel injection at the swirler blades modelled with Eqs. 2.81 and 2.82 are shown in Figs. 2.18 and 2.19, respectively.

The integral of the heat release response to the unit impulse of the velocity perturbation modelled with Eq. 2.82, $\int_0^\infty UIR_{tot}^{mod, simpl}(t) dt$, is equal to 0. This means that the step increase of the velocity will decrease the equivalence ratio by the same normalised quantity and these two changes together, in a long-term perspective, will not change the heat release (see Fig. 2.19).

Let us explore the FTF modelled by Eq. 2.81 in the vicinity of $\omega = 0$. The value of the function in Eq. 2.81 at $\omega = 0$ is 0. The first derivative of the function is calculated as

2. Description of the three-step approach for prediction of combustion instabilities in gas turbines

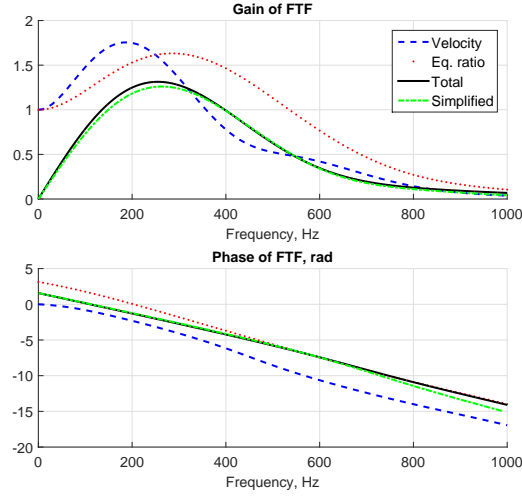


Figure 2.19: FTF of the heat release perturbations due to the velocity perturbations modelled with Eq. 2.65, due to the equivalence ratio perturbations modelled with Eq. 2.75, the total FTF modelled with the general Eq. 2.77, and the total FTF modelled with the simplified Eq. 2.81.

$$\left(FTF_{tot}^{mod, simpl} \right)'(\omega) = -i\tau_1 - 0.5\omega\sigma_1^2 e^{-i\omega\tau_1 - 0.5(\omega\sigma_1)^2} + i\tau_2 - 0.5\omega\sigma_2^2 e^{-i\omega\tau_2 - 0.5(\omega\sigma_2)^2}. \quad (2.83)$$

Next, the value of the function in Eq. 2.83 at $\omega = 0$ is

$$\left(FTF_{tot}^{mod, simpl} \right)'(0) = (\tau_2 - \tau_1)i. \quad (2.84)$$

Last, consider the first two terms of the MacLaurin series of the function in Eq. 2.81:

$$FTF_{tot}^{mod, simpl}(\omega) \approx FTF_{tot}^{mod, simpl}(0) + \omega \left(FTF_{tot}^{mod, simpl} \right)'(0) = \omega(\tau_2 - \tau_1)i. \quad (2.85)$$

The FTF modelled by Eq. 2.81 in the vicinity of $\omega = 0$ is defined as $\omega(\tau_2 - \tau_1)i$. Taking into account that $\tau_2 > \tau_1$ because fuel injection is positioned upstream of the flame holder, in the vicinity of $\omega = 0$ the phase of the FTF modelled by Eq. 2.81 is equal to $\pi/2$. The graphical interpretation of the FTF model (Eq. 2.81) in the complex plane is shown in Fig. 2.20 for frequencies in the range 0–200 Hz.

Models 2.81–2.82 could be extended to the nonlinear regime of excitation assuming dependence of parameters τ_i and σ_i on the amplitude of excitation A . Several FDF models for technically premixed swirl-stabilised flame are presented in Section 4.4.

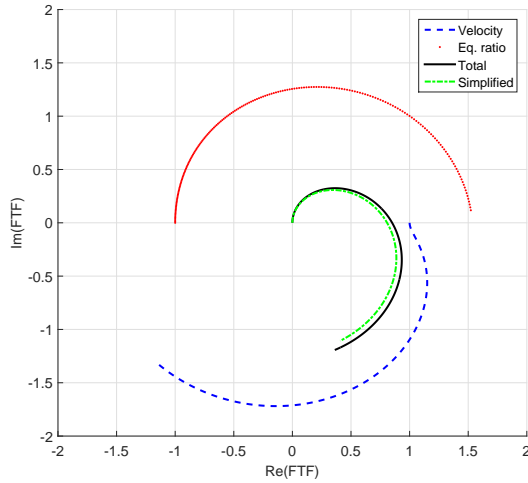


Figure 2.20: FTFs in the complex plane in the range of frequencies 0–200 Hz. FTF of the heat release perturbations due to the velocity perturbations modelled with Eq. 2.65, due to the velocity perturbations through equivalence ratio perturbations modelled with Eq. 2.75, the total FTF modelled with the general Eq. 2.77, and the total FTF modelled with the simplified Eq. 2.81.

2.3 Description of the network model approach

When the length of the setup under consideration is much larger than its dimensions in the other directions, acoustic modes with variations across the cross-sectional can be neglected. This leads to plane waves in a cylindrical combustor. The frequencies of interest for combustion instabilities in gas turbines are sufficiently low that this is often a good approximation. Then, it is possible to perform a one-dimensional low-order acoustic analysis with a network model [42, 43, 44, 45].

2.3.1 Waves propagation in sections

The setup under investigation is divided into a set of sections with constant cross-sectional area. Pressure, velocity, temperature and density are decomposed into the sum of their mean component (denoted by $\bar{}$) and their fluctuating component (denoted by \prime). Mean values of pressure, velocity, temperature, density and thermophysical properties are assumed to be constant along each section and change only from section to section.

Perturbations of pressure, velocity and density can be represented in terms of downstream and upstream propagating acoustic waves (characteristics):

$$p'(x, t) = f(x, t) + g(x, t), \quad (2.86)$$

$$u'(x, t) = \frac{1}{\bar{\rho}c_s} [f(x, t) - g(x, t)], \quad (2.87)$$

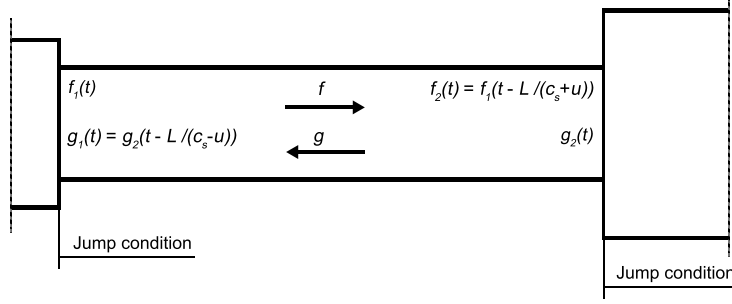


Figure 2.21: Scheme of waves propagating in a section for a low-order model.

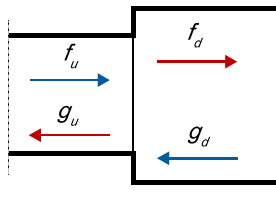


Figure 2.22: Scheme of waves propagation between adjacent sections in a low-order model.

$$\rho'(x, t) = \frac{1}{\bar{c}_s^2} [f(x, t) + g(x, t)], \quad (2.88)$$

where p is the pressure, f and g are downstream and upstream travelling components (Riemann invariants) of acoustic waves, respectively, \bar{c}_s is the mean speed of sound, u is the velocity, ρ is the density. The downstream propagating Riemann invariant f at the end of a section f_{end} at each instant of time is equal to its value at the beginning of the section f_{beg} with the time delay $\frac{L_{section}}{\bar{c}_s + \bar{u}}$ (see Fig. 2.21):

$$f_{end}(t) = f_{beg} \left(t - \frac{L_{section}}{\bar{c}_s + \bar{u}} \right), \quad (2.89)$$

where $L_{section}$ is the length of the section. Similarly, the upstream propagating Riemann invariant g at the beginning of the section g_{beg} at each instant of time is equal to its value at the end of the section g_{end} with the time delay $\frac{L_{section}}{\bar{c}_s - \bar{u}}$

$$g_{beg}(t) = g_{end} \left(t - \frac{L_{section}}{\bar{c}_s - \bar{u}} \right). \quad (2.90)$$

2.3.2 Area changes

In order to connect oscillating variables in different sections (see Fig. 2.22), jump conditions are to be imposed. To compute the jump conditions between sections separated by a compact acoustic element, such as a sharp cross-section

2.3. DESCRIPTION OF THE NETWORK MODEL APPROACH

area change or a compact swirler, the system of linearised equations describing conservation of mass and energy has to be written [30]. Momentum is not conserved along area change, thus the equation of momentum conservation is not considered. For the case of area decrease these equations are

$$S_u \rho_u u_u = S_d \rho_d u_d, \quad (2.91)$$

$$\left(\frac{\gamma}{\gamma-1} \frac{p}{\rho} + \frac{u^2}{2} \right)_u = \left(\frac{\gamma}{\gamma-1} \frac{p}{\rho} + \frac{u^2}{2} \right)_d + \zeta_{decr} \frac{u_d^2}{2}, \quad (2.92)$$

where S is the cross-sectional area of the section, γ is the heat capacity ratio, subscripts u and d denote upstream and downstream sections, respectively, ζ_{decr} is the coefficient of total pressure losses calculated with respect to the downstream velocity by the formula proposed by Idelchik [106]

$$\zeta_{decr} = \frac{1}{2} \left(1 - \frac{S_d}{S_u} \right)^{0.75}. \quad (2.93)$$

The linearised equation of mass is

$$S_u (\rho'_u \bar{u}_u + \bar{\rho}_u u'_u) = S_d (\rho'_d \bar{u}_d + \bar{\rho}_d u'_d). \quad (2.94)$$

The linearised Bernoulli equation can initially be written as

$$\left(\frac{\gamma}{\gamma-1} \frac{\bar{\rho} p' - \bar{p} \rho'}{\bar{\rho}^2} + \bar{u} u' \right)_u = \left(\frac{\gamma}{\gamma-1} \frac{\bar{\rho} p' - \bar{p} \rho'}{\bar{\rho}^2} + \bar{u} u' \right)_d + \zeta_{decr} \bar{u}_d u'_d. \quad (2.95)$$

It is possible to simplify Eq. 2.95. Taking into account the density fluctuations dependence on the pressure fluctuations neglecting entropy perturbations, $\rho' = \frac{1}{\bar{c}_s^2} p'$, the equation of state of an ideal gas written for mean quantities, $\bar{p} = R \bar{\rho} \bar{T}$, and the definition of the speed of sound for an ideal gas, $\bar{c}_s^2 = \gamma R \bar{T}$, the first terms on the LHS and RHS of Eq. 2.95 can be expressed as

$$\frac{\gamma}{\gamma-1} \frac{\bar{\rho} p' - \bar{p} \rho'}{\bar{\rho}^2} = \frac{1}{\bar{\rho}} p'. \quad (2.96)$$

The final form of the linearised Bernoulli equation in the case of area decrease expressed in terms of p' and u' reads:

$$\left(\frac{1}{\bar{\rho}} p' + \bar{u} u' \right)_u = \left(\frac{1}{\bar{\rho}} p' + \bar{u} u' \right)_d + \zeta_{decr} \bar{u}_d u'_d. \quad (2.97)$$

Substituting Eqs. 2.87 and 2.88 into Eq. 2.94 and defining the Mach number as $M = \frac{\bar{u}}{\bar{c}_s}$ we obtain

2. Description of the three-step approach for prediction of combustion instabilities in gas turbines

$$\begin{aligned} \frac{S_u}{\bar{c}_{s,u}}(M_u + 1)f_u + \frac{S_u}{\bar{c}_{s,u}}(M_u - 1)g_u &= \\ &= \frac{S_d}{\bar{c}_{s,d}}(M_d + 1)f_d + \frac{S_d}{\bar{c}_{s,d}}(M_d - 1)g_d \end{aligned} \quad (2.98)$$

Substituting Eqs. 2.86 and 2.87 into Eq. 2.97 we obtain

$$\frac{1}{\bar{\rho}_d}(1 + M_d(1 + \zeta_{decr}))f_d + \frac{1}{\bar{\rho}_d}(1 - M_d(1 + \zeta_{decr}))g_d = \frac{1}{\bar{\rho}_u}(1 + M_u)f_u + \frac{1}{\bar{\rho}_u}(1 - M_u)g_u \quad (2.99)$$

Reorganising the system of equations 2.98 and 2.99 and writing them in matrix form results into

$$\mathbf{F} \begin{bmatrix} f_d \\ g_u \end{bmatrix} = \mathbf{K} \begin{bmatrix} f_u \\ g_d \end{bmatrix}, \quad (2.100)$$

with the matrices \mathbf{F} and \mathbf{K} for the case of area decrease given by

$$\mathbf{F}_{decr} = \begin{bmatrix} \frac{S_d}{\bar{c}_{s,d}}(1 + M_d) & \frac{S_u}{\bar{c}_{s,u}}(1 - M_u) \\ \frac{1}{\bar{\rho}_d}(1 + M_d(1 + \zeta_{decr})) & -\frac{1}{\bar{\rho}_u}(1 - M_u) \end{bmatrix}, \quad (2.101)$$

$$\mathbf{K}_{decr} = \begin{bmatrix} \frac{S_u}{\bar{c}_{s,u}}(1 + M_u) & \frac{S_d}{\bar{c}_{s,d}}(1 - M_d) \\ \frac{1}{\bar{\rho}_u}(1 + M_u) & -\frac{1}{\bar{\rho}_d}(1 - M_d(1 + \zeta_{decr})) \end{bmatrix}. \quad (2.102)$$

For the case of area increase, Bernoulli equation is

$$\left(\frac{\gamma}{\gamma - 1} \frac{p}{\rho} + \frac{u^2}{2} \right)_u - \zeta_{incr} \frac{u_u^2}{2} = \left(\frac{\gamma}{\gamma - 1} \frac{p}{\rho} + \frac{u^2}{2} \right)_d, \quad (2.103)$$

where ζ_{incr} is the coefficient of total pressure losses calculated with respect to the upstream velocity by the formula proposed by Idelchik [106]

$$\zeta_{incr} = \left(1 - \frac{S_u}{S_d} \right)^2. \quad (2.104)$$

Following the same procedure as in the case of area decrease, one can obtain the system of equations 2.100, where the matrices \mathbf{F} and \mathbf{K} are now:

$$\mathbf{F}_{incr} = \begin{bmatrix} \frac{S_d}{\bar{c}_{s,d}}(1 + M_d) & \frac{S_u}{\bar{c}_{s,u}}(1 - M_u) \\ \frac{1}{\bar{\rho}_d}(1 + M_d) & -\frac{1}{\bar{\rho}_u}(1 - M_u(1 - \zeta_{incr})) \end{bmatrix}, \quad (2.105)$$

$$\mathbf{K}_{incr} = \begin{bmatrix} \frac{S_u}{\bar{c}_{s,u}}(1 + M_u) & \frac{S_d}{\bar{c}_{s,d}}(1 - M_d) \\ \frac{1}{\bar{\rho}_u}(1 + M_u(1 - \zeta_{incr})) & -\frac{1}{\bar{\rho}_d}(1 - M_d) \end{bmatrix}. \quad (2.106)$$

2.3.3 Unsteady heat release

The flame in the network model approach is assumed to be compact when its length is much shorter than the minimum length of the acoustic wave under consideration. The unsteady heat release is placed between sections with low and high temperatures. In this way, both mean and oscillating components of heat release are situated at the same point. To calculate jump conditions at the flame, the system of linearised equations of conservation of momentum and energy (product of mass conservation equation and Bernoulli equation) has to be solved. Assuming the same cross-sectional area in the upstream and the downstream sections, the equations of momentum and energy conservation are

$$p_u + \rho_u u_u^2 = p_d + \rho_d u_d^2 \quad (2.107)$$

$$\left(\frac{\gamma}{\gamma-1} p u + \rho \frac{u^3}{2} \right)_u + \frac{Q}{S} = \left(\frac{\gamma}{\gamma-1} p u + \rho \frac{u^3}{2} \right)_d. \quad (2.108)$$

The linearised equations of momentum and energy conservation are

$$p'_u + 2\bar{\rho}_u \bar{u}_u u'_u + \bar{u}_u^2 \rho'_u = p'_d + 2\bar{\rho}_d \bar{u}_d u'_d + \bar{u}_d^2 \rho'_d, \quad (2.109)$$

$$\begin{aligned} \left(\frac{\gamma}{\gamma-1} \bar{p} u' + \frac{\gamma}{\gamma-1} \bar{u} p' + \frac{3\bar{\rho} \bar{u}^2}{2} u' + \frac{\bar{u}^3}{2} \rho' \right)_u + \frac{Q'}{S} = \\ = \left(\frac{\gamma}{\gamma-1} \bar{p} u' + \frac{\gamma}{\gamma-1} \bar{u} p' + \frac{3\bar{\rho} \bar{u}^2}{2} u' + \frac{\bar{u}^3}{2} \rho' \right)_d. \end{aligned} \quad (2.110)$$

Substituting Eqs. 2.86, 2.87 and 2.88 into Eqs. 2.109 and 2.110 we obtain

$$\begin{aligned} (1 + 2M_u + M_u^2) f_u + (1 - 2M_u + M_u^2) g_u = \\ = (1 + 2M_d + M_d^2) f_d + (1 - 2M_d + M_d^2) g_d, \end{aligned} \quad (2.111)$$

$$\begin{aligned} \left[\frac{\bar{c}_s}{\gamma-1} + \frac{\gamma \bar{u}}{\gamma-1} + \frac{3\bar{u}^2}{2\bar{c}_s} + \frac{\bar{u}^3}{2\bar{c}_s^2} \right] f_u - \\ - \left[\frac{\bar{c}_s}{\gamma-1} - \frac{\gamma \bar{u}}{\gamma-1} + \frac{3\bar{u}^2}{2\bar{c}_s} - \frac{\bar{u}^3}{2\bar{c}_s^2} \right]_u g_u + \frac{Q'}{S} = \\ = \left[\frac{\bar{c}_s}{\gamma-1} + \frac{\gamma \bar{u}}{\gamma-1} + \frac{3\bar{u}^2}{2\bar{c}_s} + \frac{\bar{u}^3}{2\bar{c}_s^2} \right]_d f_d - \\ - \left[\frac{\bar{c}_s}{\gamma-1} - \frac{\gamma \bar{u}}{\gamma-1} + \frac{3\bar{u}^2}{2\bar{c}_s} - \frac{\bar{u}^3}{2\bar{c}_s^2} \right]_d g_d. \end{aligned} \quad (2.112)$$

Reorganising the system of equations 2.111 and 2.112 and writing them in matrix form results into

$$\mathbf{J} \begin{bmatrix} f_d \\ g_u \end{bmatrix} = \mathbf{H} \begin{bmatrix} f_u \\ g_d \\ Q' \end{bmatrix}, \quad (2.113)$$

where the coefficients of matrices \mathbf{J} and \mathbf{H} are

$$\mathbf{J} = \begin{bmatrix} (1 + 2M_d + M_d^2) & -(1 - 2M_u + M_u^2) \\ \left[\frac{\bar{c}_s + \gamma \bar{u}}{\gamma - 1} + \frac{3\bar{u}^2}{2\bar{c}_s} + \frac{\bar{u}^3}{2\bar{c}_s^2} \right]_d & \left[\frac{\bar{c}_s - \gamma \bar{u}}{\gamma - 1} + \frac{3\bar{u}^2}{2\bar{c}_s} - \frac{\bar{u}^3}{2\bar{c}_s^2} \right]_u \end{bmatrix}, \quad (2.114)$$

$$\mathbf{H} = \begin{bmatrix} (1 + 2M_u + M_u^2) & -(1 - 2M_d + M_d^2) & 0 \\ \left[\frac{\bar{c}_s + \gamma \bar{u}}{\gamma - 1} + \frac{3\bar{u}^2}{2\bar{c}_s} + \frac{\bar{u}^3}{2\bar{c}_s^2} \right]_u & \left[\frac{\bar{c}_s - \gamma \bar{u}}{\gamma - 1} + \frac{3\bar{u}^2}{2\bar{c}_s} - \frac{\bar{u}^3}{2\bar{c}_s^2} \right]_d & \frac{1}{S} \end{bmatrix}. \quad (2.115)$$

2.3.4 Boundary conditions

At the beginning of the first section, f and g waves are related by the reflection coefficient R_{in}

$$f_{1,beg} = R_{in}g_{1,beg}, \quad (2.116)$$

and at the end of the last N section g and f waves are related by the reflection coefficient R_{out}

$$g_{N,end} = R_{out}f_{N,end}. \quad (2.117)$$

In general, the reflection coefficients are complex values, i.e. can be represented in the way

$$R_i = |R_i|e^{i\phi_{refl}}, \quad (2.118)$$

where $|R_i|$ is the amplitude of the reflection coefficient and ϕ_{refl} is its phase. Phase of the reflection coefficient takes into account the end correction.

2.3.5 Elements interconnection

An example of elements interconnection in a low-order network model is shown in Fig. 2.23. Time histories of acoustic characteristics f and g are modelled in the network model. It consists of four ducts in which propagation of waves f and g are modelled according to Eqs. 2.89 and 2.90. The waves between *Plenum duct* and *Burner duct* are connected according to Eqs. 2.100-2.102. The waves between *Burner duct* and *Combustor duct 1* are connected according to Eqs. 2.100, 2.105 and 2.106. The waves between *Combustor duct 1* and *Combustor duct 2* are connected according to Eqs. 2.113-2.115. The velocity perturbations are computed at the end of *Burner duct* (the reference position) from the acoustic invariants at this position according to Eq. 2.87. The heat release perturbations are calculated from the velocity perturbations according to one of the FTF or FDF models described in section 2.2. The acoustic invariants are connected at the inlet according to Eq. 2.116 and at the outlet according to Eq. 2.117. The setup is perturbed at the inlet by an external broadband excitation for the first t_{exc} time of simulations. After the excitation

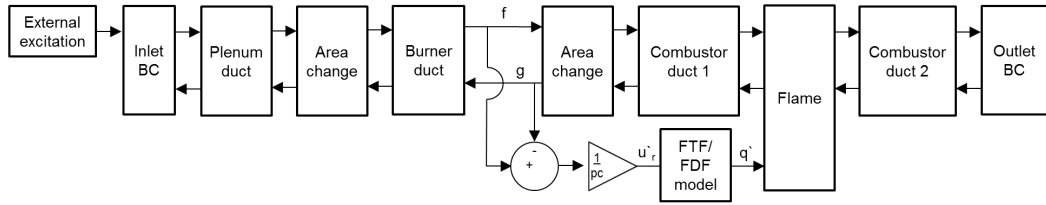


Figure 2.23: Elements interconnection in a low-order network model.

time t_{exc} , acoustic oscillations modelled by the network model either saturate to a limit cycle or decay. The dominant frequencies of oscillations (either growing, decaying or saturated) are computed by performing the Fast Fourier Transform of the simulated perturbations time history.

2.4 Discussion

In this chapter, the three-step approach for prediction of combustion instabilities in gas turbines is described. The first step of the approach is to calculate the Flame Describing Function (FDF) of a setup. Both Unsteady Reynolds-Averaged Navier-Stokes method and the Flame Speed Closure model used to compute the FDF numerically are presented. The Wiener-Hopf inversion method for rapid Flame Transfer Functions (FTF) calculations is presented. Time-lag distributed FTF model for the technically-premixed swirl-stabilised flames is presented in this chapter similarly to the FTF model for the perfectly premixed flames presented in the literature. Furthermore, it is shown that under certain conditions the FTF model for the technically-premixed flames can be significantly simplified. At the end of this chapter, the network model approach used further in this work is presented.

2. Description of the three-step approach for prediction of combustion instabilities in gas turbines

Chapter 3

Application of the three-step approach to a laboratory, perfectly premixed, setup

3.1 Description of the setup

The test rig under consideration is operated under atmospheric pressure and consist of three main parts: a plenum, a swirl stabilised burner with a central bluff body and a combustion chamber (see Fig. 3.1). A perfectly premixed mixture of methane and air with equivalence ratio equal to 0.77 enters the setup. The plenum is a cylinder with diameter of 200 mm and length of 170 mm. A rigid sinter plate is placed at the beginning of the plenum. The burner exit is represented by an annular section with an inner diameter of 16 mm and an outer diameter of 40 mm. The swirler consists of 8 blades with the length of 30 mm, positioned 30 mm upstream of the burner exit. The length of the burner duct is 180 mm. The combustion chamber has the quadratic cross section of $90 \times 90 \text{ mm}^2$. The walls of the chamber are made from glass to enable measurements of the flame dynamics. Combustion chamber walls are water-cooled. In the experiments, the position of the heat release distribution was determined by OH^* chemiluminescence measurements. The length of the combustion chamber is variable and during FTF measurements was kept equal to 300 mm. Experiments with a combustion chamber length of 700 mm have also been performed [9]. A perforated plate is placed at the end of the combustion chamber in order to ensure a low reflective acoustic boundary condition. Further details on the experimental set-up can be found in the work by Komarek and Polifke [36].

With the length of the combustion chamber of 300 mm the setup was thermoacoustically stable in the experiments; with the length of the combustion chamber of 700 mm pressure oscillations at a frequency of 101.3 Hz were measured.

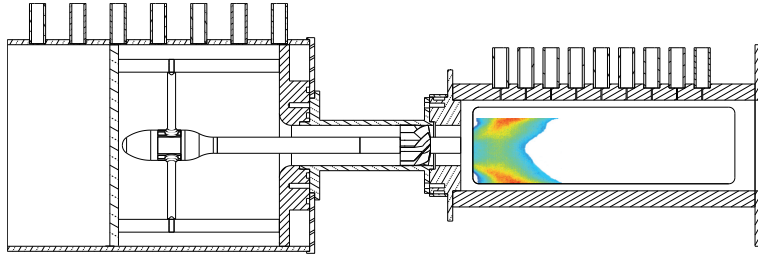


Figure 3.1: Scheme of the BRS test rig (image courtesy of Thomas Komarek).

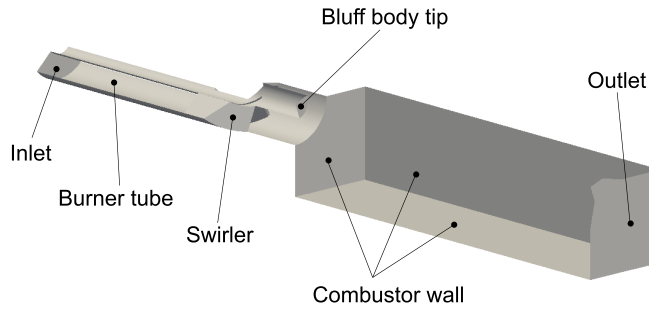


Figure 3.2: Sector scheme of the numerical set-up of the BRS test rig.

3.2 CFD simulations

3.2.1 Numerical setup

Since the main goal of the simulations is to calculate the flame dynamics, the effect of the plenum on the fluid dynamics in the chamber is assumed to be negligible and the plenum is not considered in the numerical setup. The length of the burner duct in the simulations is 160 mm. A combustor length of 200 mm is used for the sake of computational economy of the simulations. The heat release zone lies in the first 100 mm of the combustion chamber, as reported by Komarek and Polifke [36]. It will be shown in the next section that the recirculation zone lies within the computational domain. Thus, it is shown a posteriori that the considered combustor length is enough to simulate the behaviour of the flame. Since the structure of the set-up is periodical, just one-quarter of the test rig has been modelled in the simulations (see Fig. 3.2). A 3D structured mesh consisting of around 280000 cells is created using the commercial software ANSYS® ICEM CFD™. The time step of the simulations is 4×10^{-7} s to ensure an acoustic CFL number lower than 0.7.

In this investigation, the thermal power is equal to 30 kW. To avoid the development of resonance modes, non-reflective or partially reflective boundary conditions at the inlet and at the outlet have been employed. The *waveTransmissive* boundary condition implemented in OpenFOAM [84] is used in this work. It is based on the work by Poinso and Lele [107] and is expressed by

Table 3.1: Boundary Conditions for the BRS numerical model.

Face	Boundary condition	Details
Inlet	Velocity inlet	11.3 m/s
Outlet	Pressure outlet	101325 Pa
Burner tube, swirler	Adiabatic no-slip wall	–
Combustor walls	Isothermal no-slip wall	600 K
Bluff body tip	Isothermal no-slip wall	600 K

the following equation for the pressure at the boundaries:

$$\frac{\partial p}{\partial t} + u_{wave} \frac{\partial p}{\partial x} = \frac{u_{wave}}{l_{inf}} (p_{inf} - p), \quad (3.1)$$

where $u_{wave} = u + c_s$ at the outlet, $u_{wave} = u - c_s$ at the inlet, c_s is the speed of sound, l_{inf} is the distance from the boundary (outlet or inlet) at which the pressure field p becomes equal to p_{inf} . $l_{inf} = 1$ m is taken in this work because it results in low reflection coefficients for a wide range of frequencies. Boundary conditions for the unperturbed simulation are listed in Tab. 3.1.

Walls of the experimental setup under consideration are made of glass in order to be able to observe the flame and they are water-cooled. The temperature of the combustor walls is imposed to 600 K to take into account heat losses, as suggested by Tay-Wo-Chong and Polifke [65].

3.2.2 Results of unperturbed simulations

First, the value of the FSC model parameter u_{FSC} used in Eq. 2.33 is taken equal to the velocity at the inlet of the burner tube, $u_{FSC} = 11.3$ m/s. Due to the funnelling effect the velocity of the flow between the flame holder and the flame is larger than at the exit from the burner (see Fig. 3.3) and thus $u_{FSC} = 18$ m/s is taken in further simulations.

Fields of axial velocity, temperature and heat release in the longitudinal cross-section obtained from unperturbed simulations are shown in Figs. 3.3, 3.4, and 3.5 respectively. It is seen from Fig. 3.3 that the inner recirculation zone completely lies in the computational domain. It is seen from Fig. 3.4 that the temperature of the flow in the outer recirculation zone is lower than the adiabatic temperature of the flame.

It is illustrative to compare the distributions of heat release in experiments and simulations along the longitudinal axis. To obtain this distribution from our simulation we take several planes perpendicular to the longitudinal axis in the range $0 \div 0.1$ m from the beginning of the combustion chamber in the axial direction. Then, the heat release is integrated over these planes and the resulting values are plotted over the longitudinal axis (see Fig. 3.6).

The difference between experimental and numerical heat release distributions is explained by the presence of the flame both in the inner and outer shear layers in simulation (so-called M-flame) (see Fig. 3.5). However, in the

3. Application of the three-step approach to a laboratory, perfectly premixed, setup

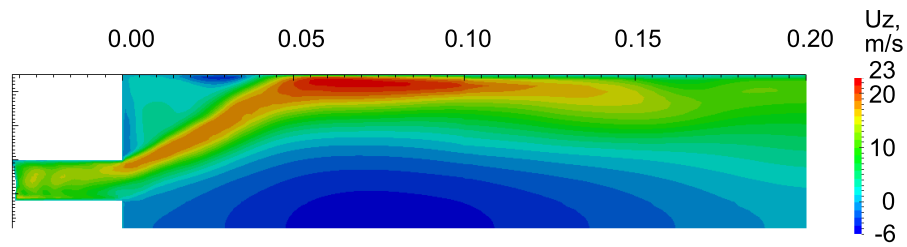


Figure 3.3: Axial velocity distribution from the unperturbed simulation.

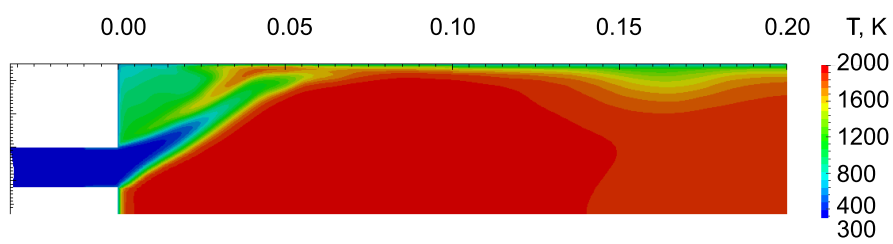


Figure 3.4: Temperature distribution from the unperturbed simulation.

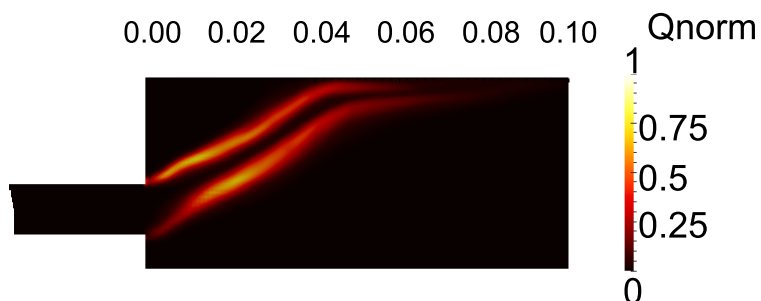


Figure 3.5: Normalised unperturbed heat release distribution from the simulation.

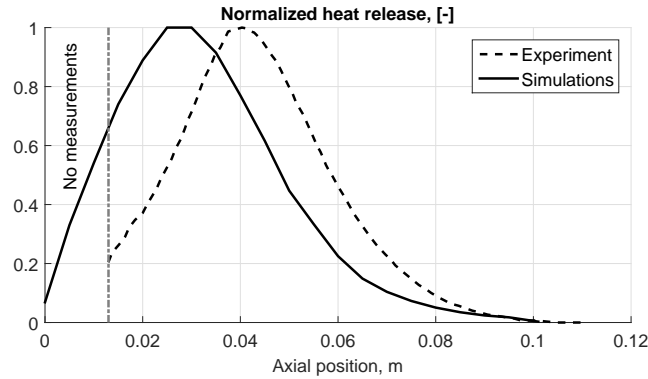


Figure 3.6: OH^* chemiluminescence distribution from experiment and heat release distribution from the simulation.

experiments the flame was observed mostly in the inner shear layer, that is called V-flame. This is explained by the fact that the FSC model is adiabatic and the quenching influence on heat losses [108] is not taken into account in the FSC model.

3.2.3 FDF computations

FTF computation

A transient numerical simulation of the system is performed exciting the axial component of velocity at the inlet of the computational domain. The signal of excitation is composed of a sum of sine waves with random frequency in the range 0–1 kHz and random phase. The excitation signal is normalised in a way that three standard deviations of the signal amplitude are equal to 10% of the mean velocity at the inlet of the computational domain (see Fig. 3.7). The signal of the velocity excitation applied at the inlet of the computational domain and its Fast Fourier Transform are shown in Fig. 3.7 and 3.8, respectively.

The time series u_r is during the simulations the axial component of the velocity averaged in the plane perpendicular to the z -axis situated 2 cm upstream of the burner exit (1 cm downstream of the swirler). The response of the flame Q is measured in the simulations as the volumetric integral of Eq. 2.44. After that, the mean values \bar{u}_r and \bar{Q} of the measured u_r and Q are computed and are subtracted from the time series of u_r and Q , respectively, in order to obtain the fluctuations of the axial velocity u_r' and the fluctuations of the heat release Q' .

The simulation is run for 129 ms in real time. Longer simulation times do not change the FTF. The duration of the Unit Impulse Response (UIR) is assumed to be equal to 10 ms. The first 15 ms are considered as a transition period and are neglected. Using the Wiener-Hopf inversion method described in section 2.1.3, the Flame Transfer Function of the BRS test rig is calculated and is shown in Fig. 3.9 together with the experimental FTF [9].

3. Application of the three-step approach to a laboratory, perfectly premixed, setup

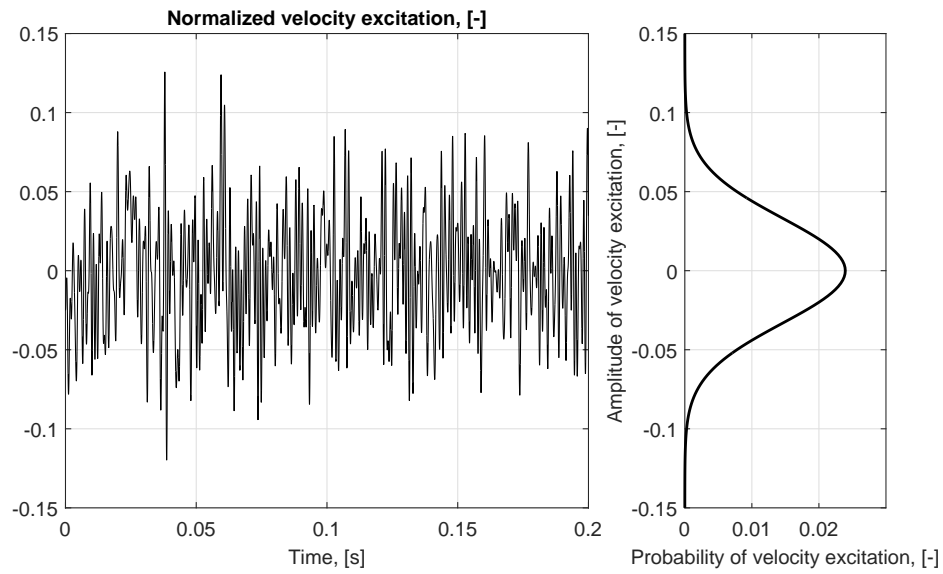


Figure 3.7: Signal of the velocity excitation.

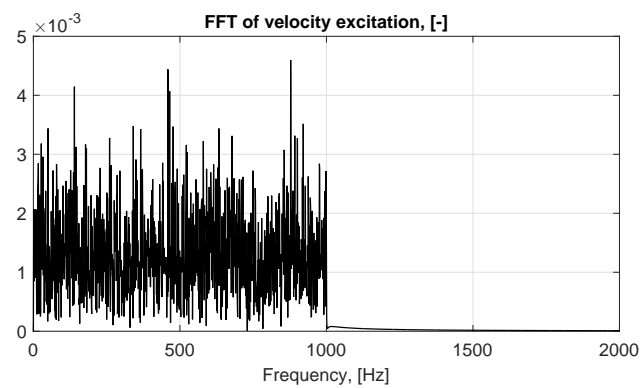


Figure 3.8: Fast Fourier Transform of the excitation signal shown in Fig. 3.7.

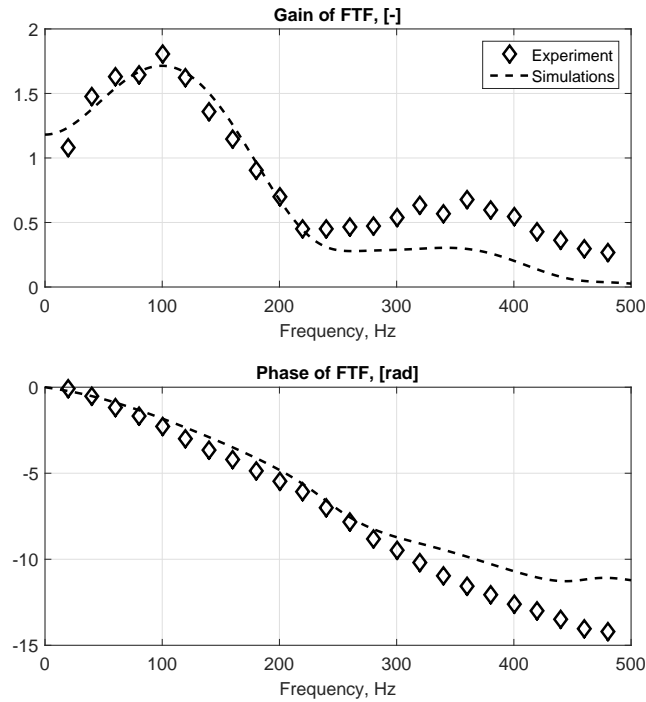


Figure 3.9: FTF obtained experimentally [9] and from simulations.

There is a good agreement between the experimentally obtained FTF and that obtained from the simulations in terms of gain of the FTF in the range of frequencies 0–220 Hz. The shift in the phase of the FTF is better understood if we switch to the time-domain representation of the FTF - the UIR. It is possible to calculate the coefficients h_k of the UIR knowing the FTF using the formula

$$h_k = \Re \left[\frac{\Delta t}{\pi} \sum_{\omega=0}^{\pi/\Delta t} FTF(\omega) e^{i\omega k \Delta t} \right], \quad k = 0, \dots, L, \quad (3.2)$$

where L is the length of the h_k vector.

UIRs corresponding to the FTF obtained experimentally and from simulations are shown in Fig. 3.10. The UIR calculated from CFD simulations follows the shape of the UIR computed from the experimental data but is shorter in time. In other words, in the CFD simulations the heat release responds earlier to the velocity excitations with respect to the experiments. This can be explained by the shifted distribution of the heat release obtained with CFD simulations with respect to the experimental one as shown in Fig. 3.6. One can note that the significant change in the heat release distribution shown in Fig. 3.6 results in the not so significant change of the FTF. This question is addressed in section 3.3.2.

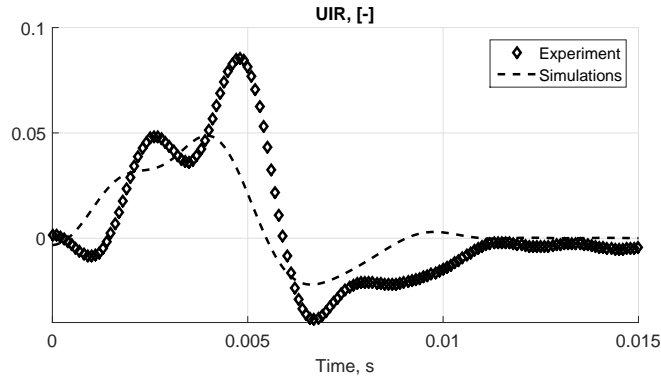


Figure 3.10: Coefficients h_k computed from FTFs obtained experimentally [9] and from simulations.

FDF computations

In order to construct the Flame Describing Function, excitation frequencies of 100 Hz, 160 Hz, 240 Hz and 320 Hz are chosen. 100 Hz, 240 Hz and 320 Hz are local extrema of the FTF gain shown in Fig. 3.9. To ensure that the difference of the FDF phase between 100 Hz and 240 Hz is smaller than π , the 160 Hz is also considered. Different excitation amplitudes of velocity perturbations are applied at the inlet of the numerical setup in order to obtain velocity perturbations after the swirler with the amplitude of 30%, 50% and 70% for each frequency.

The FDF obtained from the simulations is shown in Fig. 3.11. The most significant decay of the gain of the FDF with increasing amplitude of the velocity perturbations is observed at 100 Hz, while the most significant change in phase of the FDF is observed at 240 Hz.

The reason for the variation of the phase of the FDF for different amplitudes of excitation can be explained as follows.

In Fig. 3.12 the normalised velocity perturbations at the reference point u'_r/\bar{u}_r and the normalised heat release perturbations Q'/\bar{Q} during one period of oscillation at 240 Hz with the excitation amplitude $A = \max(u'_r)/\bar{u}_r = 70\%$ are shown. After a quarter of the oscillation period (90° phase) shown in Fig. 3.12 the heat release experiences its minimum value and after three-quarters of the oscillation period (270° phase), it experiences its maximum value. It is seen in Figs. 3.13 and 3.14 that at 180° and 270° phase the flame enters the burner's tube. At the same time at 180° phase the axial velocity passes through its minimum values (see Fig. 3.12). Because the high-amplitude velocity excitations are applied, around 180° phase the turbulent flame velocity locally is higher than the axial component of the flow velocity. This difference of velocities pushes the flame front behind the flame holder. Because of the heat release presence behind the flame holder when applying high-amplitude acoustic excitations (see Figs. 3.14 and 3.15), the flame responds earlier to acoustic excitations in comparison to small-amplitude excitations that results in the lower absolute value of the phase of the FDF.

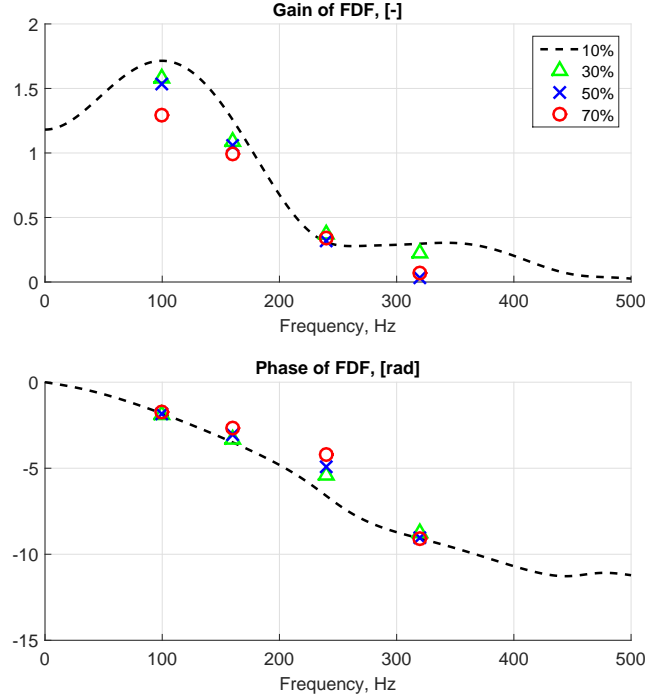


Figure 3.11: FTF (dashed line) and FDF (points) obtained from simulations.

Moreover, when high-amplitude velocity excitations are applied, the turbulence of the flow in the combustor is intensified. This results in higher turbulent flame velocity and, as a result, the shift of the heat release distribution towards the swirler (see Figs. 3.13, 3.15). Results of the simulations with high-amplitude excitation at 240 Hz are shown but similar behaviours are observed with excitations at other frequencies. Similar flame behaviour was also observed during LES of limit-cycle oscillations in a rocket engine [35]. Further insight on the change of the FTF phase is given in section 3.3.3.

3.3 Analytical models for the FDF

3.3.1 Rational time-lagged FTF model

The computed FTF can be approximated with a rational time-lagged (RTL) transfer function of the form 2.63. The FTF calculated in the previous section (see Fig. 3.11) can be approximated as sum of one second-order low pass filter and two band-pass filters multiplied by a time-lag:

$$FTF_{mod\ RTL}(\omega) = \left[\frac{n_{f,1}\omega_{0,1}^2}{-\omega^2 + 2i\xi_1\omega_{0,1}\omega + \omega_{0,1}^2} + \sum_{j=2}^3 \frac{2in_{f,j}\xi_j\omega_{0,j}\omega}{-\omega^2 + 2i\xi_j\omega_{0,j}\omega + \omega_{0,j}^2} \right] e^{-i\omega\tau_f}, \quad (3.3)$$

3. Application of the three-step approach to a laboratory, perfectly premixed, setup

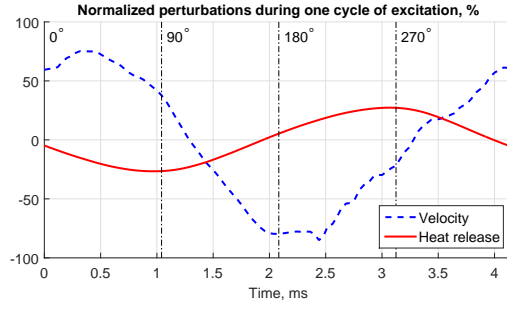


Figure 3.12: Normalised perturbations of velocity at reference point u'_r/\bar{u}_r and heat release Q'/\bar{Q} during one period of oscillations (excitation at 240 Hz with amplitude 70%).

Table 3.2: Coefficients of the RTL FTF model (Eq. 3.3)

j	$n_{f,j}$	$\omega_{0,j}$	ξ_j
1	1.169	2160	0.461
2	1.156	1267	1.612
3	-3.232	1073	0.455

where $n_{f,j}$ is a dimensionless constant, $\omega_{0,1}$ is the cut-off frequency of the second-order low-pass filter, ξ_j is the damping ratio, $\omega_{0,2}$ and $\omega_{0,3}$ are band-pass frequencies, τ_f is the time delay of the model. Optimum values of the coefficients of Eq. 3.3 are computed using least-squares method and are listed in Tab. 3.2; the optimum time delay for the flame model is $\tau_f = 1.163 \cdot 10^{-3} s$. Note that second-order low-pass filter and band-pass filters contribute significantly to the phase of the FTF model 3.3 (see [99]). Thus, τ_f is not the only parameter influencing the FTF phase. The resulting FTF model is shown in Fig. 3.16 together with the FTF calculated from simulations.

3.3.2 Time-lag distributed FTF models

In this section the FTF model 3.4 proposed by Tay-Wo-Chong et al. [65] is used. With respect to the original FTF model of Komarek and Polifke [36] described by Eq. 2.65, Tay-Wo-Chong et al. [65] introduced the dimensionless parameter $a = 1.05$ that gives a better agreement with the measured FTF:

$$FTF_{mod\ TLD}(\omega) = e^{-i\omega\tau_1 - 0.5[\omega\sigma_1]^2} + a \left(e^{-i\omega\tau_2 - 0.5[\omega\sigma_2]^2} - e^{-i\omega\tau_3 - 0.5[\omega\sigma_3]^2} \right). \quad (3.4)$$

Optimal values of parameters τ_j and σ_j calculated using the method of least squares for the experimentally obtained FTF and for the FTF computed from simulations are presented in Tab. 3.3. The corresponding model of the FTF is shown in Fig. 3.17.

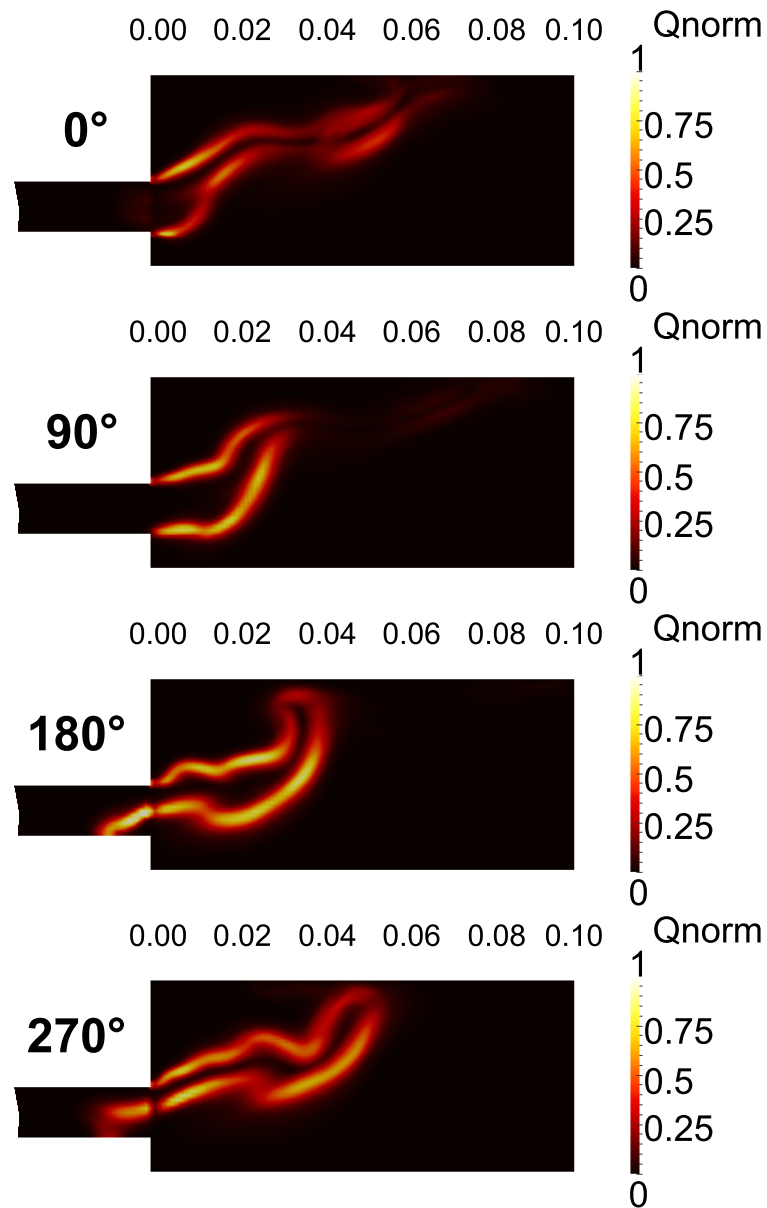


Figure 3.13: Heat release distribution in the setup at different phases of a period of oscillations (excitation at 240 Hz with amplitude 70%).

Table 3.3: Values of parameters τ_j and σ_j for the TLD model of the experimental and numerical FTFs, ms.

	τ_1	σ_1	τ_2	σ_2	τ_3	σ_3
Experiment	2.79	0.88	4.88	0.52	6.76	1.48
Simulations	2.43	0.93	4.40	0.73	6.25	1.33

3. Application of the three-step approach to a laboratory, perfectly premixed, setup

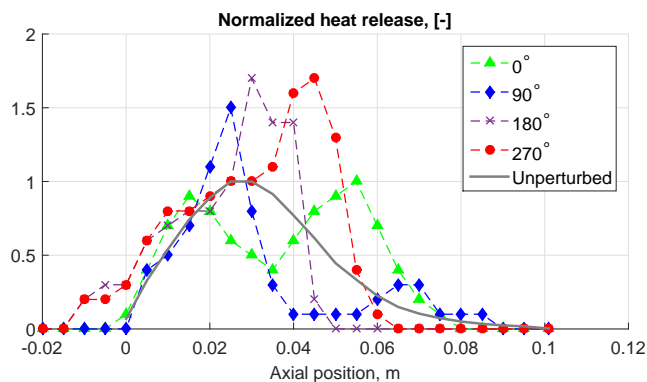


Figure 3.14: Heat release distribution at four instances of one period of oscillations (excitation at 240 Hz with amplitude 70%) and heat release distribution in the setup without perturbation.

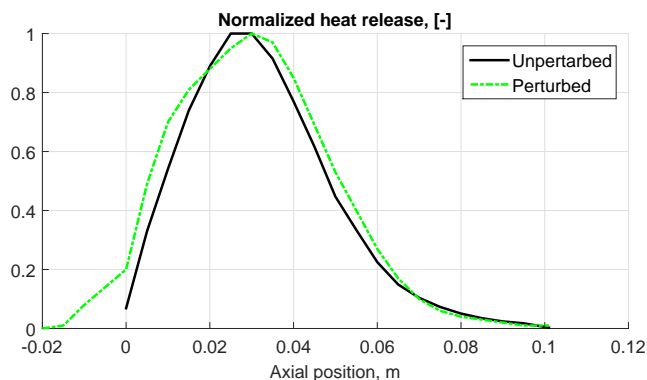


Figure 3.15: Heat release distribution in the setup without perturbation and heat release distribution averaged over one period of oscillations (excitation at 240 Hz with amplitude 70%).

3.3. ANALYTICAL MODELS FOR THE FDF

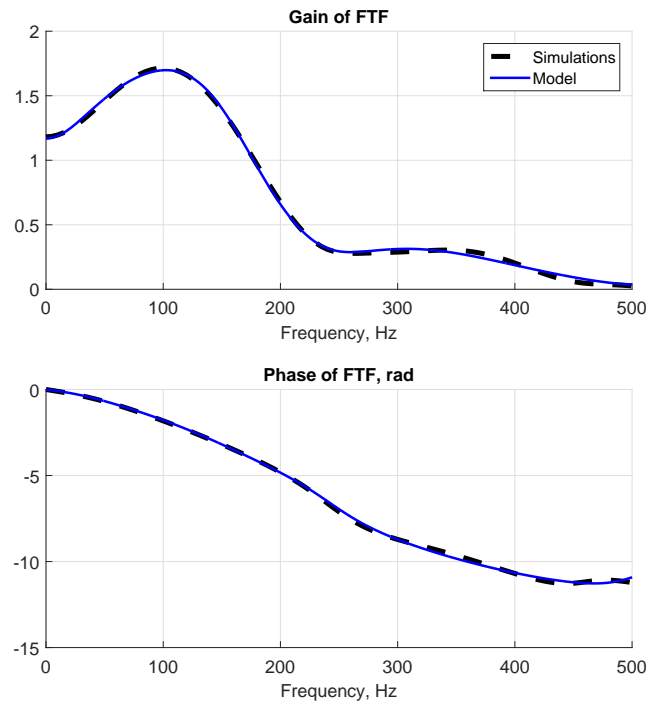


Figure 3.16: FTF of the BRS test rig calculated from OpenFOAM simulations and its RTL FTF model (Eq. 3.3).

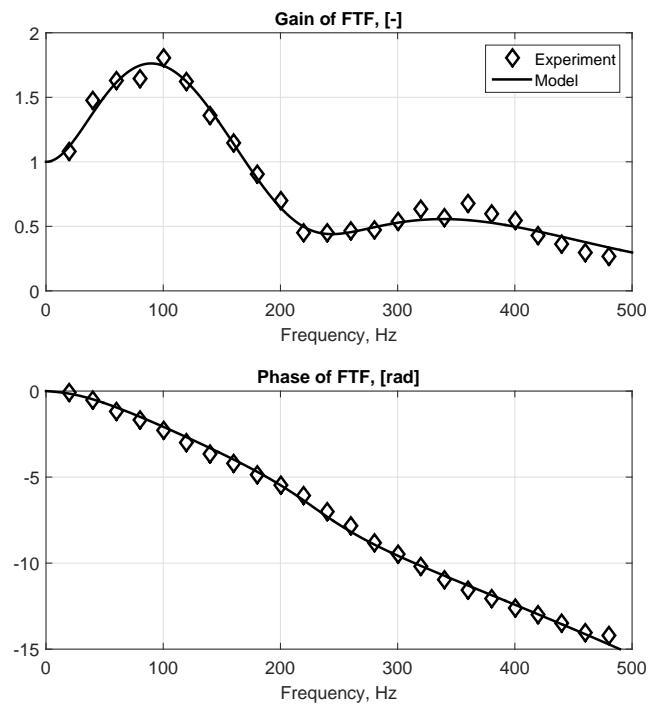


Figure 3.17: Experimental FTF of BRS and its TLD model.

3. Application of the three-step approach to a laboratory, perfectly premixed, setup

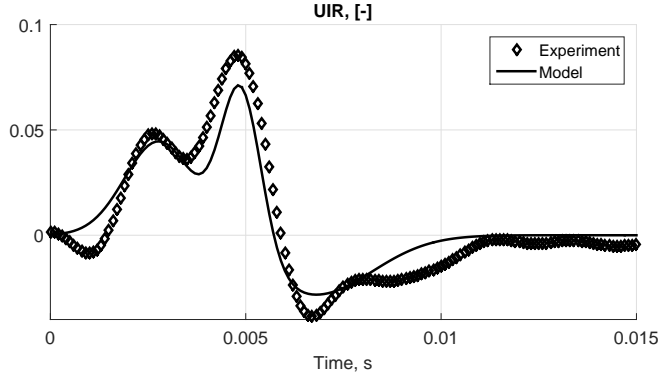


Figure 3.18: UIR computed from the experimental FTF [9] and modelled by Eq. 3.5.

The analytical form of the UIR corresponding to the FTF model 3.4 is

$$UIR_{mod\ TLD}(t) = \frac{1}{\sigma_1\sqrt{2\pi}}e^{-\frac{1}{2}\left(\frac{t-\tau_1}{\sigma_1}\right)^2} + a \left(\frac{1}{\sigma_2\sqrt{2\pi}}e^{-\frac{1}{2}\left(\frac{t-\tau_2}{\sigma_2}\right)^2} - \frac{1}{\sigma_3\sqrt{2\pi}}e^{-\frac{1}{2}\left(\frac{t-\tau_3}{\sigma_3}\right)^2} \right). \quad (3.5)$$

The UIR computed from the experimental FTF and its model 3.5 are shown in Fig. 3.18.

To understand the influence of the heat release distribution on the FTF, we need to recover meaning of the parameters τ_1 , τ_2 and τ_3 from section 2.2.1. The parameter τ_1 model the time that fluid particles spend while traveling from the flame holder to the flame. Thus, $\tau_1 \propto \frac{x_{fl}}{u_{fh}}$, where x_{fl} is the position of the peak of the heat release distribution and u_{fh} is the axial velocity at the flame holder. Indeed, the difference between τ_1 parameter in the experimental and the numerical FTFs (see Tab. 3.3) is 15% that corresponds to the difference of the heat release distributions shown in Fig. 3.6.

The parameters τ_2 and τ_3 model the time that fluid particles spend to travel from the swirler to the flame. Thus, they can be decomposed into time that fluid particles spend to travel from the swirler to the flame holder τ_{sw-fh} and the time that fluid particles spend to travel from the flame holder to the flame $\tau_{j\ fh-fl}$. The first component τ_{sw-fh} is indifferent to the heat release distribution. Thus, it is equal for both τ_2 and τ_3 and for both experimental and the numerical FTFs:

$$\tau_{sw-fh} = \frac{L_{sw-fh}}{u_{fh}} = \frac{0.03}{11.3} = 2.65 \cdot 10^{-3}\text{s}. \quad (3.6)$$

The remaining components $\tau_{j\ fh-fl}$ are calculated subtracting the τ_{sw-fh} from the τ_j values reported in Tab. 3.3, and are reported in Tab. 3.4. The differences between $\tau_{2\ fh-fl}$ and $\tau_{3\ fh-fl}$ parameters in the experimental and the numerical FTFs (see Tab. 3.4) are 27% and 14% respectively. That corresponds to the difference of the heat release distributions shown in Fig. 3.6.

Table 3.4: Values of parameters τ_j $_{fh-fl}$ for the TLD model of the experimental and numerical FTFs, ms.

	τ_2 $_{fh-fl}$	τ_3 $_{fh-fl}$
Experiment	2.23	4.11
Simulations	1.75	3.60

3.3.3 Time-lag distributed FDF model

Idea of introducing the dependence of the FTF model parameters on the amplitude of velocity oscillations was expressed by Heckl [47, 109] and by Li and Morgans [54]. In both works laminar flames were discussed. Heckl [47, 109] used extended $n - \tau$ model to describe the experimentally measured FDF. That model does not accounts the filtering flame behaviour at high frequencies. In the FDF model of Li and Morgans [54], the standard $n - \tau$ model was extended by a low-pass filter. However, the relative decrease of the FTF gain is assumed to be equal for all the frequencies that is not fully representative of the real configuration.

In this work, the FTF model for the perfectly-premixed swirl stabilised flames 3.4 is extended to the nonlinear regime introducing the dependence of its parameters on the amplitude of the velocity perturbations upstream of the flame

$$FDF_{mod\ TLD}(\omega, A) = e^{-i\omega\tau_1(A)-0.5[\omega\sigma_1(A)]^2} + a \left(e^{-i\omega\tau_2(A)-0.5[\omega\sigma_2(A)]^2} - e^{-i\omega\tau_3(A)-0.5[\omega\sigma_3(A)]^2} \right), \quad (3.7)$$

where $A = \max(|u'_r|)/\bar{u}_r$ is the normalised amplitude of velocity oscillations at the reference position.

First, optimal values of parameters τ_j and σ_j are calculated for each amplitude of velocity perturbations using the method of least squares. The obtained values of parameters τ_j and σ_j for different amplitudes of perturbation are presented in Tab. 3.5 and shown in Fig. 3.20; the corresponding FDF model is shown in Fig. 3.19. All τ_i decrease when increasing A . This trend is explained by the flame shift towards the swirler when it is forced by excitation with high amplitudes. The increase of σ_2 and σ_3 while increasing A is explained by higher dispersion of the flame along the longitudinal axis when applying high-amplitude excitation (see Fig. 3.15) with respect to the heat release distribution when low-amplitude excitation is applied. The decrease of the parameter σ_1 when increasing A can be explained by the decrease of the parameter τ_1 .

Second, the dependencies of τ_i and σ_i on the normalised amplitude of velocity perturbations A are modelled as

$$\tau_j = \tau_{j,lin}(1 + \Theta_j A^2), \quad (3.8)$$

$$\sigma_j = \sigma_{j,lin}(1 + \Sigma_j A), \quad (3.9)$$

3. Application of the three-step approach to a laboratory, perfectly premixed, setup

Table 3.5: Values of parameters τ_j and σ_j for different amplitudes of perturbation in simulations, ms

Amplitude	τ_1	σ_1	τ_2	σ_2	τ_3	σ_3
10%	2.43	0.93	4.40	0.73	6.25	1.33
30%	2.47	0.92	4.18	0.73	5.71	1.81
50%	2.33	0.78	3.98	0.77	5.27	2.38
70%	1.95	0.73	3.60	0.77	3.35	2.44

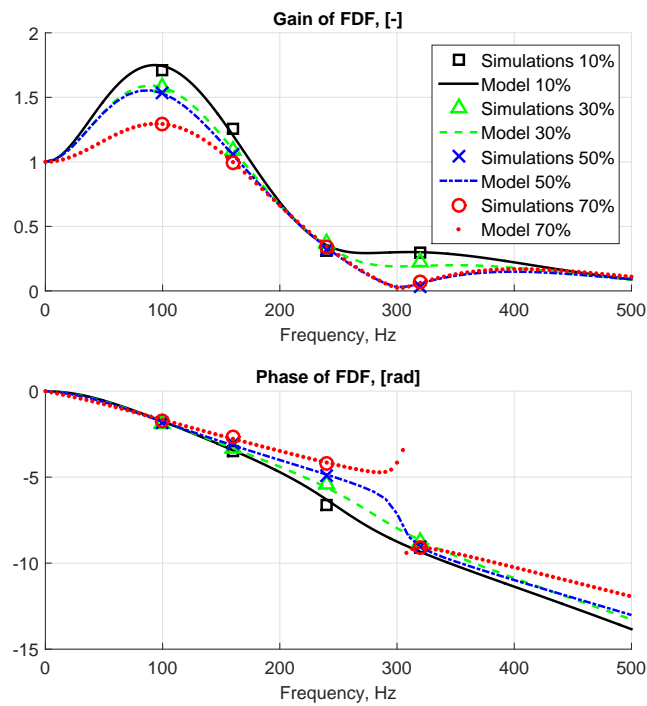


Figure 3.19: FDF of BRS setup modelled with Eq. 3.7.

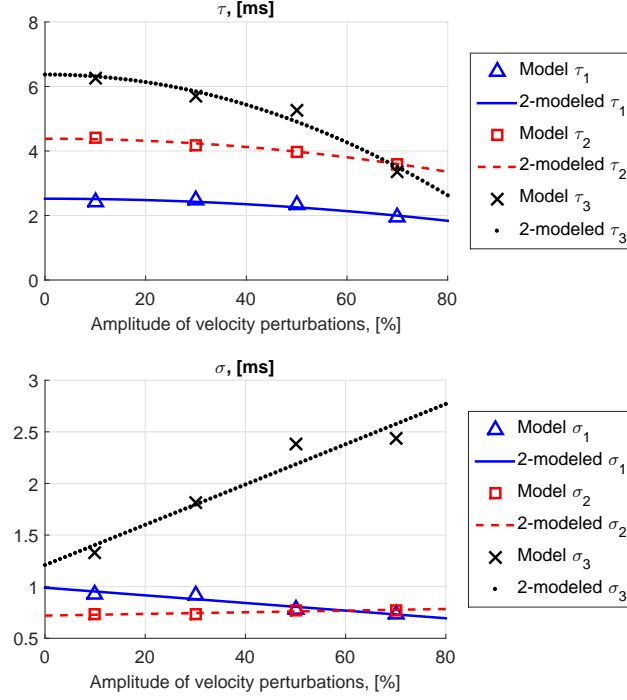


Figure 3.20: Dependencies $\tau_j(A)$ and $\sigma_j(A)$ from Tab. 3.5 (points, 'Model') and modelled by Eqs. (3.8)-(3.9) (lines, '2-modeled').

where parameters $\tau_{j,lin}$ and $\sigma_{j,lin}$ determine the FDF in the linear regime when $A = 0$, and dimensionless parameters Θ_j and Σ_j determine the relative change of the parameters τ_j and σ_j respectively when the excitation of $A = 1$ is applied.

Quadratic dependency of τ_j on A is chosen because it gives smaller values of root-mean-square errors than a linear dependence. For $\sigma_j(A)$ a linear dependency gives the smallest root-mean-square errors. Optimal values of parameters $\tau_{j,lin}$, Θ_j , $\sigma_{j,lin}$ and Σ_j are computed using the least squares method and are listed in Table 3.6. The resulting functions are shown in Fig. 3.20. Note that values of $\tau_{j,lin}$ and $\sigma_{j,lin}$ are close to the values of τ_j and σ_j for 10% excitation (see Tab. 3.5).

Table 3.6: Values of parameters $\tau_{j,lin}$, Θ_j , $\sigma_{j,lin}$ and Σ_j in the TLD FDF model.

j	$\tau_{j,lin}$, ms	Θ_j	$\sigma_{j,lin}$, ms	Σ_j
1	2.52	-0.42	0.99	-0.37
2	4.38	-0.37	0.72	0.11
3	6.37	-0.92	1.21	1.61

The physical meaning of dependencies of parameters τ_j and σ_j on A is understood if the frequency domain representation of the FDF is switched to

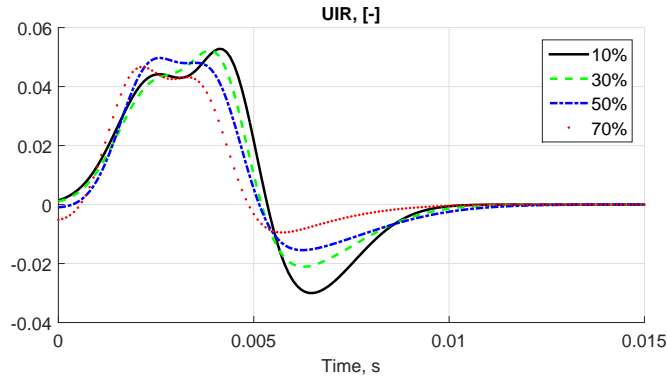


Figure 3.21: UIRs for different amplitudes of velocity excitations modelled by Eq. (3.5).

the time domain representation, i.e. to the UIR. Eq. 3.5 models the response of the heat release to acoustic oscillations with the help of three Gaussians with peaks at τ_j and standard deviations σ_j .

The UIRs for different amplitudes of velocity excitation are shown in Fig. 3.21. As it can be observed, higher velocity perturbations amplitudes cause the flame response peaks to occur mildly earlier in time. Furthermore, the overall response duration remains almost the same for the 4 excitation amplitudes considered.

As it is already mentioned in section 3.2.3, high-amplitude velocity excitations intensify the turbulence of the flow and shift the peak of the heat release distribution towards the swirler (see Fig. 3.15). This causes the flame response peaks in the UIR (see Fig. 3.21) to occur earlier in time. Moreover, the length of the non-zero heat release distribution remains almost unchanged. That is why the overall response duration remains almost the same for the 4 amplitudes considered.

Note that the proposed FDF model consists of only 6 parameters. The FDF at certain excitation amplitude computed for 3 frequencies gives 6 equations for the FDF model parameters estimation: 3 equations for the FDF gain and 3 equations for the FDF phase. From the mathematical point of view, it is possible to find optimum model parameters knowing the FDF just at 3 frequencies. With 4 frequencies, as used in the present work, the problem of the optimum parameters search becomes even overestimated improving the reliability of the obtained results. Thus, using the proposed FDF model it is possible to reduce the number of time-consuming CFD simulations for the FDF calculation that is the advantage of this FDF model.

The calculation of the instantaneous normalised amplitude of velocity oscillations at the reference position A is a challenge when using the FDF in the time domain simulations. In this work, the instantaneous value of A is computed as the maximum value of the normalised amplitude of velocity oscillations $\max(|u'_r|)/\bar{u}_r$ in a window of time that precedes the current instant of the simulation. This approach is robust and is computationally inexpen-

sive. For the setup in this section the time window is taken 25 ms that allows to compute the normalised amplitude of velocity oscillations for frequencies higher than 20 Hz. Smaller length of the time window may be required if the dynamics of the thermoacoustic system is very fast and the unstable frequency of the pressure oscillations is high. Examples of A time histories for a stable and for an unstable cases are presented in Section 3.4.3.

3.4 Network model simulations

3.4.1 Numerical setup

The network model numerical setup consists of 6 sections, 3 jump conditions with pressure losses, one jump condition at the flame and 2 boundary conditions, as shown in Fig. 3.22. The cross-section area, length and temperature of each section are listed in Tab. 3.7. Jump matrices to connect waves between sections are calculated using systems of Eqs. 2.100 and 2.113. The reflection coefficient of the inlet (see Eq. 2.116) is $R_{inlet} = 1$ unless another value is specified. The outlet reflection coefficient defined in Eq. 2.117 is $R_{outlet} = -0.4$ approximated from the values reported by [9], unless otherwise specified. The total length of the combustor (sum of the lengths of Sections 5 and 6) $L_{c.c.}$ is variable. Acoustic losses at area changes between the plenum and the burner duct and between the burner duct and the combustor are taken into account by pressure losses coefficients $\zeta_{decr} = 0.487$ and $\zeta_{incr} = 0.756$ respectively, calculated by formulae 2.93 and 2.104. Acoustic losses at the swirler are taken into account by the pressure loss coefficient $\zeta_{swirler} = 2.073$ calculated from the unperturbed OpenFOAM simulations. The active flame, i.e. the unsteady heat release, in the low-order network model is positioned at $x_{fl} = 0.03$ m between Sections 5 and 6. This value corresponds to the maximum of the heat release in the longitudinal direction in OpenFOAM simulations (see Fig. 3.6). Time step in the network model simulations is 10^{-5} s that is smaller than any acoustic time lag in any Section of the network model.

The velocity fluctuations for the unsteady heat release model are taken between Sections 3 and 4 that corresponds to the velocity probe position in the simulations. The instantaneous unsteady heat release is calculated as the convolution of the history of velocity fluctuations and the Unit Impulse Response

$$Q'(t) = \frac{\bar{Q}}{\bar{u}} \int_0^\infty UIR_u^{mod}(t' - t)u'(t)dt'. \quad (3.10)$$

where t' is the integration variable.

The mean temperature is the same in the first five sections. The temperature gradient coincides with the position of the active flame and is situated at the border between Sections 5 and 6. On the one hand, the temperature in Section 6 should be equal to the adiabatic temperature of the flame (1960 K) that is observed in the inner recirculation zone in the OpenFOAM simulations (see Fig. 3.4). In this case the temperature gradient at the flame is modelled correctly that is important for the stability prediction [31]. On the other hand,

3. Application of the three-step approach to a laboratory, perfectly premixed, setup

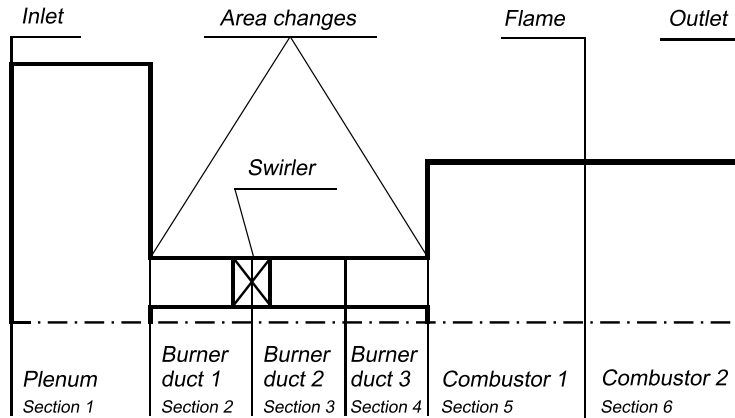


Figure 3.22: Scheme of BRS network model numerical setup.

Table 3.7: Default values of parameters imposed in the network model.

N	Section	Area, m ²	Length, m	Temperature, K
1	Plenum	$3.146E-2$	0.17	300
2	Burner duct 1	$1.056E-3$	0.135	300
3	Burner duct 2	$1.056E-3$	0.025	300
4	Burner duct 3	$1.056E-3$	0.02	300
5	Combustor 1	$8.1E-3$	$x_{fl} = 0.03$	300
6	Combustor 2	$8.1E-3$	$L_{c.c.} - x_{fl}$	1712/1930

the value of the mean temperature in Section 6 should take into account heat losses of the test rig. In the second case, time for the acoustic wave to travel from the flame to the outlet and backwards is computed correctly.

The thermoacoustic analysis using a network model is computationally inexpensive and several analyses with different values of the parameters can be made. The first value of the temperature in Section 6, $T_{comb\ 2}=1930$ K, is taken from the work by Tay-Wo-Chong et al. [9]. This value is close to the adiabatic temperature of the flame. Considering the case with the value of the temperature in Section 6, 1930 K renders possible the comparison of our results with the results of [9]. The second value of the temperature in Section 6 is $T_{comb\ 2}=1712$ K. This value is the average temperature at the outlet of the computational domain in the OpenFOAM simulation and takes into account heat losses of the setup. The influence of the temperature in Section 6 is addressed later in section 3.4.3.

3.4.2 Results of the linear analysis

Rational time-lag FTF model 3.3 gives the very good approximation of the computed FTF (see Fig. 3.16). Moreover, time domain simulations with this FTF model are two orders of magnitude faster than with the time-lag distributed model 3.4. Thus, for the linear analysis the RTD FTF model 3.3 is used.

The temperature in Section 6 is taken equal to $T_{comb\ 2}=1930$ K, to compare the present results with the results of Tay-Wo-Chong et al. [9].

The setup is excited at the inlet for the first $t_{exc}=0.1$ s by a broadband signal in the range $0 \div 1$ kHz with maximum amplitude of 5 Pa. After 0.1 s and until 0.3 s, the system is left to evolve by itself without external excitation. The parameter called growth rate is calculated; it provides information about the mode stability. It is possible to calculate the growth rate from the time domain simulations assuming the following law for the pressure perturbations

$$p'(t) = \sum_{i=1}^n P_i \sin(2\pi f_i t + \phi_i) e^{\alpha_i(t-t_{exc})}, \quad (3.11)$$

where f_i is one of the frequencies of pressure oscillations after t_{exc} , n is the number of the frequencies of pressure oscillations after t_{exc} , P_i is the amplitude of pressure oscillations at f_i at the time t_{exc} , ϕ_i is the phase of the pressure oscillations at f_i , α_i is the growth rate of the mode f_i .

The frequencies of oscillations and their growth rates are computed by approximating time history of pressure oscillations by Eq. 3.11 using the least-squares method. In the simulations presented in this chapter no more than two unstable frequencies per run are detected, thus $n = 2$ for all simulations in the network model in this chapter. Positive values of the growth rate parameter α indicate that the system is unstable, and the negative values of α mean that the system is stable.

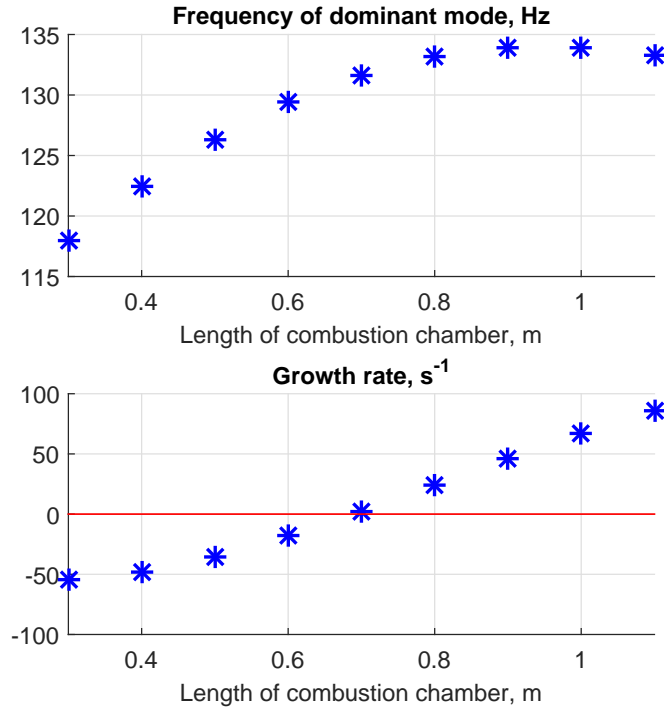


Figure 3.23: Dominant frequency of oscillations and its growth rate for various lengths of the combustion chamber; $x_{fl} = 0.03$ m, $k_G = 1$, $\tau_{add} = 0$ ms.

Validation against experimental data

An unstable frequency at 101.3 Hz was detected in the experiments [9] with a combustor length of 0.7 m. With a length of the combustor equal to 0.3 m the setup was stable [65]. A parametric study with different values of the combustion chamber length in the range $0.3 \div 1.1$ m, with steps of 0.1 m, is performed here. For values of the combustion chamber length below 0.6 m the setup is stable (see Fig. 3.23). For combustion chamber lengths equal or higher than 0.7 m the setup is unstable. Thus, our simulations predict the setup with the length of combustion chamber $L_{c.c.} = 0.3$ m to be stable and with $L_{c.c.} = 0.7$ m to be unstable as in the experiments. Particularly, it explains why the experimental setup was stable when the FTF was computed with $L_{c.c.} = 0.3$ m.

The computed frequency does not correspond to any of the acoustic modes of the setup but is a 'flame intrinsic mode' as defined by Bomberg et al. [110], an 'Intrinsic Thermo-Acoustic (ITA)' mode defined by Silva et al. [31] or a 'mode associated with the flame model' as defined by Dowling and Stow [30]. The brief explanation of the ITA mode formation is given in Figure 3.24. The heat release perturbations \dot{Q}' according to Eq. 2.113 produce acoustic waves and one of them, g_5 , travels upstream to the junction between the combustor and the burner tube. At this junction, according to Eq. 2.100, one part of the acoustic wave g_5 transforms into the wave g_4 that travels to the reference

velocity plane. At this plane, the acoustic wave g_4 contributes to the velocity perturbations u'_r that produce heat release oscillations through the FTF. At this point, the loop is closed; since this loop can exist even with the zero reflection coefficients [31], the acoustic mode produced as a result of this interaction is called intrinsic. Nevertheless, it does not imply that acoustics of the setup does not influence the frequency and the stability of the intrinsic mode. The more detailed explanation of the ITA mode formation can be found in the work of Bomberg et al. [110].

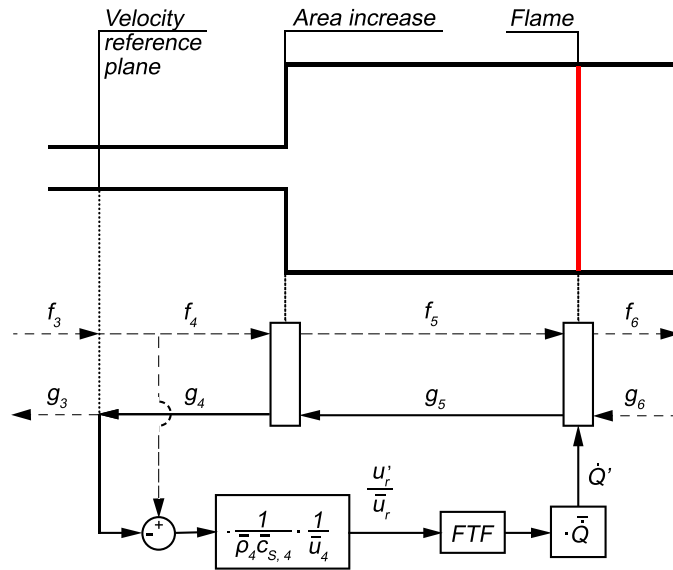


Figure 3.24: Scheme of formation of ITA modes.

The unstable frequency 131 Hz computed in this work with the length of combustion chamber of 0.7 m and $T_{comb,2} = 1930$ K differs from the value 101.3 Hz observed in the experiment [9] with the same length of the combustor. This is explained by the difference in the phase of the FTF in the experiment and in our simulations and by the very high sensitivity of ITA modes frequency to the phase of the FTF, as it is shown further.

The FSC model that is used in this work is adiabatic as well as the Turbulent Flame Closure (TFC) model used by Tay-Wo-Chong et al. [9]. However, using the FTF computed with the URANS simulations and the TFC model predicted the BRS test rig to be unstable only with the total combustor length equal or higher than 1 m. Thus, it can be concluded that the FSC model is more in agreement with the experiments than the TFC model. The unstable frequency obtained by Tay-Wo-Chong et al. [9] is also higher than the one detected in experiments. It is mentioned by Tay-Wo-Chong et al. [9] that three parameters were different for the experimental measurements and the URANS simulations with the TFC model: the position of the maximum heat release of unperturbed case (denoted here as x_{fl}), the gain and the phase of the FTF

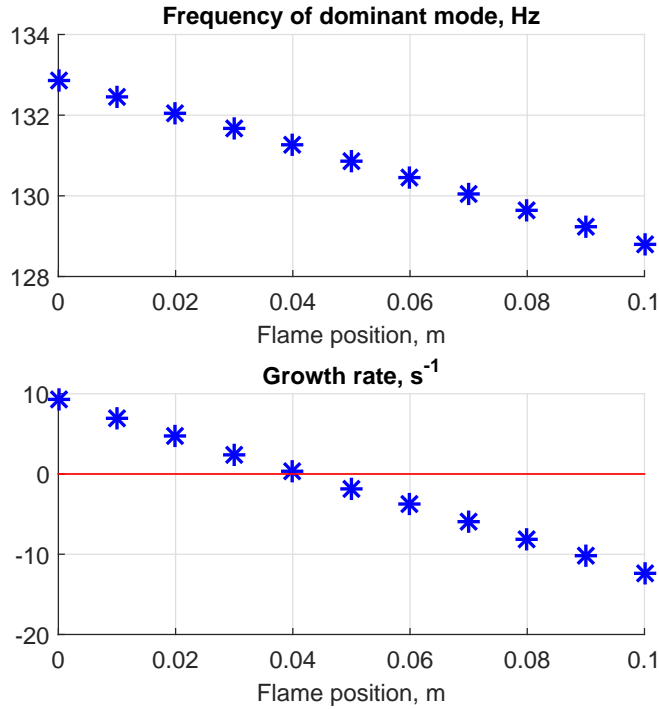


Figure 3.25: Dominant frequency of oscillations and its growth rate for various positions of the flame; $L_{c,c} = 0.7$ m, $k_G = 1$, $\tau_{add} = 0$ ms.

around the unstable frequency. To investigate these aspects, parametric analysis varying the position of the unsteady heat release, the gain and the phase of the FTF in the network model are performed. We are aware of the strong connection between the heat release distribution and the phase of the FTF. However, the direct effect of heat release distribution, i.e. the flame position in the network model, and its indirect effect, i.e. the phase of the FTF, on the stability are studied separately in this work to understand each effect.

Sensitivity to the flame position

The parameter x_{fl} is varied in the range $0 \div 0.1$ m with steps of 0.01 m keeping fixed the length of the combustion chamber, $L_{c,c} = 0.7$ m, and the FTF. This range corresponds to the heat release distribution in the longitudinal direction (see Fig. 3.6). As it can be seen from Figure 3.25, the thermoacoustic system is unstable for values of x_{fl} smaller or equal to 0.04 m. When increasing the x_{fl} parameter, the frequency of the dominant mode of the setup slightly decreases.

Sensitivity to the gain of FTF

To study the influence of the gain and the phase of the FTF on the stability of the setup the modified version of the model for the FTF is introduced:

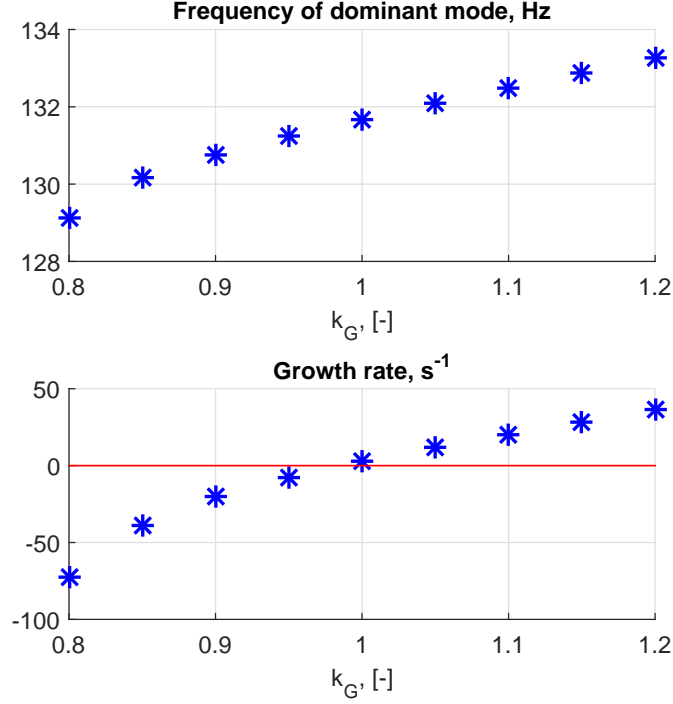


Figure 3.26: Dominant frequency of oscillations and its growth rate for various values of the parameter k_G parameter; $L_{c.c} = 0.7$ m, $x_{fl} = 0.03$ m, $\tau_{add} = 0$ ms.

$$FTF_{mod\ RTL\ 2}(\omega) = k_G FTF_{mod\ RTL}(\omega) e^{-i\omega\tau_{add}}, \quad (3.12)$$

where k_G is the dimensionless parameter responsible for the change of the gain of the FTF and τ_{add} is the additional time delay responsible for the change of the phase of the FTF.

The parameter k_G is changed in the range $0.8 \div 1.2$ with steps of 0.05. It is seen from Fig. 3.26 that the setup is stable for values of k_G lower than 1, i.e. lower values of the gain of the FTF. This could be the main reason of discrepancy between experimental data and the stability analysis with the FTF calculated with the URANS simulations and the TFC model [9]. The dominant frequency of the oscillations of the setup grows slowly when k_G increases.

Sensitivity to the phase of FTF

We vary the parameter τ_{add} in the range $-1.0 \div 2.0$ ms in steps of 0.2 ms. The lower limit of this range is set by the value τ_f . The setup is unstable for higher values of τ_{add} , i.e. higher absolute values of the phase of the FTF, as it can be seen from Fig. 3.27. The dominant frequency of the oscillations decays significantly when τ_{add} increases. The unstable frequency 100.3 Hz corresponds to the value of the parameter $\tau_{add} = 1.6$ ms. Almost the same frequency

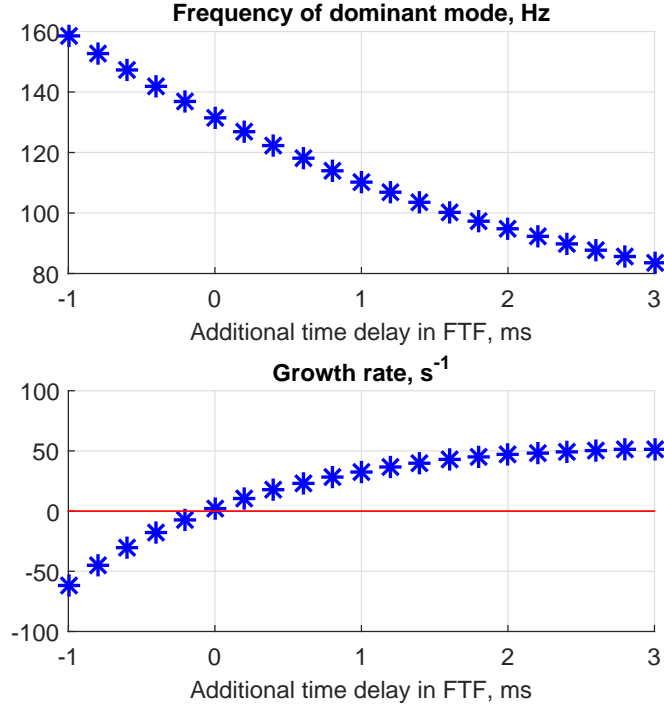


Figure 3.27: Dominant frequency of oscillations and its growth rate for various values of the parameter τ_{add} ; $L_{c.c} = 0.7$ m, $x_{fl} = 0.03$ m, $k_G = 1$.

101.3 Hz was retrieved experimentally. This happens because the phase of the FTF obtained numerically is underestimated with respect to the experimental one. Adding an artificial time delay to the FTF obtained numerically shifts the phase of the FTF closer to the experimental one.

Combined sensitivity to the flame length and the FTF phase

Next, the influence of the simultaneous change of the flame position in the network model and the FTF phase on the stability is studied. The change of the FTF phase τ_{add} is assumed to be dependent on the change of the flame position in the network model Δx_{flame} as

$$\tau_{add} = \frac{\Delta x_{flame}}{\bar{u}_r}, \quad (3.13)$$

where $\bar{u}_r = 11.3$ m/s. The length of the network model section *Combustor 1* is calculated as $x_{flame} = 0.03 + \Delta x_{flame}$. The dependence of the frequency of the dominant mode and its growth rate on both the flame location in the network model and the FTF phase are shown in Figure 3.28. $\Delta x_{flame} = 0.015$ ms is characterised with the unstable frequency 104.1 Hz that is close to the frequency 101.3 Hz retrieved experimentally.

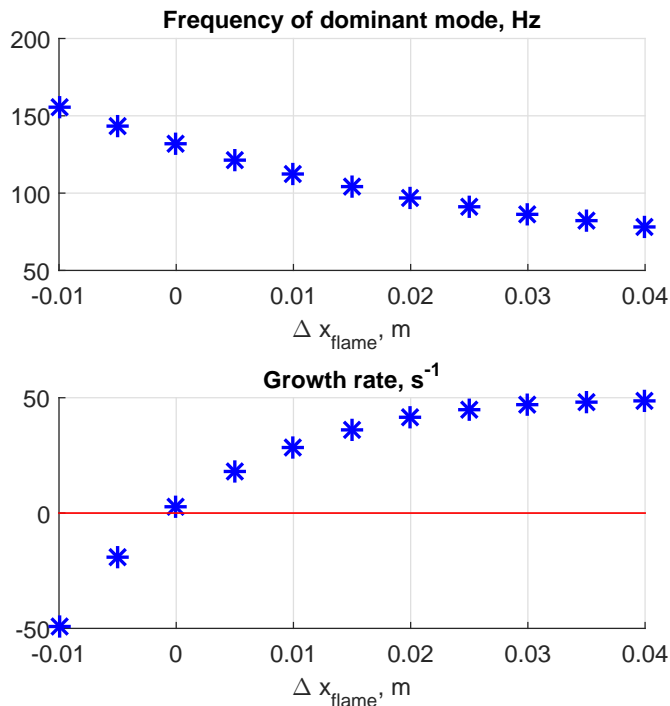


Figure 3.28: Dominant frequency of oscillations and its growth rate for various values of Δx_{flame} parameter; $L_{c.c} = 0.7$ m, $k_G = 1$, $\tau_{add} = \Delta x_{flame}/\bar{u}_r$.

Sensitivity to the combustion chamber length and the outlet reflection coefficient

It is important to find ways to suppress combustion instabilities at the ITA frequencies. To accomplish this task, the parametric analysis is performed for lengths of combustion chamber in a wider range than presented in Fig. 3.23, for various reflection coefficients, plenum lengths and plenum cross-sectional areas.

First, a parametric analysis is performed for length of the combustion chamber in the range $0.3 \div 10$ m and three values of the outlet reflection coefficient $R_{out} = \{-0.4, 0, 0.4\}$. The results are presented in Fig. 3.29. For the zero value of the outlet reflection coefficient the unstable frequency of the setup is 117 Hz with the growth rate $83 s^{-1}$ in the whole range of the combustion chamber lengths.

For a value of the outlet reflection coefficient $R_{out} = -0.4$ when increasing the length of the combustion chamber from 0.3 m till 1.0 m, the unstable frequency increases from 118 Hz to 134 Hz. As $L_{c.c.}$ increases till 3.9 m, the unstable frequency decreases to 103 Hz. In the range of the combustion chamber lengths $0.3 \div 2.0$ m the growth rate grows from $-54 s^{-1}$ to $149 s^{-1}$. As the length of the combustion chamber increases to 3.9 m, the growth rate decreases to $17 s^{-1}$. For a length of the combustion chamber equal to 4.0 m the unstable mode changes suddenly its frequency from to 103 Hz to 130 Hz.

3. Application of the three-step approach to a laboratory, perfectly premixed, setup

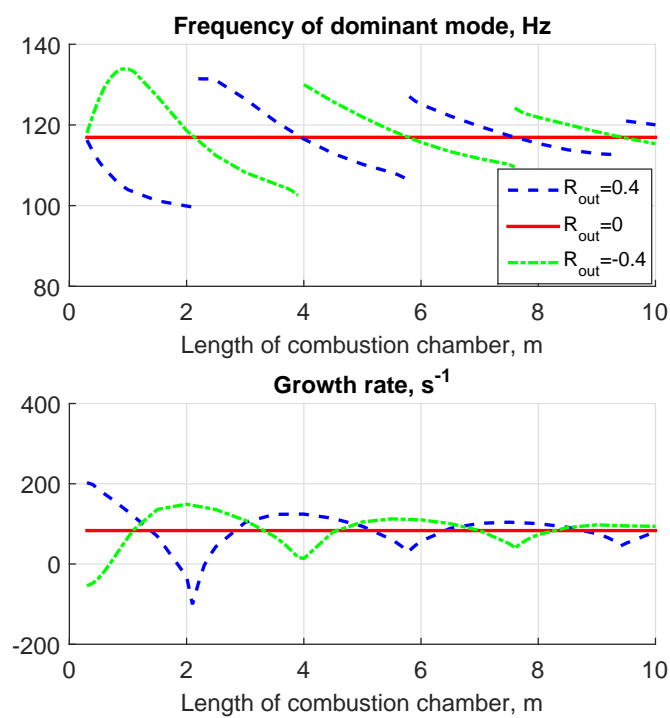


Figure 3.29: Dominant frequency of oscillations and its growth rate for various combustion chamber length and three values of the outlet reflection coefficient.

Further increase of $L_{c.c.}$ up to 7.6 m results in a monotonic decrease of the unstable frequency to 110 Hz. The growth rate increases in the range of the combustion chamber length $4.0 \div 5.5$ m and decreases in the range of the combustion chamber length $5.5 \div 7.6$ m. At $L_{c.c.} = 7.6$ m the frequency jump occurs again. The frequency jump occurs every $\Delta L_{c.c.} = 3.6$ m that corresponds to half the wavelength of the mode at frequency 118 Hz, for a temperature of Section 6 equal to $T_{comb\ 2} = 1930$ K.

Similar behaviour is observed for a value of the outlet reflection coefficient $R_{out} = 0.4$. For the length of the combustion chamber from 0.3 m till 2.1 m, the unstable frequency decreases with its growth rate. At $L_{c.c.} = 2.2$ m the frequency jump occurs and the further increase of the combustion chamber length results in a monotonic decrease of the dominant frequency; its growth rate first increases and then decreases. Next frequency jumps occur at $L_{c.c.} = 5.8$ m and $L_{c.c.} = 9.5$ m with the same periodicity $\Delta L_{c.c.} = 3.6$ m as for $R_{out} = -0.4$.

The influence of the outlet reflection coefficient on the stability is studied. Similar analyses have been done by Emmert et al. [111] for $L_{c.c.} = 0.7$ m and by Silva et al. [112] for $L_{c.c.} = 0.3 \div 0.7$ m. In this work, this analysis is extended to three other values of the combustion chamber length $L_{c.c.} = \{0.7, 2.2, 3.0\}$ m. The results are present in Fig. 3.30.

For $L_{c.c.} = 0.7$ m the frequency of the dominant mode decreases monotonically when increasing the value of the reflection coefficient, in particular when the reflection coefficient changes its sign. The growth rate of the dominant mode increases while increasing the value of the reflection coefficient in the whole range studied $R_{out} = -0.7 \div 1$. The dominant mode is unstable for $R_{out} = -0.4 \div 1$.

For $L_{c.c.} = 2.2$ m the frequency of the dominant mode increases monotonically when increasing the value of the reflection coefficient in the range $R_{out} = -1 \div 0.7$. For values of the reflection coefficient in the range $R_{out} = -1 \div 0.4$, the growth rate decreases. The dominant mode is stable for $R_{out} = 0.4 \div 0.7$.

For $L_{c.c.} = 3.0$ m the frequency of the dominant mode increases monotonically when increasing the value of the reflection coefficient in the whole range $R_{out} = -1 \div 1$. The growth rate decreases for negative values of the outlet reflection coefficients and increases for positive values. The dominant mode is unstable in the whole range of outlet reflection coefficients.

It is common practice to decrease the absolute value of the reflection coefficient to suppress combustion instabilities. However, as shown in Fig. 3.30, this technique generally does not work with ITA modes and some cases could even lead to an increase of the growth rate of the ITA mode.

Sensitivity to the plenum length and the inlet reflection coefficient

Next, a parametric analysis is performed for a length of the plenum in the range $0.1 \div 10$ m and three values of the inlet reflection coefficient $R_{in} = \{-1, 0, 1\}$. To eliminate the influence of the combustion chamber acoustics, the outlet reflection coefficient was taken to vanish, i.e. $R_{out} = 0$. Results are presented in Fig. 3.31. For a zero value of the inlet reflection coefficient the unstable

3. Application of the three-step approach to a laboratory, perfectly premixed, setup

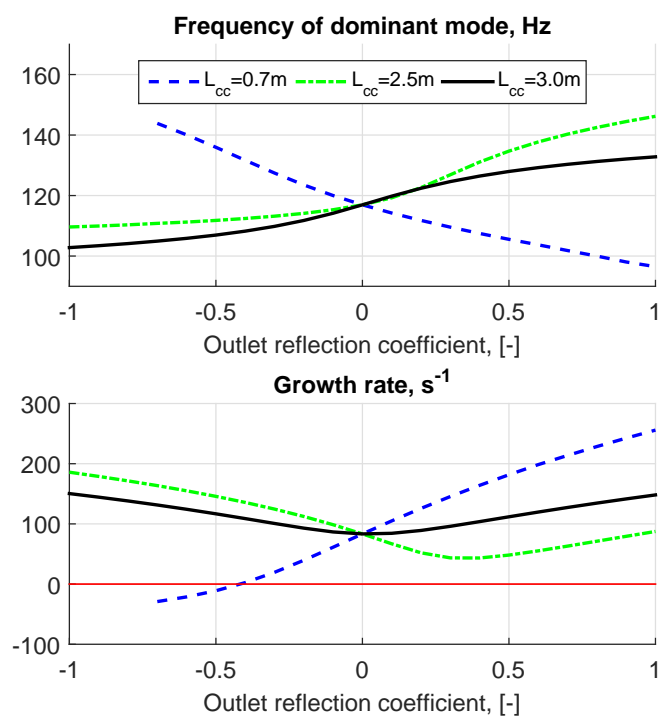


Figure 3.30: Dominant frequency of oscillations and its growth rate for various values of the outlet reflection coefficient and three combustion chamber lengths.

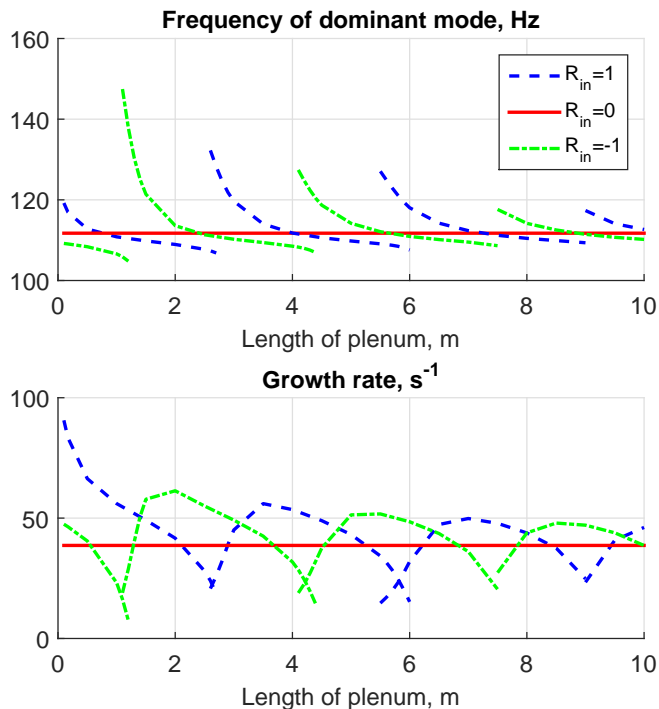


Figure 3.31: Dominant frequency of oscillations and its growth rate for various plenum lengths and three values of the inlet reflection coefficient; $R_{out} = 0$.

frequency of the setup is 112 Hz with a growth rate equal to 39 s^{-1} in the whole range of plenum lengths. This means that for both inlet and outlet anechoic conditions ($R_{in} = 0$ and $R_{out} = 0$) the setup is unstable.

For $R_{in} = 1$ in the range of plenum lengths $0.1 \div 2.6$ m the unstable frequency decreases from 119 Hz to 107 Hz; its growth rate decreases from 91 s^{-1} to 24 s^{-1} . At $L_{pl} = 2.7$ m the dominant frequency jumps to 128 Hz. Further increase of the plenum length up to 5.8 m results in the monotonic decrease of the dominant frequency; its growth rate first increases and then decreases. Next jumps occur for plenum lengths of 5.8 m and 9 m. The periodicity of frequency jump occurrence is $\Delta L_{pl} = 3.2$ m. This length corresponds to the acoustic wavelength at the frequency 112 Hz at the temperature of Section 1 equal to $T_{pl} = 300$ K.

Similar behaviour is observed for $R_{in} = -1$. In the range of plenum lengths $0.1 \div 1.1$ m the unstable frequency decreases from 109 Hz to 106 Hz; its growth rate decreases from 47 s^{-1} to 16 s^{-1} . At $L_{pl} = 1.1$ m the dominant frequency jumps to 147 Hz. Further increase of the plenum length to 4.2 m results in the monotonic decrease of the dominant frequency; its growth rate first increases and then decreases. Next frequency jumps occur at $L_{pl} = 4.3$ m and 7.5 m. A frequency jumps occurs each $\Delta L_{pl} = 3.2$ m as in the case of $R_{in} = 1$.

For certain values of the plenum length and the inlet reflection coefficient two ITA modes are unstable with close values of growth rate. In particular,

3. Application of the three-step approach to a laboratory, perfectly premixed, setup

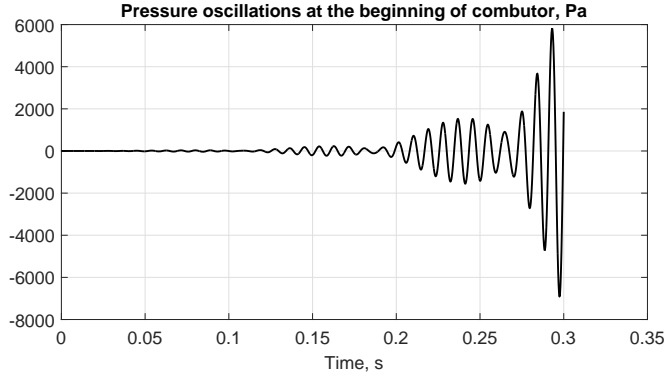


Figure 3.32: History of pressure oscillations at the beginning of the combustor; $R_{in} = 1$, $L_{pl} = 5.8$ m, $R_{out} = 0$.

such situation is well pronounced for the set of parameters $R_{in} = 1$, $L_{pl} = 5.8$ m, $R_{out} = 0$ (see Fig. 3.31). For this set of parameters, there are two unstable ITA modes, one at the frequency 108 Hz with the growth rate 25 s^{-1} and another at a frequency of 121 Hz with growth rate equal to 23 s^{-1} . These unstable frequencies coexist and lead to the unusual time history of acoustic perturbations in the time-domain simulations displayed in Fig. 3.32.

Sensitivity to the plenum cross-sectional area

Finally, a parametric analysis is performed for different values of the cross-sectional area of the plenum, in the range $S_{pl} = 1.056 \times 10^{-3} \div 10 \text{ m}^2$. The value $S_{pl} = 1.056 \times 10^{-3} \text{ m}^2$ corresponds to the cross-sectional area of the burner duct. Further increase of the plenum cross-sectional area beyond 10 m^2 does not show any change of the dominant frequency nor of its growth rate. Both the inlet and outlet reflection coefficients are set to zero. Results are presented in Fig. 3.33. The frequency of the dominant mode decreases from 138 Hz for $S_{pl} = 1.056 \times 10^{-3} \text{ m}^2$ to 110 Hz for $S_{pl} = 10 \text{ m}^2$. The growth rate of the dominant mode increases from -168 s^{-1} for $S_{pl} = 1.056 \times 10^{-3} \text{ m}^2$ to 51 s^{-1} for $S_{pl} = 10 \text{ m}^2$. In particular, the setup is unstable for values of the plenum cross-sectional area in the range $S_{pl} = 0.01 \div 10 \text{ m}^2$. Thus, it is possible to stabilise the unstable ITA mode reducing the cross-sectional area of the plenum.

Both dominant frequency and its growth rate in Fig. 3.33 are limited by the cases without plenum and inlet reflection coefficient $R_{in} = -1$ and $R_{in} = 0$. Dominant frequencies and their growth rates for the case without plenum and values of the inlet reflection coefficients $R_{in} = \{-1, 0, 1\}$ are presented in Tab. 3.8. Table 3.8 demonstrates why the ITA modes are stable in FTF calculation with URANS, whenever the plenum is not accounted for.

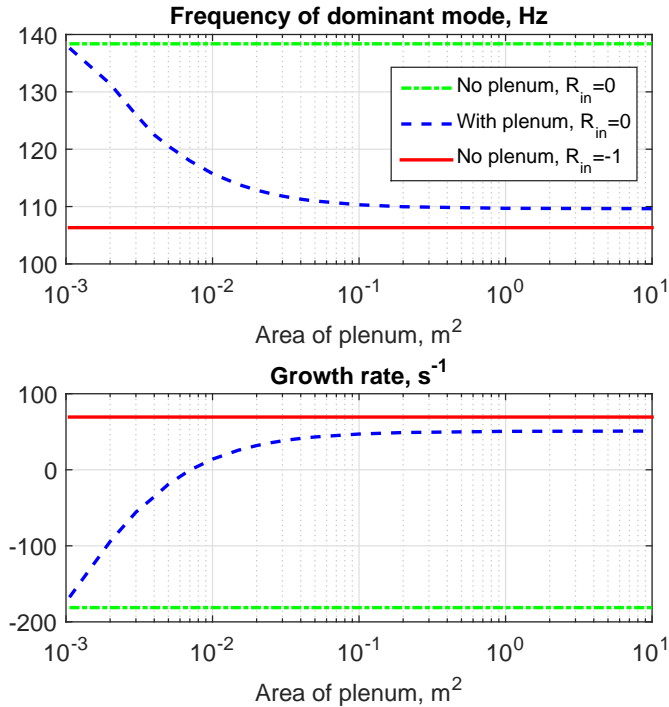


Figure 3.33: Dominant frequency of oscillations and its growth rate for various plenum lengths and three values of the inlet reflection coefficient; $R_{out} = 0$.

Table 3.8: Dominant frequencies and their growth rates for the case without plenum and various inlet reflection coefficient values.

	$R_{in} = -1$	$R_{in} = 0$	$R_{in} = 1$
Dominant frequency, Hz	106	138	183
growth rate, s ⁻¹	69	-181	-432

3.4.3 Results of the weakly nonlinear analysis

In this section, the acoustics of the system is assumed to be linear and the heat release perturbations depend on the amplitude of the acoustic perturbations. Such analysis is called weakly nonlinear.

As mentioned in the previous section, the FTF model 3.3 gives the very good approximation of the computed FTF (see Fig. 3.16). The drawback of this model is that it consists of 10 parameters and it is difficult to trace the dependence of each parameter on the amplitude of the excitation. Thus, for the nonlinear analysis FDF model 3.7 is employed.

The normalised amplitude of velocity perturbations A is needed for the calculation of the instantaneous values of parameters τ_i and σ_i . It is unknown before the simulation is run and is rather the output of the simulation. It is calculated as the maximum amplitude of the normalised velocity fluctuations between Sections 3 and 4 of the network model setup (this position corre-

sponds to the reference position in the CFD calculations) in the last 25 ms of simulations, as mentioned in section 3.3.3. Each time step the UIR to be used in Eq. 3.10 is recalculated based on the current amplitude of velocity perturbations A .

Validation of the forced response

It is worth to validate the nonlinear TLD flame model against CFD simulations before validating the three-step approach against the experimental data. For the validation of the linear TLD flame model, the CFD simulation is run for 45 ms with the broadband small-amplitude velocity excitation as in section 3.2.3. The resulting heat release is registered and then decomposed into its mean value \bar{Q}_{CFD} and fluctuating value Q'_{CFD} . The velocity time history at the reference position is also recorded and then the TLD flame model implemented in Simulink environment is applied to the velocity signal. As a result of simulation in Simulink, the respective heat release perturbations Q'_{SIM} are calculated. The Quality of Fit (QF) parameter proposed by Jaensch and Polifke [113] is used to estimate the agreement between the CFD and Simulink simulations:

$$QF = 100 \left(1 - \frac{\|Q'_{CFD} - Q'_{SIM}\|}{\|Q'_{CFD} - \bar{Q}_{CFD}\|} \right) \quad (3.14)$$

For the small-amplitude broadband velocity excitation the first 15 ms of the simulations are neglected as a transient period, thus only last 30 ms of the simulations are compared. Heat release fluctuations computed with the CFD simulation in OpenFOAM and calculated with Simulink modelling are presented in Fig. 3.34. The Quality of Fit calculated by Eq. 3.14 for the linear case is 98.81%.

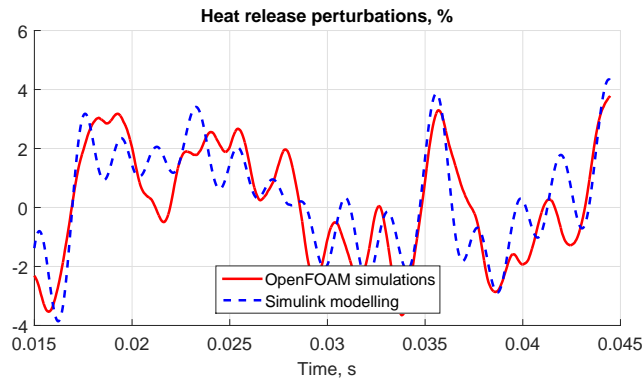


Figure 3.34: Validation of the linear response of the TLD flame model to small-amplitude velocity excitations.

Similar procedure of QF calculation is done for the mono-frequency excitation at high amplitudes. Since the flame response is deterministic both in

Table 3.9: Quality of Fit calculated by Eq. 3.14 of the heat release modelled with the nonlinear TLD flame model in Simulink with respect to the one computed with OpenFOAM simulations.

Excitation amplitude	100 Hz	160 Hz	240 Hz	320Hz
30%	93.88%	97.46%	97.73%	98.59%
50%	85.88%	93.78%	97.99%	98.30%
70%	82.84%	88.31%	94.93%	94.01%

CFD simulations and in Simulink modelling, the same time histories of velocity perturbations and heat release perturbations from CFD simulations used for the FDF calculation (see section 3.2.3) are used for the Quality of Fit computation. Then, the TLD flame model implemented in Simulink environment is applied to the velocity signal. The heat release perturbations Q'_{SIM} are computed and are shown in Figs. 3.35-3.38. The values of the Quality of Fit criterion are presented in Tab. 3.9.

Values of the QF lower than 90% correspond to low-frequency high-amplitude excitations (100 Hz 50%, 100 Hz 70%, and 160 Hz 70%) that are characterised by heat release oscillations of the amplitude close to 100%. When such high heat release oscillations take place, Simulink modelling predicts the positive and negative parts of the heat release response of the same amplitude. Meanwhile, under the same conditions in CFD simulations, the positive part of the heat release oscillation has higher amplitude and the negative part have lower amplitude (see Figs. 3.35, 3.36). This results in lowering of the QF value. For other cases QF criterion is higher than 90% that indicates good agreement between the TLD nonlinear flame model and the OpenFOAM CFD simulations.

Influence of the temperature downstream the flame

For each set of parameters, the simulation is run for 1.0 s, which is enough to reach either saturation to limit cycle pressure oscillations or zero pressure fluctuations. The setup is excited at the inlet first for $t_{exc} = 0.1$ s by a broadband signal in the range $0 \div 1$ kHz with maximum amplitude 5 Pa. In this way perturbations are introduced in the numerical model. After 0.1 s and until 1.0 s the system is left to evolve by itself without external excitations. The maximum amplitude of pressure oscillations is measured in the window $0.9 \div 1.0$ s and is presented hereafter.

Two values of temperature in Section 6 are studied: $T_{comb\ 2} = 1712$ K and $T_{comb\ 2} = 1930$ K. Corresponding simulations are performed and it is found that with a combustion chamber length $L_{c.c.} = 0.3$ m the setup is stable (see Figs. 3.39, 3.40) and with the combustion chamber length $L_{c.c.} = 0.7$ m the setup is unstable (see Figs. 3.41, 3.42), as in experiments [65].

It is shown in Figs. 3.40 and 3.42 how the instantaneous value of A parameter is computed from the time history of the normalised velocity perturbations. It is checked that simulations with the length of the time window for A calculation equal to 5 ms instead of 25 ms give the same results. In Figs. 3.41 and 3.42

3. Application of the three-step approach to a laboratory, perfectly premixed, setup

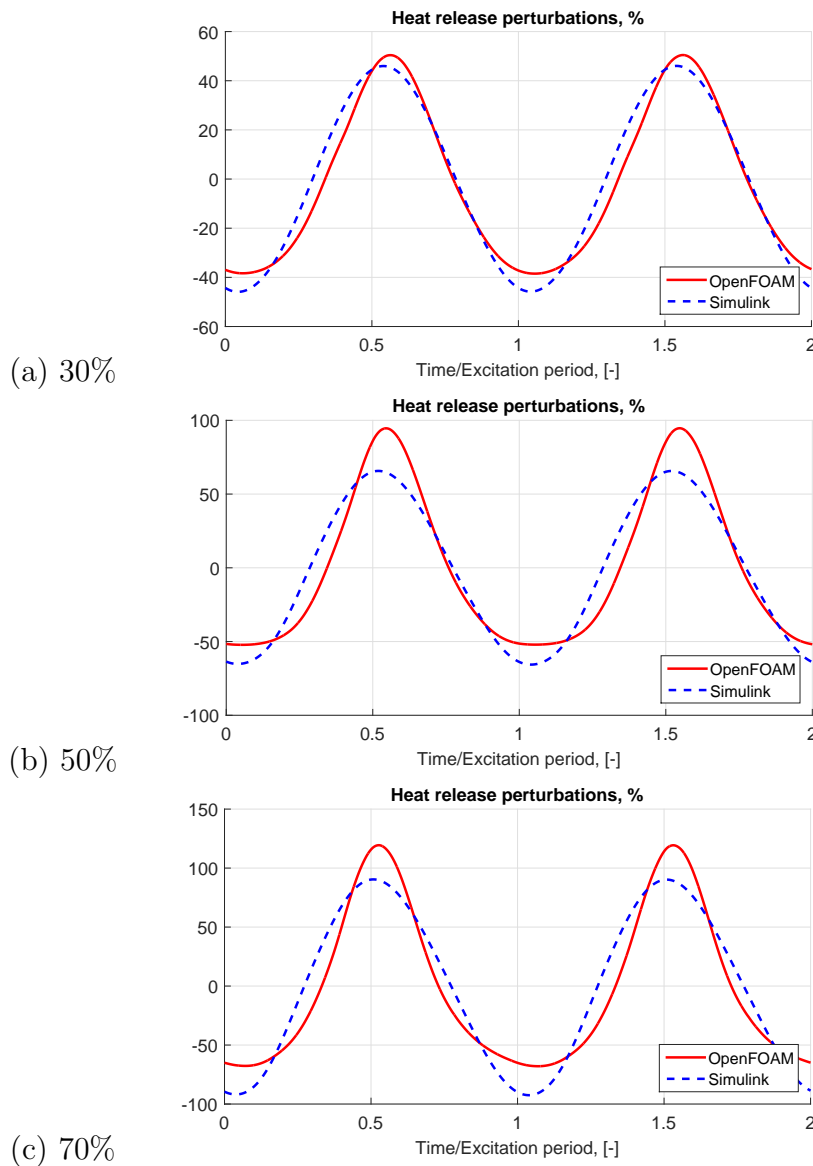


Figure 3.35: Validation of the nonlinear response of the TLD flame model to velocity excitations at 100 Hz; top to bottom excitation amplitudes 30%, 50%, and 70%.

it is possible to see how the nonlinear flame model works: first perturbations grow exponentially and then they saturate at a certain amplitude.

A parametric study with combustion chamber lengths in the range $0.3 \div 1.0$ m with steps of 0.1 m is thus performed. For values of the combustion chamber length lower and equal to 0.6 m the setup is stable for both temperature values in Section 6 (see Fig. 3.43). For values of the combustion chamber lengths equal and higher than 0.7 m the setup is unstable for both temperature values in Section 6. Larger temperature values after the flame are characterised by larger pressure oscillations amplitudes (see Fig. 3.43).

Results for velocity perturbations amplitude values above 70% are not

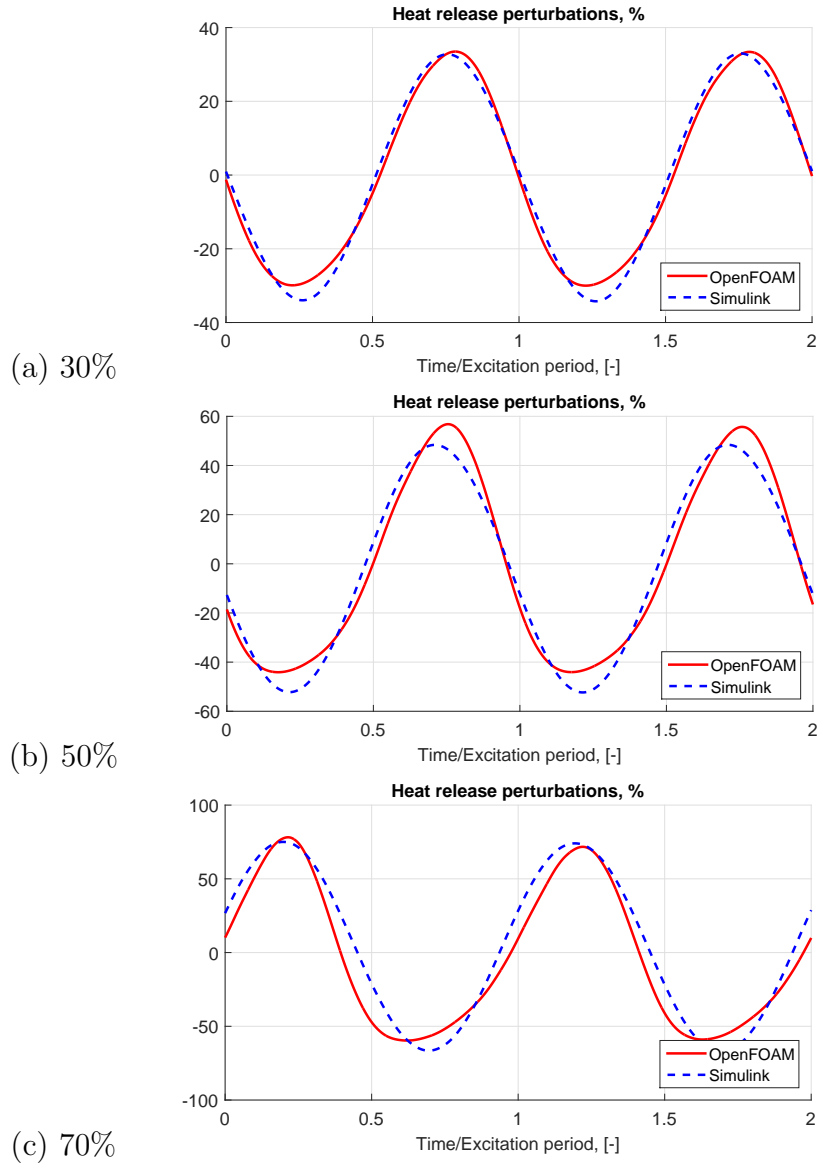


Figure 3.36: Validation of the nonlinear response of the TLD flame model to velocity excitations at 160 Hz; top to bottom excitation amplitudes 30%, 50%, and 70%.

shown in the current work since this is the maximum amplitude of the velocity perturbations during the simulations of the FDF (see Fig. 3.44). Thus, the presented results of network model simulations are consistent.

The unstable frequencies predicted by the network model simulations are shown in Fig. 3.45 as a function of the total length of the combustion chamber. The unstable frequencies are almost independent of the temperature after the flame T_{comb} .

3. Application of the three-step approach to a laboratory, perfectly premixed, setup

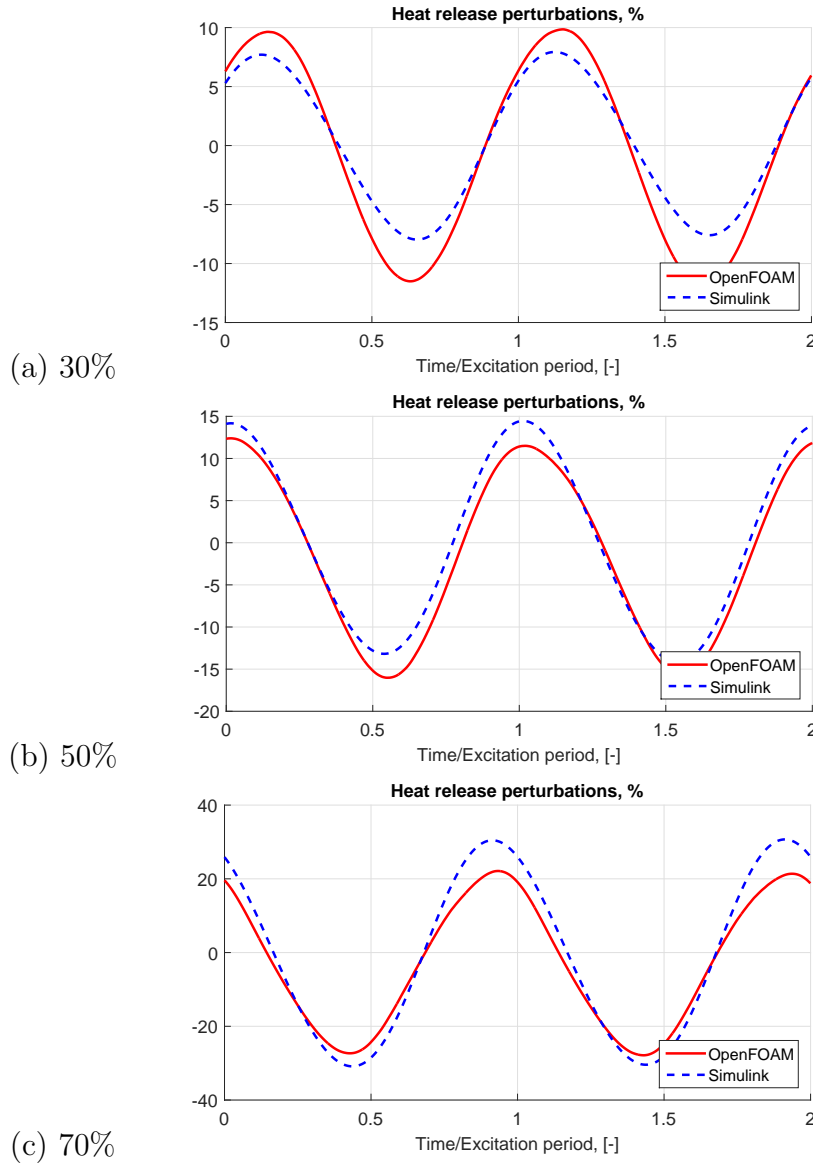


Figure 3.37: Validation of the nonlinear response of the TLD flame model to velocity excitations at 240 Hz; top to bottom excitation amplitudes 30%, 50%, and 70%.

Comparison with the FTF computed experimentally

Next, results of network model simulations with two FDFs - the one obtained experimentally and the one obtained with CFD simulations - are compared. Since the FDF was not measured experimentally and only the FTF is available from experiments, the model described by Eqs. 3.7, 3.8, 3.9 is assumed for the experimental FDF. For infinitesimal perturbations, the amplitude values of $\tau_{i,lin}$ and $\sigma_{i,lin}$ correspond to the experimental FTF by taking the parameters τ_i and σ_i from Tab. 3.3. Then, the change of parameters τ_i and σ_i with the amplitude is assumed to be the same as in the model of FDF computed from CFD by taking Θ_i and Σ_i values from Tab. 3.6. It can be seen from

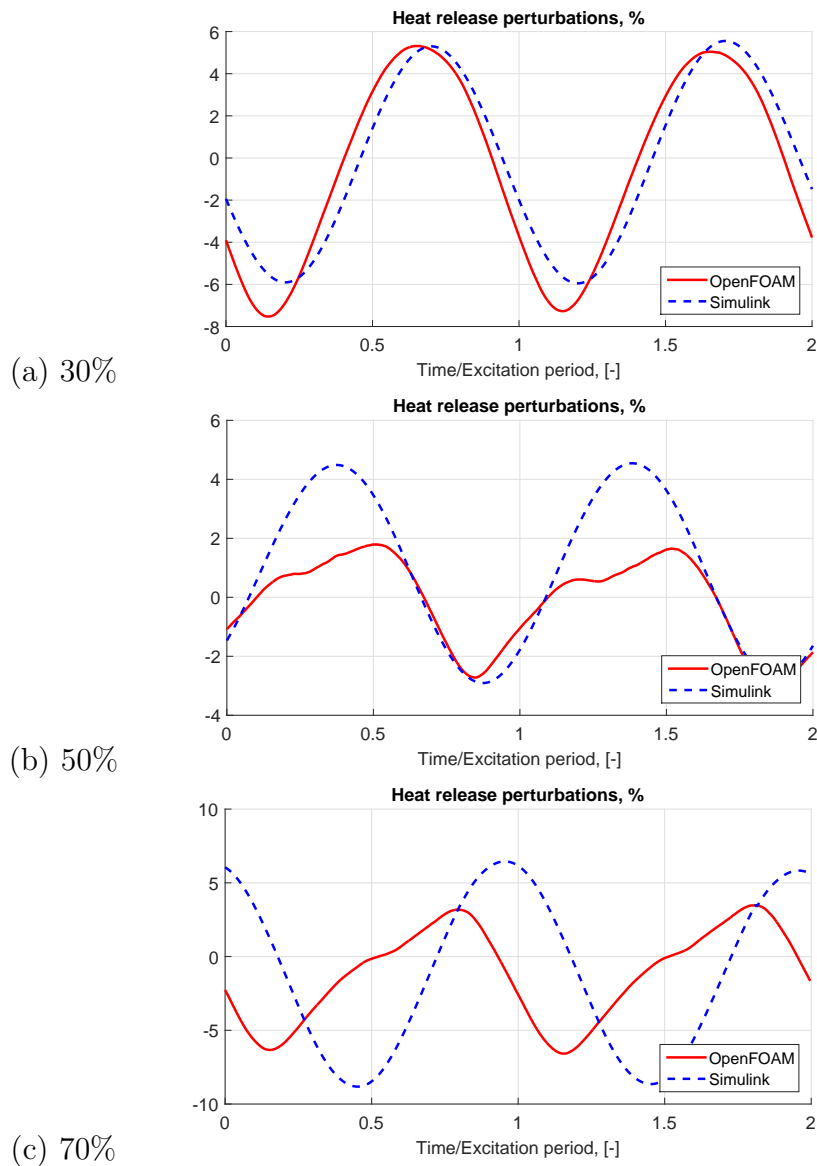


Figure 3.38: Validation of the nonlinear response of the TLD flame model to velocity excitations at 320 Hz; top to bottom excitation amplitudes 30%, 50%, and 70%.

Fig. 3.46, that the network model simulations predict larger amplitudes of pressure oscillations if the experimental FTF is used instead of the numerically calculated FTF. The dominant frequency of the pressure oscillations predicted by the network model simulations is closer to the experimental frequency when the experimental FTF is used, compared to the numerical FTF (see Fig. 3.47). The still existing difference in the frequency could be explained by uncertainties in the FTF measurements and by the step dependence of the ITA mode frequency on the phase of the FTF. With the length of combustion chamber $L_{c.c} = 1$ m and experimental FTF the amplitude of velocity perturbations at the reference point exceed 70% of its mean value, thus the results are not

3. Application of the three-step approach to a laboratory, perfectly premixed, setup

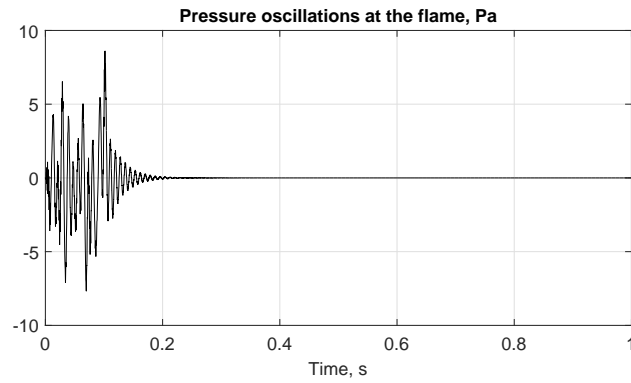


Figure 3.39: Pressure perturbations at the flame with $L_{c.c.} = 0.3$ m and $T_{comb\ 2} = 1930$ K.

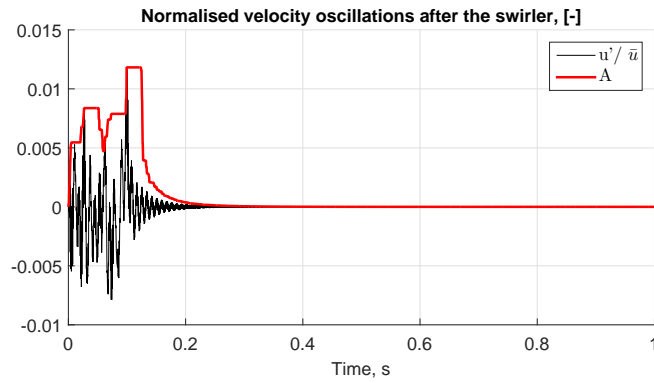


Figure 3.40: Normalised instantaneous velocity perturbations between Sections 3 and 4 of the network model setup and instantaneous A parameter with $L_{c.c.} = 0.3$ m and $T_{comb\ 2} = 1930$ K.

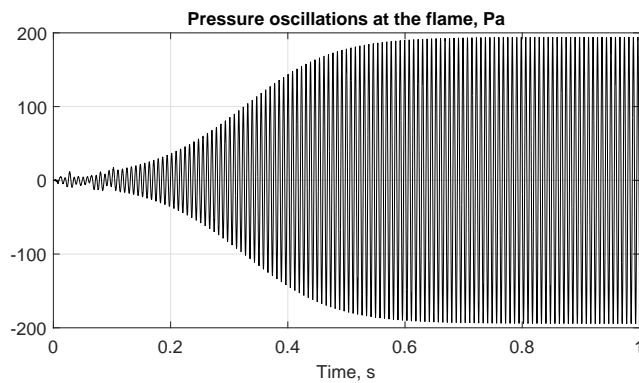


Figure 3.41: Pressure perturbations at the flame with $L_{c.c.} = 0.7$ m and $T_{comb\ 2} = 1930$ K.

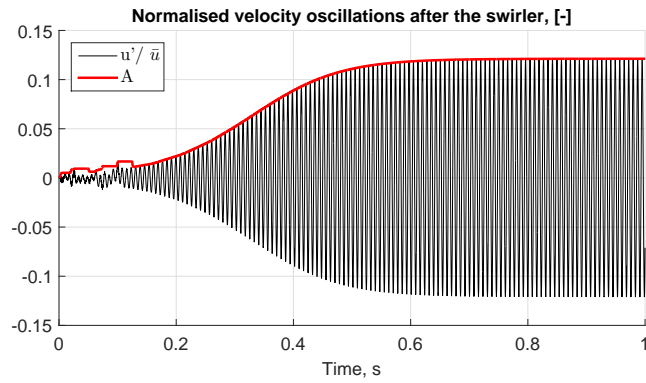


Figure 3.42: Normalised instantaneous velocity perturbations between Sections 3 and 4 of the network model setup and instantaneous A parameter with $L_{c.c.} = 0.7$ m and $T_{comb\ 2} = 1930$ K.

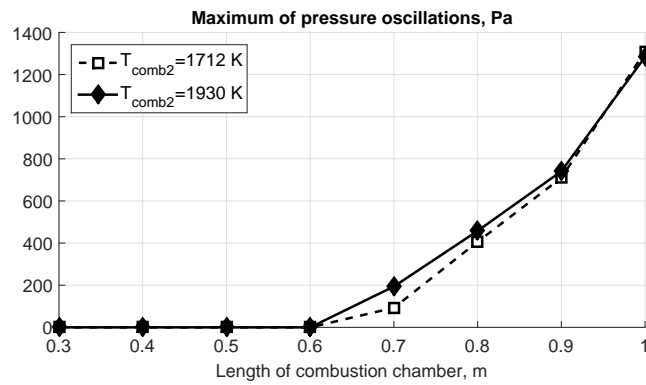


Figure 3.43: Amplitude of pressure perturbations at the flame for different $L_{c.c.}$ and $T_{comb\ 2}$.

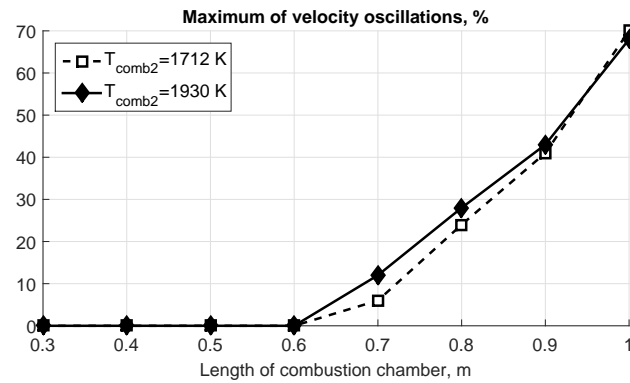


Figure 3.44: Normalised amplitude of velocity perturbations after the swirler for different $L_{c.c.}$ and $T_{comb\ 2}$.

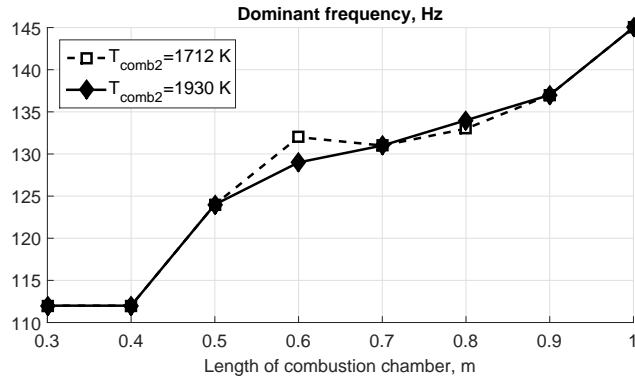


Figure 3.45: Dominant frequency of pressure perturbations at the flame for different $L_{c.c.}$ and $T_{comb 2}$.

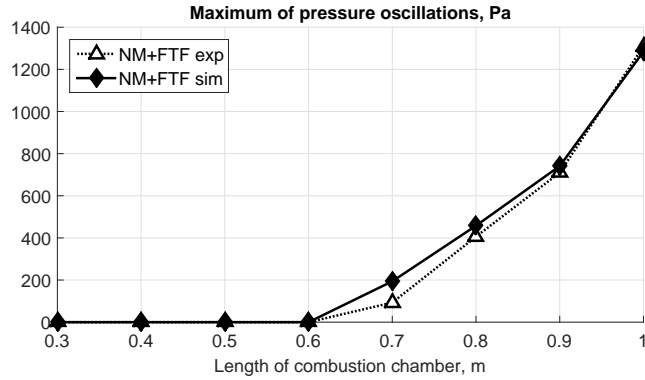


Figure 3.46: Amplitude of pressure perturbations at the flame in network model simulations with the FTF obtained experimentally and using the FTF obtained from numerical simulations with $T_{comb 2} = 1930$ K.

considered reliable (and are not presented).

Linear versus weakly nonlinear analysis

Finally, the linear analysis is performed with network model simulations in time domain with the FTF obtained numerically. In this set of simulations the FDF does not depend on the amplitude of the velocity perturbations before the flame, i.e. we have set the parameters $\Theta_i = 0$ and $\Sigma_i = 0$. In this set of calculations, there is no limit amplitude of pressure oscillations because they grow (or decay) exponentially. Only cases with values of $L_{c.c.} = 0.7 \div 1.0$ m that are unstable, as was already shown in Fig. 3.43, are considered. With $L_{c.c.} = 0.7$ m, when the non-linear simulation saturates at small-amplitude acoustic oscillations (see Figs. 3.43, 3.44), the linear and non-linear analyses predict the same frequency of oscillations (see Fig. 3.48). In the non-linear analysis, while increasing the parameter $L_{c.c.}$ the amplitudes of oscillations grow (see Figs. 3.43, 3.44), the phase of the FDF changes (see Fig. 3.11); this

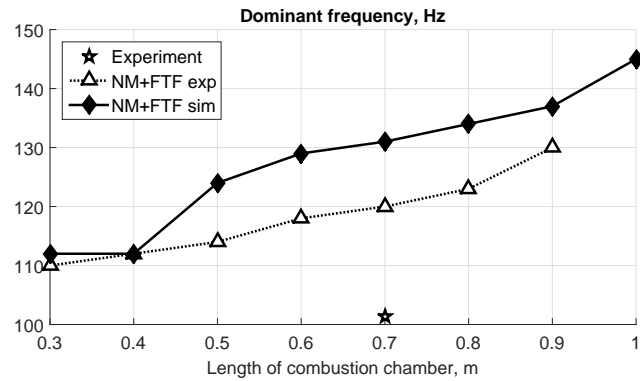


Figure 3.47: Dominant frequency of pressure perturbations at the flame obtained using the FTF obtained experimentally and using the FTF obtained from numerical simulations with $T_{comb, 2} = 1930$ K.

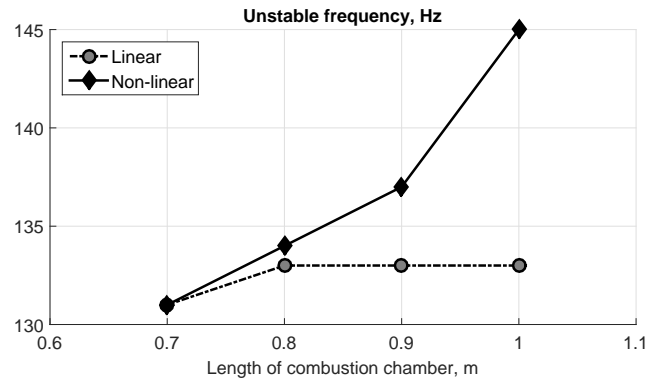


Figure 3.48: Unstable frequency of pressure perturbations at the flame obtained using the FTF and using the FDF obtained numerically with $T_{comb, 2} = 1930$ K.

results in the changing of the frequency of oscillations (see Fig. 3.48). However, in the linear analysis the phase of the FTF remains the same and the predicted unstable frequency depends very weakly on the stability parameter $L_{c.c.}$.

3.5 Discussion

In this chapter, the three-step approach has been applied to the BRS test rig and it is shown that the proposed approach can be used successfully for the stability analysis. The unstable frequency computed in the simulations corresponds to the unstable frequency observed in the experiments which is not a pure acoustic mode of the system but is an Intrinsic Thermo-Acoustic mode. For conditions when the test rig was unstable in experiments, the stability analysis described in this work also predicts the setup to be unstable. The discrepancy in the calculated frequency with the experimental data is explained by the heat losses not accounted for by the FSC model.

3. *Application of the three-step approach to a laboratory, perfectly premixed, setup*

The dependence of the frequency of the dominant mode and its growth rate on the outlet and inlet reflection coefficients, on the length of the combustion chamber, on the length of the plenum, and on the cross-sectional area of the plenum are studied. The strong dependence of the frequency of the ITA mode and its growth rate on these parameters is revealed. It is demonstrated that the usual technique to decrease the absolute value of the reflection coefficient could make the ITA mode even more unstable. The decrease of the plenum cross-section could be recommended as a method to suppress the unstable ITA mode.

The nonlinear dynamics of the setup is studied performing weakly nonlinear analysis: the acoustics is assumed to be linear and the heat release dependence on the velocity oscillations amplitude is taken into account. The dependence of the amplitude of pressure oscillations on the temperature downstream the flame is revealed. Simulations in the network model with two Flame Describing Function (FDF) models are conducted: the first FDF model is calculated with URANS simulations; the second FDF model is based on the FTF computed experimentally and the dependence of the model parameters on the amplitude are taken from the first FDF model. The unstable frequency calculated with the network model simulations and the FDF model 2 is closer to the experimentally observed frequency, compared to the case when the FDF model 1 is used. The still present difference in the frequency could be explained by uncertainties in the FTF measurements and by the strong dependence of the ITA mode frequency on the FTF. It is further shown that the frequency of the unstable ITA mode depends strongly on the amplitude of the acoustic perturbations.

Chapter 4

Application of the three-step approach to an industrial, technically premixed, setup

4.1 Description of the setup

In this section, an atmospheric single-burner test rig developed by Ansaldo Energia (AEN) and Centro Combustione Ambiente equipped with one full-scale AEN gas turbine burner is discussed. The test rig is characterised by two cylindrical volumes, the plenum and the combustion chamber, connected to each other by the burner. A schematic view of the experimental setup utilised for the thermo-acoustic experimental campaign is shown in Fig. 4.1. A thick layer of refractory material is interposed between the chamber walls and the external liner to make the test rig adiabatic. Previous calculations [13] showed that the setup is well insulated.

The air supply of the setup is not co-axial with the plenum (see Fig. 4.1), nevertheless the length of the plenum is sufficient to homogenise the flow field and avoid non-uniformities at the inlet of the burner. During the experimental session, it is possible to control air and fuel mass flow rate, as well as air temperature and length of the plenum and the chamber. The lengths of the

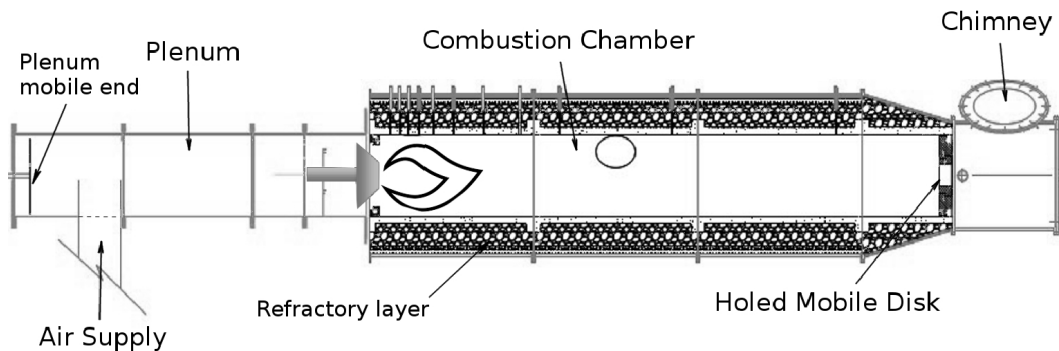


Figure 4.1: Scheme of the industrial test rig [11].



Figure 4.2: Multi-perforated outlet disk.

plenum and of the combustion chamber can be continuously varied in order to tune the frequency at which combustion instabilities occur. Additionally, it is possible to change the outlet geometry with different configurations, such as a single outlet or multi-perforated disk, as shown in Fig. 4.2, to obtain different acoustic downstream boundary conditions.

The flame is stabilised by the burner swirler, area expansion between the burner and the combustion chamber, and by the bluff-body in the burner. The burner consists of diagonal and axial passages and the centre cooled bluff-body (see Fig. 4.3). Swirler blades are installed both in the diagonal and axial passages of the burner. Injection of the fuel in the diagonal passage of the burner is organised through the holes in the blades. Fuel is injected in the axial passage just upstream of the swirler blades. At the exit of the burner, an air-cooled Cylindrical Burner Outlet (CBO) is located. CBO changes the heat release distribution and can be used to modify the burner FTF and, as a result, stability of the engine [114].

The test rig is equipped with several measurement systems able to collect data both for on-line monitoring and off-line data analysis. In the standard set-up, the following information is gathered:

- static pressure for oxidizer air and gas;
- emissions level (CO, NO_x, UHC) and O₂, CO₂ in the exhaust gases;
- the temperature of oxidizer air, exhaust gas and chamber shell;
- flame video;
- pressure loss Δp across the burner, particularly useful for the evaluation of the flame shape;

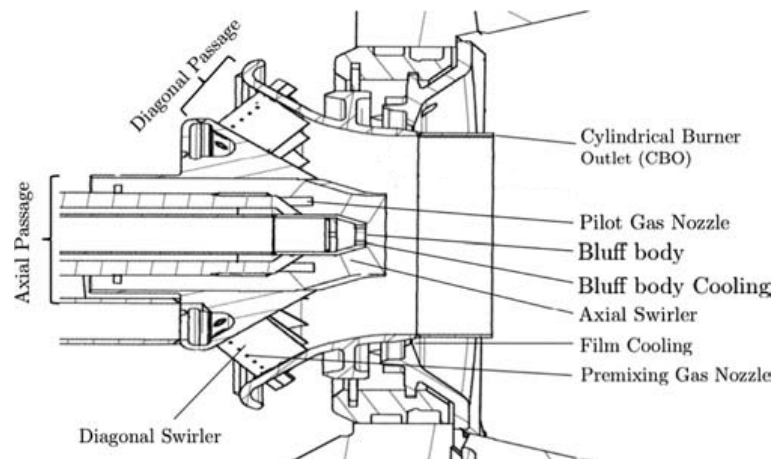


Figure 4.3: Schematic view of an industrial gas turbine test burner [12].

- 7 measurements of Δp along the combustion chamber to detect the pressure distribution.

Along one side of the cylindrical combustion chamber, a row of thermocouples and Δp transducers have been placed in order to provide the thermal and pressure profiles of the flame. These data are particularly important for the comparison of experimental results with the numerical simulations. Moreover, a dedicated hardware to measure acoustic pressure waves is present. A set of 3 microphones in the plenum and 7 pressure transducers in the combustion chamber are used. Thanks to these devices, the acoustic pressure field in these two volumes is reconstructed by using the Multi-Microphone-Method [115, 116]. Finally, an optical transducer equipped with an interferometric filter centred on the CH^* radical emission wavelength is installed to monitor chemiluminescence oscillations. This type of flame light emission is usually assumed to be directly proportional to heat release [115].

Experimental sessions have been carried out in order to acoustically characterise the full-scale industrial burner at scaled base load conditions in an atmospheric test-rig. In addition to the low sampling rate probes used to check the general behaviour of the plant and the burner, a high sampling rate system providing the operator FFT of pressure and optical transducers is continuously monitored to detect humming phenomena. The pressure transducers have the sampling rate of 10 kilo samples per second, and thus, measured FFTs have a bandwidth of 5 kHz. Self-excited combustion instabilities were observed during the experimental campaign. Figure 4.4 shows the FFT signal of two pressure transducers when humming is occurring. A peak is clearly standing above the noise at a well defined frequency, as well as its harmonics.

The pressure transducers are used in combination with the optical transducer in order to monitor both pressure and heat release oscillations. In the examined configuration, the optical transducer has shown a good ability in detecting heat release oscillations before pressure transducers detection of the pressure fluctuations. Consistently with this observation, during the exper-

4. Application of the three-step approach to an industrial, technically premixed, setup

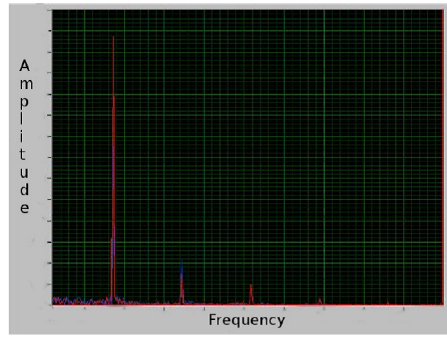


Figure 4.4: Typical FFT of two pressure transducers during a humming phenomenon.

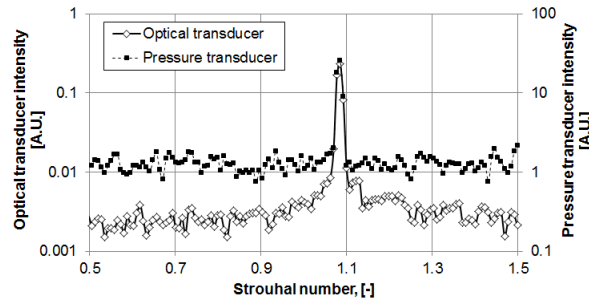


Figure 4.5: Optical transducer and pressure transducer signals, logarithmic scale, arbitrary units (A.U.). Left Y axis refers to the optical transducer signal while the right Y axis refers to the pressure transducer signal.

imental campaign, the onset of instabilities was observed first with optical transducer and later with pressure transducers. Figure 4.5 shows a comparison between the optical signal of the optical transducer and the first pressure probe of the combustion chamber in logarithmic scale (the left Y axis corresponds to the optical transducer and the right Y axis corresponds to the pressure transducer). Heat release and pressure oscillations are reported against the Strouhal number St , which is calculated taking the inner diameter of the combustion chamber and the average velocity at the exit of the burner as the reference length and velocity, respectively. In graphs and tables, frequencies are reported in terms of the Strouhal number.

$$St = \frac{fL_{ref}}{U_{ref}}, \quad (4.1)$$

where f is the frequency, L_{ref} is the reference length and U_{ref} is the reference velocity.

The difference between the two dependencies shown in Fig. 4.5 are explained as follows. The pressure transducers used for pressure oscillations measurement are cooled with air in order to reduce their temperature. However, the airflow passing around the pressure transducers induce noise affecting

the measured signal. This reduces the quality of the measurement of the outlet reflection coefficient calculated from the acoustic wave reconstruction. Moreover, this contributes to the detection of the combustion instability onset.

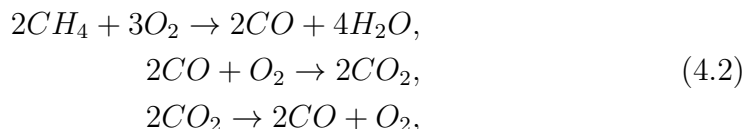
The results presented in this chapter are compared to the LES calculations performed by Rofi et al. [13]. The method used in that work is briefly outlined in section 4.2.

The thermoacoustic stability of this setup was also examined by Laera et al. [61, 11].

4.2 Overview of the reference LES study

4.2.1 Description of the LES software

In this work results of LES, particularly FTF, described in ref. [13] are used. The description of the LES is provided in this section. The reactive multi-species Navier-Stokes equations on unstructured grids are solved using the fully compressible explicit code AVBP [117] of CERFACS. The viscous stress tensor, the heat diffusion vector and the species molecular transport use gradient approaches. The fluid viscosity follows the Sutherland law and the species diffusion coefficients are obtained using a constant species Schmidt number and diffusion velocity corrections for mass conservation [118]. A high-order finite volume scheme is used for both time and space discretization. The turbulent stress term is modelled by the classical Smagorinsky model [73]. A chemical mechanism with six species (CH_4 , O_2 , CO_2 , CO , H_2O and N_2) and three reactions:



is used [119] to model methane/air combustion. A dynamic thickened flame model [120] is adopted to describe the interaction between the turbulence and the chemistry. Usage of low-Mach number or 'incompressible LES' [121] can give the advantage of reducing the calculation time. Compressible LES are performed in ref. [13] because in compressible LES fewer approximations are made, thus they are believed to yield more precise results [122].

4.2.2 Description of the numerical setup

The LES computational domain is formed by a fully unstructured mesh composed by 11852789 tetrahedral elements. The mesh is refined in correspondence of the flame and mixing regions; the time step is 4×10^{-8} s resulting in a Courant number equal to 0.7. In order to reduce the computational costs and to be able to use a finer mesh in the flame region, the LES domain is shorter than the real combustion chamber (about one-third of the real length).

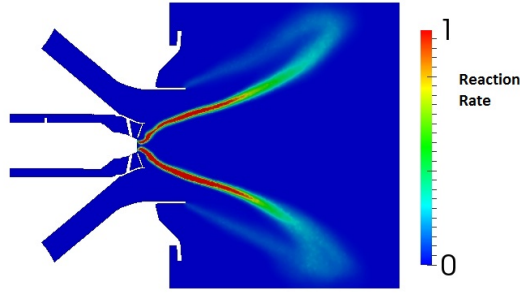


Figure 4.6: Normalised heat release; LES [13].

This assumption is considered acceptable since the recirculation zones are located well inside the LES domain; the flame is located in the first third of the LES domain; there is no diameter variation inside the test rig. Inlet and outlet boundary conditions are imposed using the non-reflecting Navier-Stokes Characteristic Boundary Condition (NSCBC) formulation to control acoustic reflection [107]. All the other walls are set as adiabatic and modelled using a logarithmic wall-law condition.

The field of heat release normalised by its maximum value in the longitudinal cross-section obtained from unperturbed simulations is shown in Fig. 4.6.

4.2.3 FTF numerical calculation

Once LES of the reactive process is statistically converged, a specific procedure to compute the FTF is performed. A multi-sinusoidal signal is imposed as velocity component normal to the burner inlet. This signal is applied both at the diagonal and the axial inlet to excite heat release oscillations. Velocity excitation normalised by the respective mean velocities are identical in both the diagonal and axial channels of the burner. When velocity perturbations pass through the blades of the diagonal and axial swirlers, tangential perturbations of velocity are produced. The frequencies imposed in the multi-sinusoidal signal are chosen in a wide range to allow the determination of the shape of the FTF with reasonable accuracy, focussing on the frequencies of interest of the industrial burner.

The velocity fluctuations are recorded by numerical probes. These probes are located both in the axial and in the diagonal passages, as shown in Fig. 4.7. Specifically, the velocity fluctuations recorded by these probes have been normalised against their own average values. The heat release fluctuations are computed as a global value calculating the volume integral of the heat release over the whole combustion chamber. The simulation is run for a time sufficient to guarantee at least six periods of oscillations at the lowest frequency of excitation. Frequencies are reported in terms of Strouhal number, which is calculated taking the inner diameter of the combustion chamber and the average velocity at the exit of the burner as reference length and velocity, respectively. The FTF is calculated for each frequency imposed in the multi-sinusoidal sig-

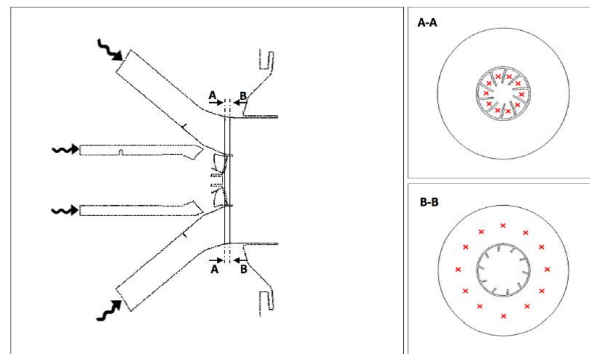


Figure 4.7: Schematic probes positions for the FTF calculation in the LES [13].

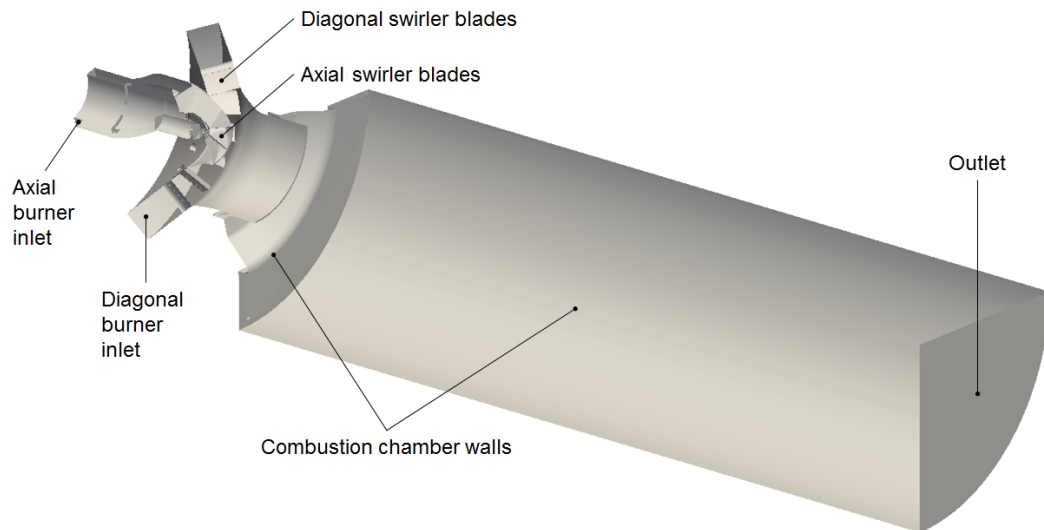


Figure 4.8: Scheme of the numerical setup.

nal; it is shown in Fig. 4.20 and discussed later.

4.3 URANS simulations

4.3.1 Numerical setup

The main goal of the CFD calculations in this work is to calculate the heat release response to acoustic excitations. The influence of the plenum on the flow field in the burner is neglected and the plenum is not considered. The length of the combustion chamber considered in the simulations is enough to enclose both the heat release zone and the inner recirculation zone in the computational domain as will be shown in the next section. Only one-quarter of the setup is simulated due to periodicity. The sketch of the computational setup is shown in Fig. 4.8.

A 3D mesh consisting mostly of hexahedral cells is created using the com-

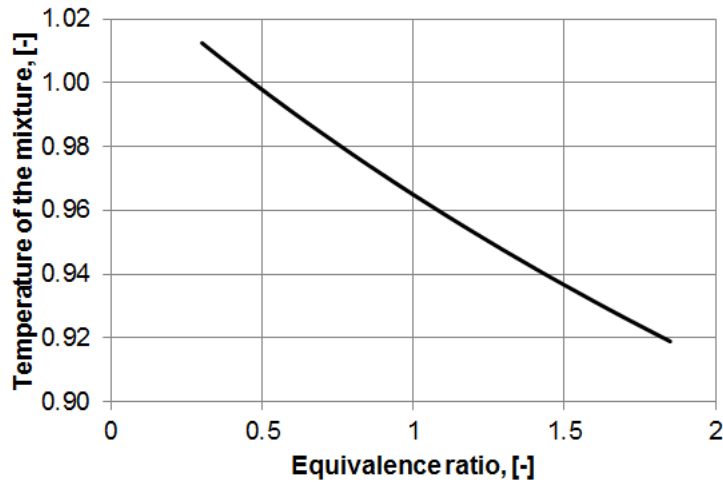


Figure 4.9: Dependence of the normalised local mixture temperature on the equivalence ratio.

mercial software ANSYS® ICEM CFD™. Tetrahedral cells are used in the zone of fuel injection in the axial part of the burner and at the exit of the axial part of the burner because of the high geometric complexity of these regions. The computational grid consists of 2588052 cells. The time step in the simulations is 2×10^{-7} s.

The walls of the numerical setup are heat insulated and, as it was shown by Rofi et al. [13], it is possible to assume the setup is adiabatic. Thus, issues connected to the uncounted heat losses in the FSC model observed in the previous chapter are not expected to occur in the industrial test rig simulations. The temperature is normalised with the temperature of the fuel-air mixture. The normalised air temperature at the air inlets is 1.04. The normalised fuel temperature at the fuel injections is 0.49.

Before running the simulations in OpenFOAM, the laminar flame speed has to be calculated. In general, the laminar flame speed depends on the equivalence ratio, temperature and pressure. The turbulent Prandtl number in the simulations is taken equal to 1. Thus, the local temperature of the mixture depends only on the local equivalence ratio (see Fig. 4.9). It is assumed that small pressure non-uniformity in the combustion chamber does not influence the laminar flame speed. Thus, the laminar flame speed depends only on the equivalence ratio.

The dependence of the laminar flame speed on the equivalence ratio is computed using the Cantera software [14]. The temperatures of the mixture for the laminar flame speed calculations are taken according to Fig. 4.9. The resulting dependence of the laminar flame speed on the equivalence ratio is shown in Fig. 4.10 normalised by the laminar flame speed at $\phi = 1.05$. The lower inflammability limit at the equivalence ratio (0.4) and the upper inflammability limit at the equivalence ratio (1.85) correspond to the flammability limits of the turbulent flames with for the considered operating temperature and pressure.

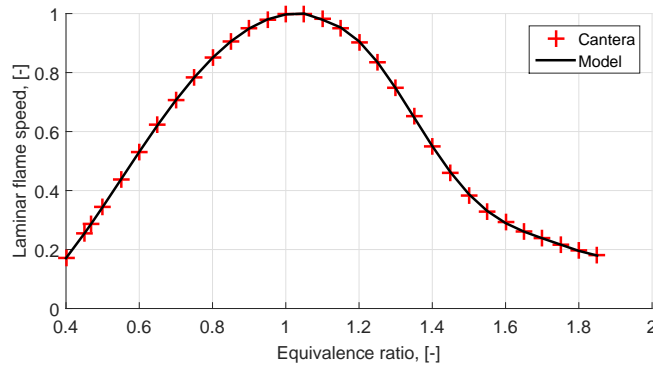


Figure 4.10: Dependence of the normalised laminar flame speed on the equivalence ratio calculated with Cantera [14] and modelled by Eq. 4.3.

The calculated laminar flame speed is approximated with the polynomial model

$$S_L = \sum_{j=0}^6 C_j (\phi - 1)^j, \quad (4.3)$$

where S_L is the laminar flame speed, C_j are the model coefficients that are different in two ranges of equivalence ratio $\phi = 0.4 \div 1.05$ and $\phi = 1.05 \div 1.85$. The coefficients C_j for both ranges of equivalence ratio are computed using the method of least squares. The laminar flame speed modelled by Eq. 4.3 is shown in Fig. 4.10.

4.3.2 Results of unperturbed simulations

The normalised value of the model parameter u_{FSC} used in Eq. 2.33 is taken equal to the averaged axial component of the velocity at the exit of the burner, $u_{FSC} = 1$. Fields of normalised axial velocity, of normalised temperature and of normalised heat release in the longitudinal cross-section obtained from unperturbed simulations are shown in Figs. 4.11, 4.12, and 4.13, respectively. The heat release is normalised by its maximum value. It is seen from Fig. 4.11 that the inner recirculation zone completely lies within the computational domain. The normalised adiabatic temperature of the flame for the mean equivalence ratio is 2.76. It is seen from Fig. 4.12 that the temperature of the flow in the outer recirculation zone is lower than the adiabatic temperature of the flame. It is explained by the fact that the laminar flame speed has zero values at the burner outlet plane close to the CBO, see Fig. 4.14. This, in turn, results in the presence of heat release mostly in the inner shear layer, see Fig. 4.13.

It is illustrative to compare the distributions of heat release in experiments and simulations along the longitudinal axis. To obtain this distribution from the simulations, several planes perpendicular to the longitudinal axis are considered from the beginning of the combustion chamber in the axial direction.

4. Application of the three-step approach to an industrial, technically premixed, setup

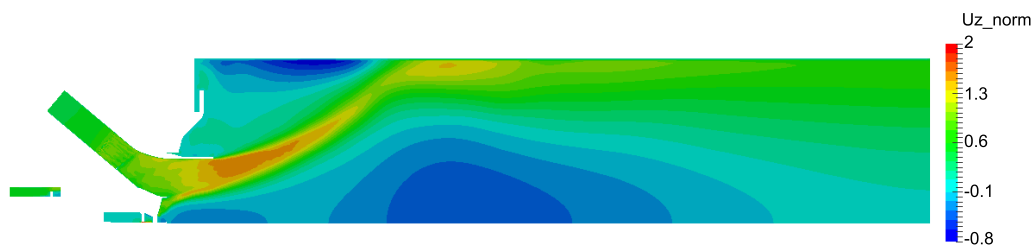


Figure 4.11: Normalised longitudinal component of velocity; URANS simulation.



Figure 4.12: Normalised temperature; URANS simulation.



Figure 4.13: Normalised heat release; URANS simulation.

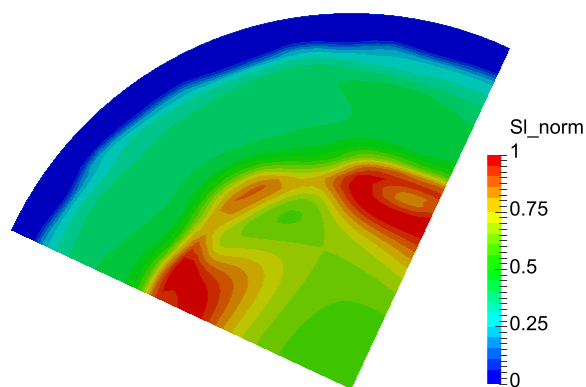


Figure 4.14: Normalised laminar flame speed distribution at the CBO outlet plane; URANS simulation.

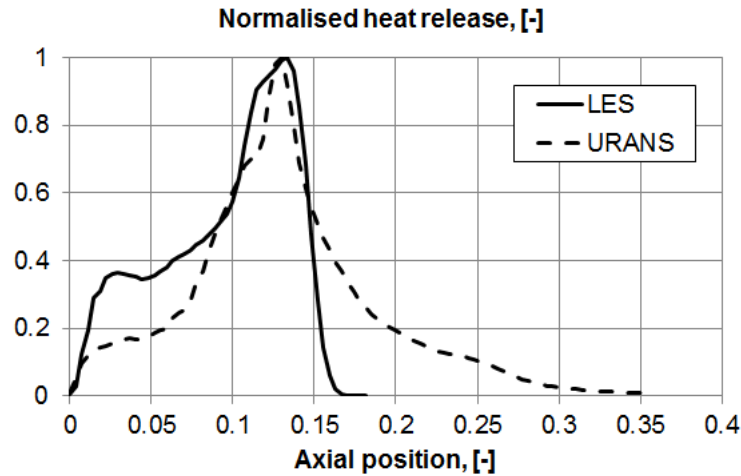


Figure 4.15: Heat release distributions from LES and URANS simulation.

Then, the heat release is integrated over these planes and the resulting values are plotted versus the longitudinal axis (see Fig. 4.15).

The peaks of the two heat release distributions presented in Fig. 4.15 coincide. Nevertheless, there are two main differences that could be explained by several factors. First, the flame is present mostly in the inner shear layer in the URANS simulation (see Fig. 4.13). However, in the LES the flame is observed in both inner and outer shear layers (see Fig. 4.6). Second, a turbulent Schmidt number of 0.3 suggested by authors of the FSC model [81, 94] may be low and lead to the high diffusion of the flame brush that could result in high dispersion of the heat release along the longitudinal axis (see Fig. 4.15).

Nevertheless, URANS simulations show good agreement both with experimental data and LES results in terms of pressure distribution close to the combustion chamber wall (see Fig. 4.16). Moreover, there is better agreement in the temperature distribution close to the combustor wall between experimental data and URANS results than between experimental data [61] and LES results [13]. Thus, it is decided to proceed with the current set of parameters to the FDF calculations.

4.3.3 FDF computations

FTF calculations

Once the URANS simulation of the combustion is statistically converged, simulations to compute the FTF is performed. A broadband signal is imposed as the air mass flow rate at the burner inlet. This signal is applied both at the diagonal and the axial inlet to excite heat release oscillations. Mass flow rate excitations normalised by the respective mean values are identical in both diagonal and axial channels of the burner. A Fast Fourier Transform of the excitation signal is shown in Fig. 4.17. The signal is constructed in the way that most of the excitation energy is concentrated in the low-frequency limit.

4. Application of the three-step approach to an industrial, technically premixed, setup

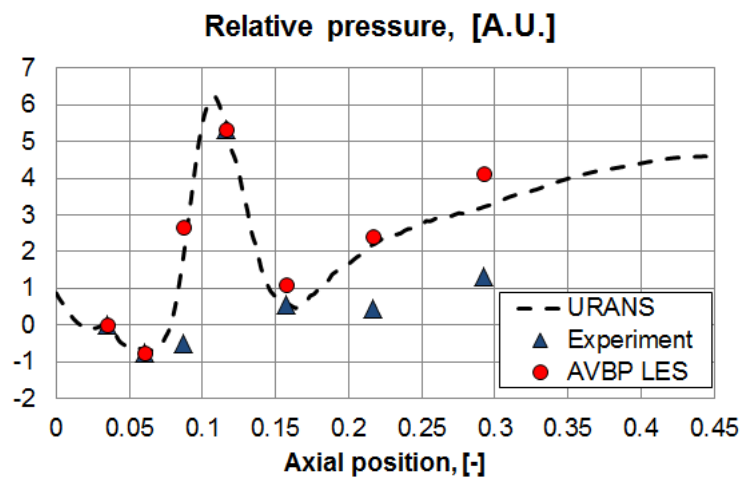


Figure 4.16: Relative pressure distributions from experiment, LES [13], and URANS simulation.

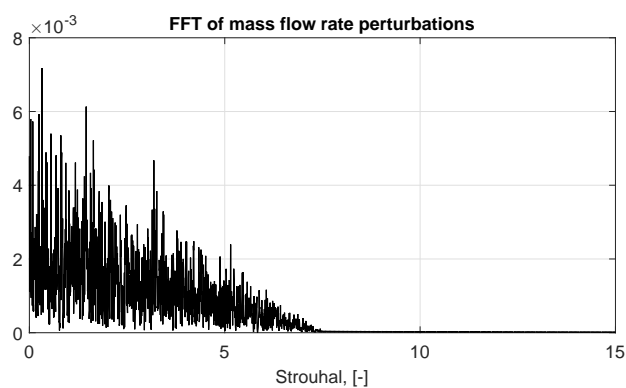


Figure 4.17: Fast Fourier Transform of the excitation signal applied in the FTF calculation with URANS.



Figure 4.18: Normalised root mean square deviation of heat release; URANS FTF calculation simulations.

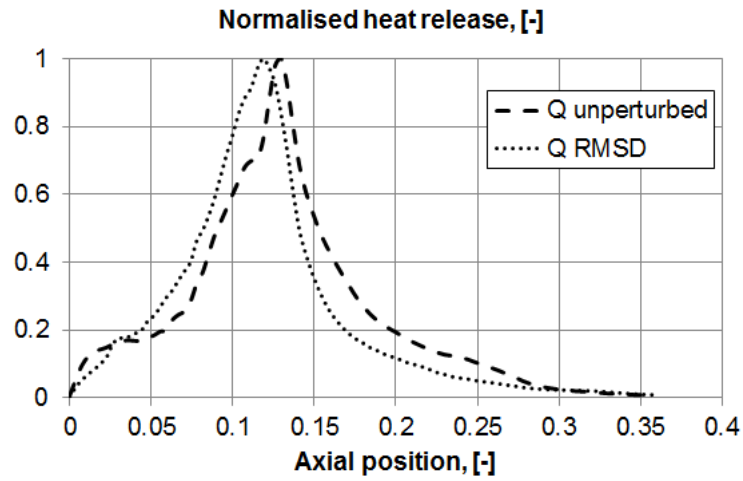


Figure 4.19: Normalised heat release from unperturbed simulation and its root mean square deviation from FTF calculation simulations; URANS simulations.

The root-mean-square deviation (RMSD) of the instantaneous heat release Q_j is calculated in the URANS simulations as:

$$Q_{RMSD} = \sqrt{\frac{1}{N} \sum_{j=1}^N (Q_j - \bar{Q})^2}, \quad (4.4)$$

where N is the number of time steps in the simulations, j denotes the current time step, \bar{Q} is the unperturbed heat release shown in Fig. 4.13. The heat release RMSD at the end of a simulation is shown in Fig. 4.18. The distribution of the unperturbed heat release and the heat release RMSD in simulations of the FTF calculation versus longitudinal axis are shown in Fig. 4.19. Distribution of Q_{RMSD} close to unperturbed value \bar{Q} indicates that the heat release response with the used excitation can be considered as linear.

The velocity time series u_r are recorded as the mass-averaged velocity at the outlet of the burner (plane A-A in Fig. 4.7). The response of the flame Q is measured in simulations as the volumetric integral of Eq. 2.44. After that, the mean values \bar{u}_r and \bar{Q} of measured u_r and Q are computed and are

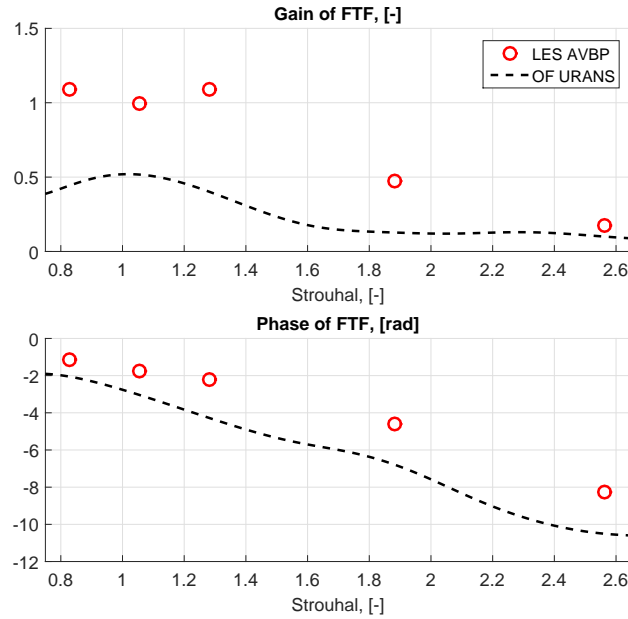


Figure 4.20: FTFs computed with LES in AVBP [13] and with URANS in OpenFOAM.

subtracted from series of u_r and Q , respectively, in order to obtain fluctuations of the axial velocity u'_r and of the heat release Q' . The simulation is run for 16.18 normalised time units. Time is normalised with respect to the mean flow velocity at the burner exit and the diameter of the combustion chamber. The duration of the UIR is assumed to be equal to 1.86 normalised time units. The first 2.91 normalised time units are considered as a transition period and are neglected. Using the Wiener-Hopf inversion method described in section 2.1.3, the Flame Transfer Function of the industrial test rig is calculated and is shown in Fig. 4.20 together with the FTF computed with LES [13]. Frequencies are reported in terms of the Strouhal number, which is calculated taking the inner diameter of the combustion chamber and the average velocity at the exit of the burner as reference length and velocity, respectively. Frequencies in a range of the Strouhal number $St = 0.75 \div 2.65$ are of particular interest, thus further analysis is concentrated on this frequency range.

The difference between the two FTFs calculated with LES and URANS shown in Fig. 4.20 are due to the differences between the corresponding heat release distribution (see Fig. 4.15). A more spatially distributed heat release in the URANS simulation with respect to the LES results in lower gain and larger phase of the FTF computed with URANS compared to those from LES. Reasons of the difference between the two FTFs will be explained in section 4.4.1.



Figure 4.21: Normalised root mean square deviation of heat release; URANS simulations 30% excitation at frequency $1.05 St$.

FDF computations

A set of simulations is run with excitation signal 30% of the mean value at three frequencies (in terms of the Strouhal number): 1.05, 1.88, and 2.56. These frequencies are chosen in a wide range of frequencies that permits to determine the shape of the FDF and focused on the frequencies of interest in this industrial burner. The simulations are run for a time to guarantee at least four periods of oscillations after the transition period of 2.65 normalised time units.

The RMSD of the heat release at the end of simulations with 30% excitation at the frequency $1.05 St$ is shown in Fig. 4.21. The high dispersion of the heat release RMSD means strong flame oscillations when it is excited at $1.05 St$ with 30% perturbation and indicates that this excitation can not be considered as linear. The distribution of the heat release RMSD in the FTF calculation simulations and with 30% excitation at $1.05 St$ versus longitudinal axis are shown in Fig. 4.22. The distribution of Q_{RMSD} with 30% excitation closer to the burner exit than Q_{RMSD} distribution with 10% excitation implies that heat release responds earlier to the excitation when excitation of higher amplitude is applied.

The FDF obtained from the simulations is shown in Fig. 4.23. For two frequencies, $1.05 St$ and $1.88 St$, both the FTF amplitude and the absolute value of the FTF phase decrease when increasing the excitation amplitude. For the frequency $2.56 St$ the FTF amplitude slightly increase when increasing the excitation amplitude. The absolute value of the FTF phase at $2.56 St$ with 30% excitation depends on the number of 2π jumps assumed at this frequency. One and two 2π jumps of the FTF phase at $2.56 St$ with 30% excitation are considered in this work. Physical meaning of the FTF change while increasing the excitation amplitude is discussed in the next section.

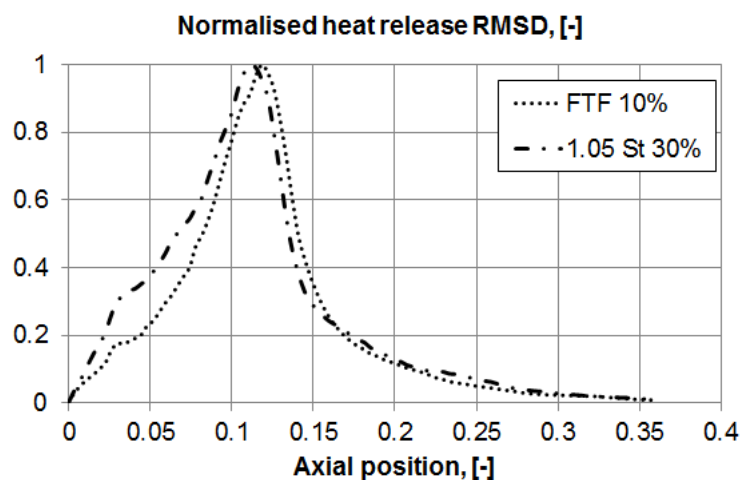


Figure 4.22: Normalised heat release root mean square deviation from FTF calculation simulations and simulations with 30% excitation at frequency $1.05 St$; URANS simulations.

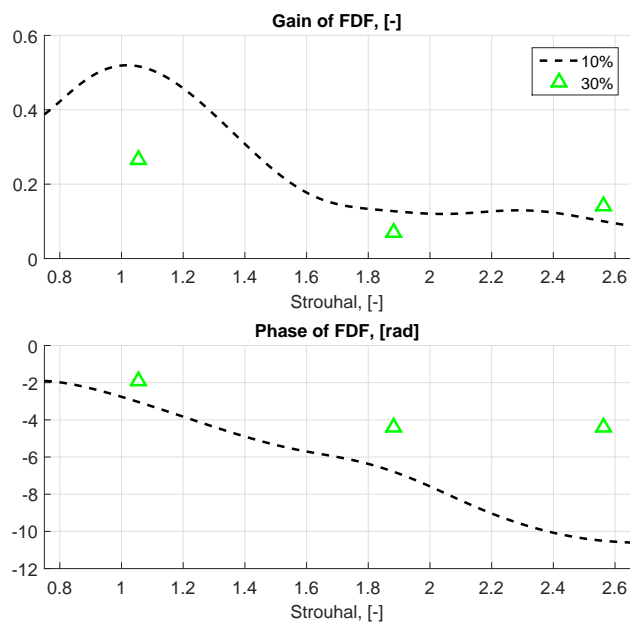


Figure 4.23: FDF computed with URANS in OpenFOAM.

Table 4.1: Values of normalised parameters τ_i and σ_i for model of FTF calculated with LES and URANS simulation.

Simulations	τ_1	σ_1	τ_2	σ_2
LES	0.37	0.18	0.69	0.11
URANS, 10%, models 1 and 2	0.71	0.24	0.86	0.17
URANS, 30%, model 1	0.37	0.12	0.41	0.14
URANS, 30%, model 2	0.51	0.17	0.68	0.21

4.4 Analytical time-lag distributed FDF models

4.4.1 FTF models

In the industrial burner discussed in this work, the pressure drop experienced by the gas passing through the burner is an order of magnitude larger than the pressure drop of the air. Moreover, the fuel is injected at the swirler blades (see Fig. 4.3). Thus, the usage of the FTF model (Eq. 2.81) and the UIR model (Eq. 2.82) is justified:

$$FTF_{tot}^{mod, simpl}(\omega) = e^{-i\omega\tau_1 - 0.5(\omega\sigma_1)^2} - e^{-i\omega\tau_2 - 0.5(\omega\sigma_2)^2}, \quad (4.5)$$

$$UIR_{tot}^{mod, simpl}(t) = \frac{1}{\sigma_1\sqrt{2\pi}}e^{-\frac{1}{2}\left(\frac{t-\tau_1}{\sigma_1}\right)^2} - \frac{1}{\sigma_2\sqrt{2\pi}}e^{-\frac{1}{2}\left(\frac{t-\tau_2}{\sigma_2}\right)^2}. \quad (4.6)$$

Optimum values of parameters τ_i and σ_i of the FTFs modelled with Eq. 4.5 are computed approximating the FTFs calculated with LES and with URANS using the method of least squares. Values of τ_i and σ_i normalised with respect to the mean flow velocity at the burner exit and the diameter of the combustion chamber are presented in Tab. 4.1. The LES FTF model is shown in Fig. 4.24. The models of UIRs for low amplitude excitation computed with LES and URANS are shown in Fig. 4.25.

Values of τ_1 and τ_2 in the URANS FTF model obtained with URANS simulations and 10% excitation are close to each other (see Tab. 4.1). This results in the lower maximum and minimum values of the URANS UIR with respect to the LES UIR (see Fig. 4.25). This, in turn, results in the lower amplitude of the URANS FTF with respect to the LES FTF (see Fig. 4.20). Higher values of τ_i in the URANS FTF model with respect to the LES FTF model results in the higher FTF phase of the URANS FTF than in the LES FTF.

4.4.2 FDF model 1

This model assumes that at the frequency $2.56 St$ with 30% excitation the phase of the FTF has only one jump of 2π , i.e. the FTF phase at $2.56 St$

4. Application of the three-step approach to an industrial, technically premixed, setup

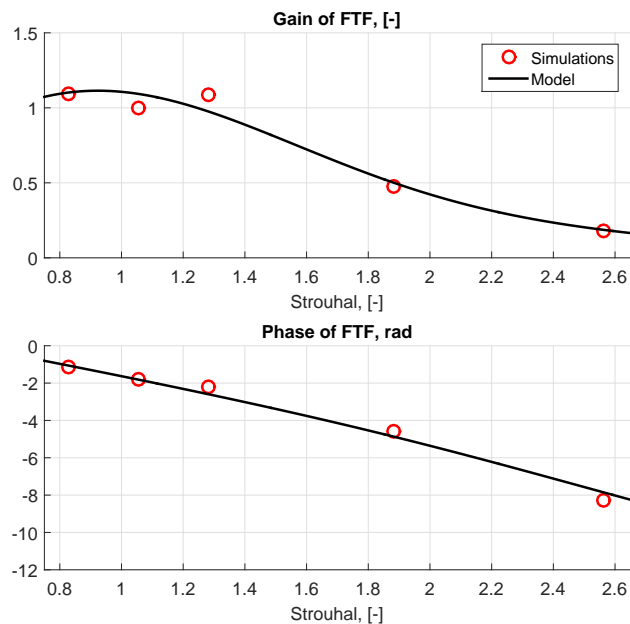


Figure 4.24: FTF computed with LES and modelled with Eq. 4.5.

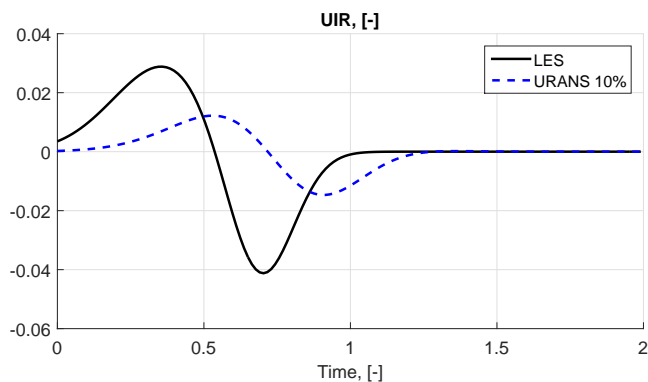


Figure 4.25: UIRs for low amplitude excitation modelled with Eq. 4.6.

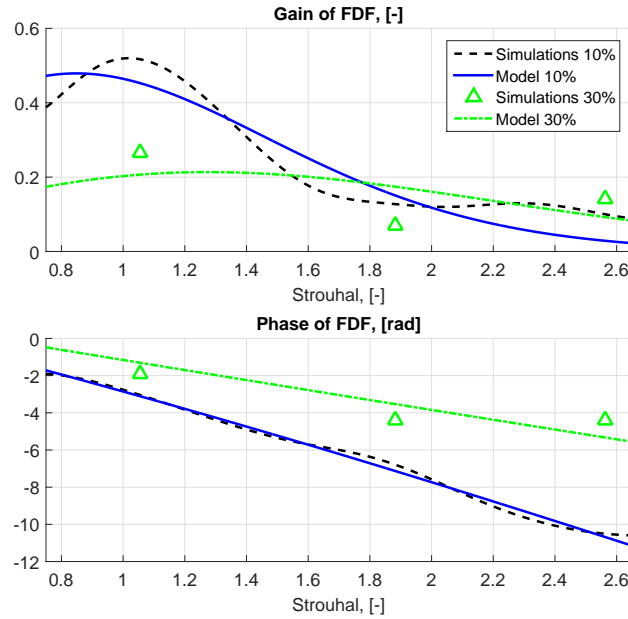


Figure 4.26: FDF computed with URANS in OpenFOAM and FDF model 1.

with 30% excitation is -4.39 rad. The FDF model 1 is shown in Fig. 4.26. The corresponding Unit Impulse Responses are shown in Fig. 4.27.

The calculated values of the parameters τ_i and σ_i for two amplitudes of perturbation are presented in Tab. 4.1 and shown in Fig. 4.28. Both τ_1 and τ_2 decrease when increasing the normalised amplitude of velocity perturbations upstream the flame A . This trend implies that the flame is shifted towards the burner when it is forced by excitation with high amplitudes. The decrease of σ_1 while increasing A is explained by the limit $\sigma_1 \leq \tau_1/3$. The decrease of σ_2 with instantaneous decrease of τ_2 implies that the length of the UIR becomes shorter while increasing A (see Fig. 4.27) that does not agree with the heat release RMSD at different amplitudes of excitation shown in Fig. 4.22. The

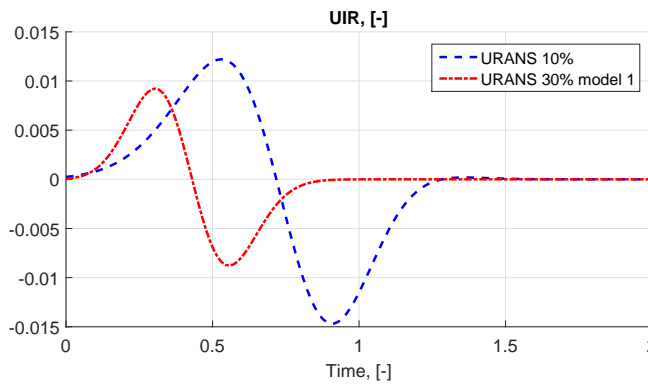


Figure 4.27: UIRs modelled with Eq. 4.6 for low amplitude excitation.

4. Application of the three-step approach to an industrial, technically premixed, setup

Table 4.2: Values of normalised parameters $\tau_{i,lin}$, Θ_i , $\sigma_{i,lin}$ and Σ_i for FDF models.

FDF model	$\tau_{1,lin}$	Θ_1	$\sigma_{1,lin}$	Σ_1	$\tau_{2,lin}$	Θ_2	$\sigma_{2,lin}$	Σ_2
1	0.88	-1.93	0.29	-1.92	1.08	-2.05	0.18	-0.77
2	0.81	-1.24	0.27	-1.23	0.94	-0.92	0.14	1.51
3	0.37	-1.93	0.18	-1.92	0.69	-2.05	0.11	-0.77
4	0.37	-1.24	0.18	-1.23	0.69	-0.92	0.11	1.51
5	0.37	-0.42	0.18	0.37	0.69	-0.42	0.11	0.37

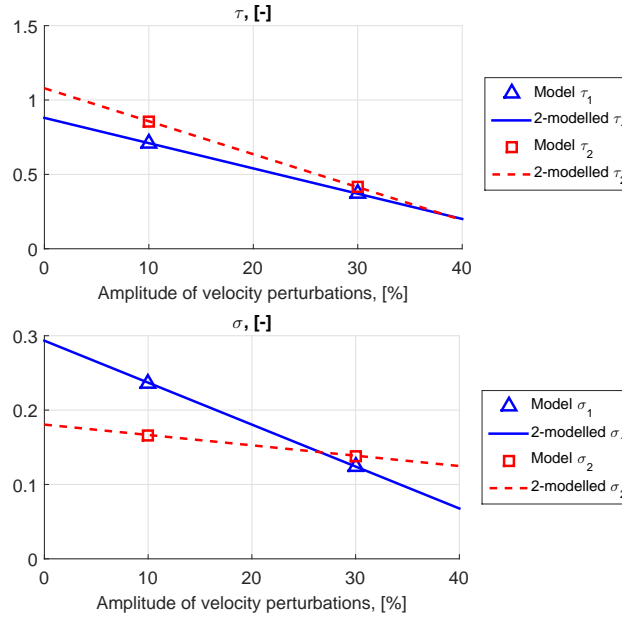


Figure 4.28: Dependencies $\tau_i(A)$ and $\sigma_i(A)$ in FDF model 1.

dependencies of τ_i and σ_i on A are modelled as

$$\tau_i(A) = \tau_{i,lin}(1 + \Theta_i A), \quad (4.7)$$

$$\sigma_i(A) = \sigma_{i,lin}(1 + \Sigma_i A). \quad (4.8)$$

The linear dependencies of τ_i and σ_i on A are chosen because only 2 amplitudes of excitations are computed. The values of the parameters in Eqs. 4.7 and 4.8 are presented in Tab. 4.2. The functions in Eqs. 4.7 and 4.8 for the FDF model 1 are shown in Fig. 4.28. This FDF model has sharp dependencies of its parameters on the excitation amplitude.

4.4.3 FDF model 2

This model assumes that at frequency $2.56 St$ with 30% excitation the phase of the FTF has two jumps of 2π , i.e. the FTF phase at $2.56 St$ with 30%

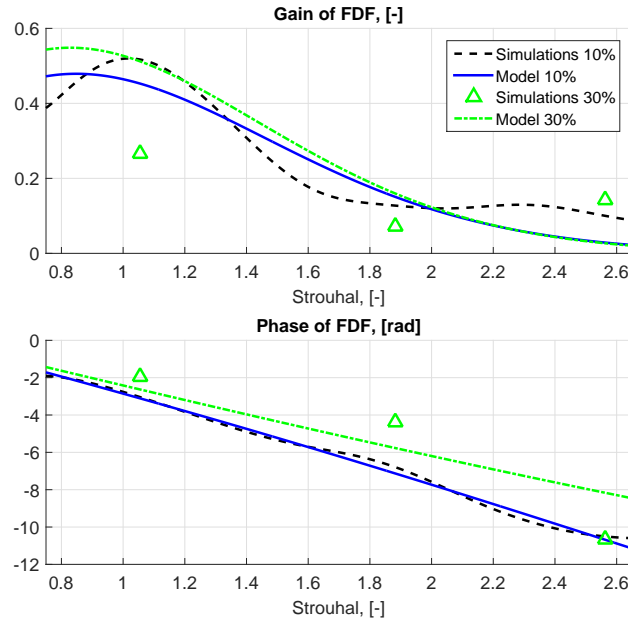


Figure 4.29: FDF computed with URANS in OpenFOAM and FDF model 2.

excitation is -10.68 rad. This model has larger norm of residuals with respect to the FDF model 1; however, the FDF model 2 has more physical sense as is shown further. The FDF model 2 is shown in Fig. 4.29. The corresponding Unit Impulse Responses are shown in Fig. 4.30.

The calculated values of the parameters τ_i and σ_i for two amplitudes of perturbation are presented in Tab. 4.1 and shown in Fig. 4.31. Both τ_1 and τ_2 decrease when increasing A . This trend implies that the flame is shifted towards the burner when it is forced by excitation with high amplitudes. The decrease of σ_1 while increasing A is explained by the limit $\sigma_1 \leq \tau_1/3$. The increase of σ_2 with the instantaneous decrease of τ_2 implies that the length of the UIR remains the same while increasing A (see Fig. 4.30) that agrees

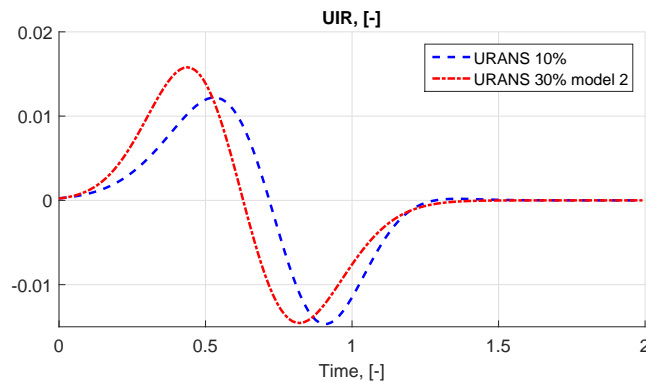


Figure 4.30: UIRs modelled with Eq. 4.6.

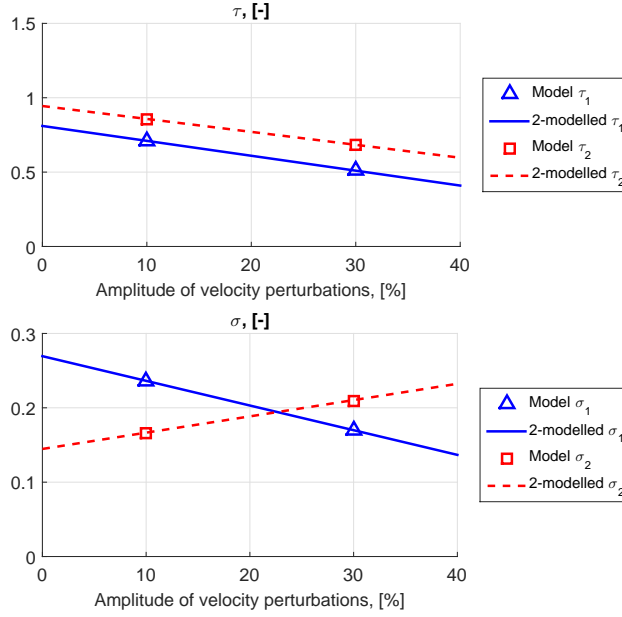


Figure 4.31: Dependencies $\tau_i(A)$ and $\sigma_i(A)$ in FDF model 2.

with the heat release RMSD at different amplitudes of excitation shown in Fig. 4.22. The dependencies of τ_i and σ_i on the normalised amplitude of velocity perturbations A are modelled by Eqs. 4.7 and 4.8. The calculated values of the parameters in Eqs. 4.7 and 4.8 are presented in Tab. 4.2. The functions in Eqs. 4.7 and 4.8 for the FDF model 2 are shown in Fig. 4.31. This FDF model displays less sharp dependencies of its parameters on the excitation amplitude than FDF model 1.

4.4.4 FDF model 3

In the next FDF model, the dependencies of τ_i and σ_i on the normalised amplitude of the velocity perturbations A are modelled as

$$\tau_i(A) = \tau_{i,lin}(1 + \Theta_i A - \Theta_i A_{LES}), \quad (4.9)$$

$$\sigma_i(A) = \sigma_{i,lin}(1 + \Sigma_i A - \Sigma_i A_{LES}), \quad (4.10)$$

where $\tau_{i,lin}$ and $\sigma_{i,lin}$ are the parameters of the LES FTF model, A_{LES} is the amplitude of the velocity excitation in the LES, the parameters Θ_i and Σ_i are taken from the FDF model 1. Thus, FDF model 3 is composed of the FTF calculated with LES [13] and the FDF model 1 computed with URANS. The terms $\Theta_i A_{LES}$ and $\Sigma_i A_{LES}$ are added in Eqs. 4.9 and 4.10 with respect to Eqs. 4.7 and 4.8 in order to guarantee that for $A = A_{LES}$ the values of τ_i and σ_i are equal to the values of the LES FTF model presented in Tab. 4.1. The parameters $\tau_{i,lin}$, Θ_i , $\sigma_{i,lin}$, and Σ_i of the FDF model 3 are presented

in Tab. 4.2. This FDF model acts as the FTF computed with LES for low amplitudes of velocity perturbations and has the strong dependence of the model parameters on A as in the FDF model 1.

4.4.5 FDF model 4

This FDF model is blended from the FTF calculated with LES [13] and the FDF model 2 computed with URANS. The blending is accomplished by assuming that the dependencies $\tau_i(A)$ and $\sigma_i(A)$ are modelled by Eqs. 4.9 and 4.10, where $\tau_{i,lin}$ and $\sigma_{i,lin}$ are taken from the LES FTF, Θ_i and Σ_i are taken from the FDF model 2. The parameters $\tau_{i,lin}$, Θ_i , $\sigma_{i,lin}$, and Σ_i of the FDF model 4 are presented in Tab. 4.2. This FDF model acts as the FTF computed with LES for low amplitudes of velocity perturbations and has the dependence of the model parameters on A as in the FDF model 2. The FDF model 4 has less strong dependence on the amplitude with respect to the FDF model 3.

4.4.6 FDF model 5

The next FDF model blends the FTF computed with LES for the industrial setup and the FDF model of the laboratory test rig presented in section 3.3.3. This is done by assuming that the dependencies $\tau_i(A)$ and $\sigma_i(A)$ are modelled by Eqs. 3.8 and 3.9

$$\tau_i(A) = \tau_{i,lin}(1 + \Theta_i A^2), \quad (4.11)$$

$$\sigma_i(A) = \sigma_{i,lin}(1 + \Sigma_i A), \quad (4.12)$$

where $\tau_{i,lin}$ and $\sigma_{i,lin}$ are taken from the LES FTF, Θ_i and Σ_i are taken from the FDF model of the laboratory setup (see section 3.3.3). The parameters $\tau_{i,lin}$, Θ_i , $\sigma_{i,lin}$, and Σ_i of the FDF model 5 are presented in Tab. 4.2.

It is observed in the laboratory setup that while increasing the amplitude of the velocity excitation, the peak of the heat release distribution along the longitudinal axis is shifted towards the burner and the heat release distribution along the longitudinal axis becomes wider, i.e. the flame length is augmented. This means that when the amplitude of velocity perturbations upstream of the flame increases, parameters τ_i are decreasing and parameters σ_i are increasing.

The square decay of the τ_i and the linear increase of the σ_i give smaller norms of residuals in section 3.3.3 and are used in this FDF model as well. When the amplitude of velocity perturbations approaches 0, values of τ_i and σ_i modelled by Eqs. 4.11 and 4.12 approach values of the LES FTF model, i.e. the FDF becomes the FTF computed with LES.

Table 4.3: Values of parameters imposed in the network model of the industrial test rig.

N	Section	Area, [-]	Length, [-]	Temperature, [-]
1	Plenum	1	0.78	1.04
2	Burner duct 1	0.15	0.015	1.04
3	Burner duct 2	0.15	0.024	1
4	Burner duct 3	0.15	0.030	1
5	Combustor 1	1	$x_{fl} = 0.1$	1
6	Combustor 2	1	$L_{c.c.} - x_{fl}$	2.76

4.5 Network model simulations

4.5.1 Numerical setup

The network model numerical setup consists of 6 regions connected by 3 jump conditions with pressure losses, one jump condition at the flame and 2 boundary conditions, as shown in Fig. 4.32. The values of the cross-sectional area normalised against the cross-sectional area of the combustion chamber, the lengths of the sections normalised against the reference length and the temperature normalised against the mean temperature of the mixture at the burner exit for each section are listed in Tab. 4.3. The jump matrices to connect acoustic waves between adjacent sections are calculated using Eqs. 2.100 and 2.113. The reflection coefficient of the inlet is taken $R_{in} = 1$. The outlet reflection coefficient $R_{out,1}$ is measured experimentally using a multi-microphone technique. Several values of the outlet reflection coefficient around the measured one are tested in this work because of some uncertainties in this value, particularly caused by microphones' cooling. The normalised total length of the combustor (sum of the lengths of Section 5 and Section 6) is varied in the range $L_{c.c.} = 0.74 \div 1.59$ with a step $\Delta L_{c.c.} = 0.037$. Acoustic losses at the area changes between the plenum and the burner and between the burner and the combustor are taken into account by the pressure loss coefficients $\zeta_{decr} = 0.442$ and $\zeta_{incr} = 0.718$, respectively, calculated by the formulae 2.93 and 2.104. The pressure loss coefficient at the swirler is calculated from the measurements. The active flame, i.e. the unsteady heat release, in the low-order network model is positioned at $x_{fl} = 0.1$. The sum of the lengths of Sections 4 and 5 is equal to the maximum of the heat release in the longitudinal direction in LES and URANS simulations (see Fig. 4.15) because the flame anchor position corresponds to the beginning of Section 4 in the network model. The temperature gradient coincides with the position of the active flame and is situated between Sections 5 and 6. The time step in the network model simulations is equal to $1.33 \cdot 10^{-3}$ normalised time units that is smaller than any acoustic time lag in any Section of the network model.

The probe of velocity fluctuations for the unsteady heat release model is situated between Sections 3 and 4 that corresponds to the velocity probe position in both URANS and LES. The instantaneous unsteady heat release

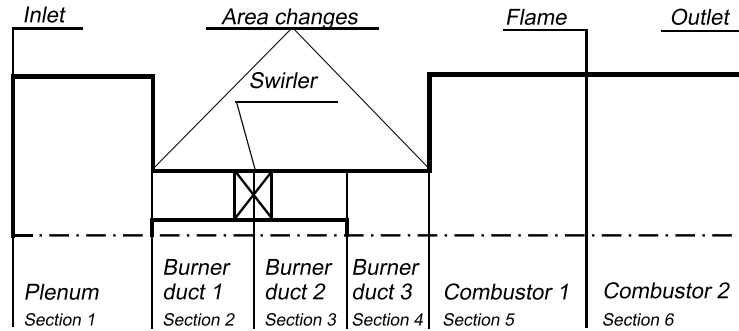


Figure 4.32: Scheme of the network model numerical setup of the industrial test rig.

is calculated as the convolution of the history of velocity fluctuations and the Unit Impulse Response

$$Q'(t) = \frac{\bar{Q}}{\bar{u}} \int_0^\infty UIR_{tot}^{mod, simpl}(t' - t)u'(t)dt'. \quad (4.13)$$

where t' is the integration variable.

4.5.2 Results of linear analysis

For each length of the combustion chamber the simulation is run for 39.8 dimensionless time units, which is enough to observe whether the pressure oscillations grow or decay in time. The velocity between Sections 3 and 4 is excited initially for $t_{exc} = 13.3$ dimensionless time units by a broadband excitation in the range of the Strouhal number $0 \div 7.53$. After 13.3 till 39.8 dimensionless time units the system is left to evolve by itself without external excitations. The growth rate of the pressure perturbations at the dominant frequency of oscillations is calculated as in section 3.4.2 – by approximating the time history of the pressure oscillations by Eq. 3.11 recalled here:

$$p'(t) = \sum_{i=1}^n P_i \sin(2\pi f_i t + \phi_i) e^{\alpha_i(t-t_{exc})} \quad (4.14)$$

where f_i is one of the frequencies of pressure oscillations after t_{exc} , n is the number of the frequencies of pressure oscillations after t_{exc} , P_i is the amplitude of pressure oscillations at f_i at the time t_{exc} , ϕ_i is the phase of the pressure oscillations at f_i , α_i is the growth rate of the mode f_i .

The frequencies of oscillations and their growth rates are computed by approximating the time history of pressure oscillations at the beginning of Section 5 by Eq. 4.14 using the least-squares method. A positive value of the growth rate parameter α indicates that the system is unstable, and the negative

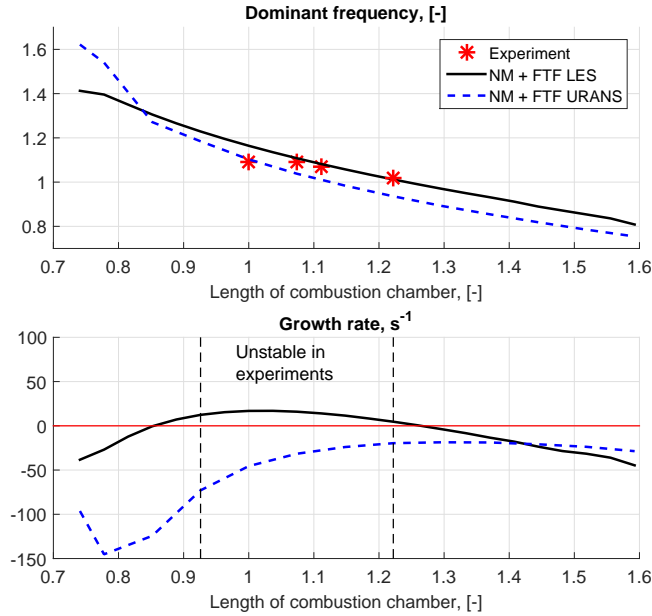


Figure 4.33: Dominant frequencies of the pressure oscillations and their growth rates for various lengths of the combustion chamber calculated using LES FTF model and URANS FTF model; outlet reflection coefficient $R_{out,1}$.

value of α mean that the system is stable. In the simulations presented in this chapter either one or none unstable frequency per run is detected, thus $n=1$ for all simulations in the network model in this chapter.

Two FTF models are tested in this section: the LES FTF model and the URANS FTF model for 10% excitation presented in section 4.4.1. The outlet reflection coefficient is taken equal to the experimentally measured $R_{out,1}$.

The dominant frequencies of pressure oscillations and their growth rates for various lengths of the combustion chamber are shown in Fig. 4.33. The frequencies are normalised with respect to the mean flow velocity at the burner exit and the diameter of the combustion chamber. The dominant frequency of oscillations decreases with increasing length of the combustion chamber. This subtends the acoustic nature of the modes computed in this chapter. The frequencies calculated with the two FTF models agree well with the experimentally observed frequency of the first longitudinal mode of the combustion chamber.

Thermoacoustic instabilities are observed in the experimental campaign in the range of combustion chamber length $L_{c.c.} = 0.93 \div 1.22$. Simulations in the network model with the LES FTF model capture qualitatively the unstable behaviour of the system and predict the setup to be unstable for the slightly wider range of the combustion chamber length $L_{c.c.} = 0.85 \div 1.30$ (see Fig. 4.33). In contrast, simulations with the URANS FTF model predict the setup to be stable in the whole range of combustor lengths. This is due to the differences between the FTFs computed with LES and URANS presented in Fig. 4.20.

4.5.3 Results of weakly nonlinear analyses

It is possible to perform a weakly nonlinear analysis using the network model and the nonlinear heat release model. Since the linear analysis with the URANS FTF model predicts the setup to be stable for each possible value of combustion chamber length, there is no reason to try FDF models 1 and 2 since they are both based on the URANS FTF model. FDF models 3, 4 and 5 are tested in this section.

The normalised velocity perturbations amplitude A required for the calculation of the instantaneous values of the parameters τ_i and σ_i is calculated as the maximum normalised amplitude of the velocity fluctuations between Sections 3 and 4 of the network model setup in the last 3.32 dimensionless time units preceding the current instant of simulation as described in sections 3.3.3 and 3.4.3. This time window allows to compute the normalised amplitude of velocity oscillations for frequencies higher than $0.15 St$. Each time step the UIR to be used in Eq. 4.13 is recalculated based on the current amplitude of velocity perturbations A .

The velocity between Sections 3 and 4 is excited for the first $t_{exc} = 13.3$ dimensionless time units by the broadband excitation in the range of the Strouhal number $0 \div 7.53$. After 13.3 and until 132.7 dimensionless time units the system is left to evolve by itself without external excitations. This time is enough to reach either saturation to a limit cycle pressure oscillations or infinitesimal pressure fluctuations. The maximum amplitudes of the pressure oscillations measured in the last 13.3 dimensionless time units of simulations at the beginning of the combustion chamber normalised by the maximum pressure oscillations amplitude in the experiment are reported.

Network model simulations with FDF model 3

The FDF model 3 presented in section 4.4.4 is used in the network model simulations. The outlet reflection coefficient is taken equal to the experimentally measured $R_{out,1}$. The calculated unstable frequencies shown in Fig. 4.34 slightly differ with respect to the frequencies calculated in the linear analysis with the LES FTF model (see Fig. 4.33). Simulations in the network model with the FDF model 3 predict the setup to be unstable in the range of the combustion chamber length $L_{c.c.} = 0.85 \div 1.41$ that is wider than the unstable range in experiments (see Fig. 4.33). The calculated amplitudes of the pressure oscillations are under-predicted by the network model simulations with the FDF model 3 (see Fig. 4.34). This is explained by the rapid change of the heat release response modelled with FDF model 3 when changing the amplitude of the velocity excitation. The maximum amplitude of the pressure oscillations in the network model simulations corresponds to the normalised combustor length 0.85. Meanwhile, in the experiments, the maximum pressure oscillations amplitude was observed with the normalised combustion chamber length 1.

The network model setup with the FDF model 3 is bistable for the combustion chamber length $L_{c.c.} = 0.85$. If the excitation of 1% of the mean velocity

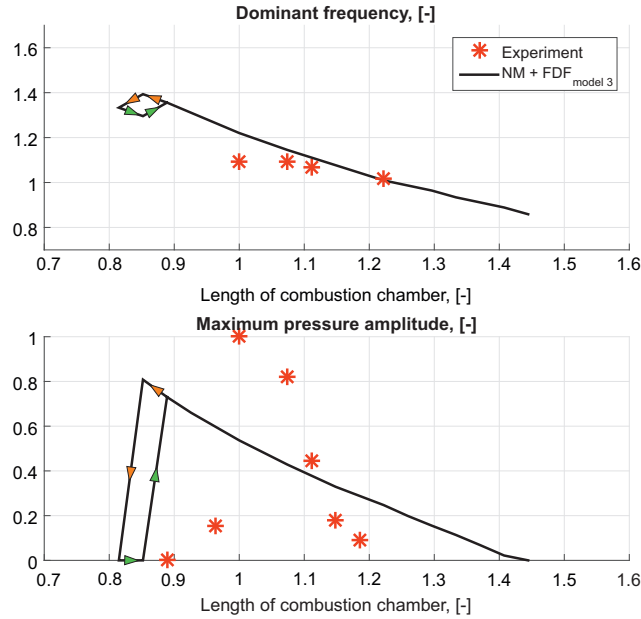


Figure 4.34: Unstable frequencies and amplitudes of pressure oscillations for various values of the combustion chamber length calculated with the network model and the FDF model 3; outlet reflection coefficient $R_{out,1}$ measured experimentally.

upstream the flame is applied to the network model, the setup is stable and all oscillations decrease after the excitation time t_{exc} . However, if the 15% excitation is applied to the network model with the combustion chamber length equal to $L_{c.c.} = 0.85$, the oscillations increase after the excitation time t_{exc} at the frequency higher than the dominant frequency calculated when 1% excitation is applied. It can be considered as a hysteresis. With the combustor length $L_{c.c.} = 0.89$ high-amplitude pressure oscillations are observed; the decrease of the combustion chamber length from this condition to the value $L_{c.c.} = 0.85$ leads to further pressure oscillation amplitude increase and increase of the frequency of oscillations (the path marked with orange arrows in Fig. 4.34). Further decrease of the combustor length to the value $L_{c.c.} = 0.81$ leads to the stabilisation of the system and the decrease of the dominant frequency of oscillations. Meanwhile, increasing the length of the combustion chamber from $L_{c.c.} = 0.81$ to the value $L_{c.c.} = 0.85$ does not bring the system to the instability and the dominant frequency of oscillations decreases (the path marked with green arrows in Fig. 4.34). Further increase of the combustor length to the value $L_{c.c.} = 0.89$ leads to the instability.

Network model simulations with FDF model 4

The frequencies and amplitudes of pressure fluctuations calculated with the FDF model 4 presented in section 4.4.5 are shown in Fig. 4.35. Three values of

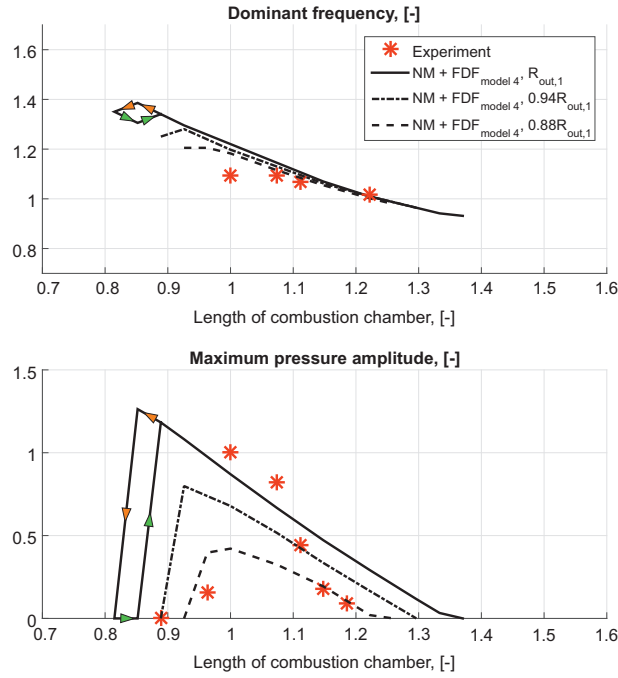


Figure 4.35: Unstable frequencies and amplitudes of pressure oscillations for various values of the combustion chamber length calculated with the network model and the FDF model 4.

the outlet reflection coefficient are considered: $R_{out,1}$, $0.94R_{out,1}$, and $0.88R_{out,1}$. Simulations in the network model with the FDF model 4 predict the setup to be unstable in the range of the combustion chamber length $L_{c.c.} = 0.85 \div 1.33$ that is wider than the unstable range in experiments (see Fig. 4.33).

The maximum amplitude of pressure oscillations in the network model simulations with the outlet reflection coefficient $R_{out,1}$ corresponds to the normalised combustor length 0.85. Meanwhile, in the experiments, the maximum pressure oscillations amplitude was observed with the normalised combustion chamber length 1. The maximum amplitude of the pressure oscillations calculated with the network model simulations, the outlet reflection coefficient $R_{out,1}$, and the FDF model 4 is over-predicted with respect to the experimentally observed value. The decrease of the outlet reflection coefficient to the values $0.94R_{out,1}$ and $0.88R_{out,1}$ leads to the shift of the maximum pressure oscillations amplitude to the combustor length values $L_{c.c.} = 0.93$ and $L_{c.c.} = 1$, respectively. At the same time, decrease of the outlet reflection coefficient leads to a more narrow unstable region in terms of the combustor length and to the decrease of the maximum pressure oscillations amplitude

The network model setup with the FDF model 4 and the outlet reflection coefficient $R_{out,1}$ is bistable for the combustion chamber length $L_{c.c.} = 0.85$. If the excitation of 1% is applied to the network model, the setup is stable and the oscillations decrease after the excitation time t_{exc} . However, if significant

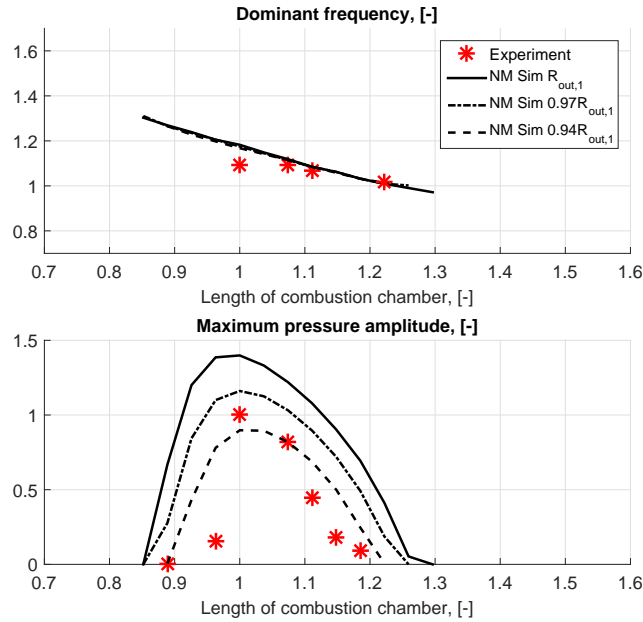


Figure 4.36: Unstable frequencies and amplitudes of pressure oscillations for various combustion chamber lengths and outlet reflection coefficients calculated with the network model and the FDF model 5.

excitation, e.g. 15%, is applied to the network model with the combustion chamber length equal to $L_{c.c.} = 0.85$, all oscillations increase after the excitation time $t_{exc.}$. Qualitatively the same hysteresis is observed as in the case of usage the FDF model 4 and the outlet reflection coefficient $R_{out,1}$. With the combustor length $L_{c.c.} = 0.89$ high-amplitude pressure oscillations are observed; decrease of the combustion chamber length from this condition to the value $L_{c.c.} = 0.85$ increases the pressure oscillation amplitude and increases the frequency of oscillations (the path marked with orange arrows in Fig. 4.35). Further decrease of the combustor length to the value $L_{c.c.} = 0.81$ leads to the stabilisation of the system and the decrease of the dominant frequency of oscillations. Meanwhile, increasing the length of the combustion chamber from $L_{c.c.} = 0.81$ to the value $L_{c.c.} = 0.85$ does not bring the system to the instability and the dominant frequency of oscillations decreases (the path marked with green arrows in Fig. 4.35). Further increase of the combustor length to the value $L_{c.c.} = 0.89$ leads to the instability.

Network model simulations with FDF model 5

Last, the FDF model 5 presented in section 4.4.6 is applied to the network model simulations. Simulations are performed for the range of combustion chamber lengths predicted to be unstable by the linear analysis and for three values of the outlet reflection coefficient $R_{out,1}$, $0.97R_{out,1}$, and $0.94R_{out,1}$. Results are presented in Fig. 4.36.

Unstable frequencies of the pressure oscillations in the weakly nonlinear

analysis with the FDF model 5 are the same as in the linear analysis with the LES FTF shown in Fig. 4.33. The nonlinear simulations with the FDF model 5 capture well the trend of the experimental dependence of the pressure oscillations amplitude on the length of the combustion chamber (see Fig. 4.36). The simulations employing the outlet reflection coefficient reduced by 6% with respect to the measured value yield the best match against the experimental data points.

4.6 Discussion

In this chapter, the three-step approach is applied to an industrial test rig equipped with an industrial gas turbine burner. The heat release response to the velocity excitation is calculated with URANS simulations in a broad range of frequencies for two excitation amplitudes. The heat release distribution in the URANS simulations and the FSC model is more dispersed along the combustion chamber than in the LES previously conducted by Rofi et al. [13] calculations with the AVBP solver of CERFACS. It could be due to the flame absence in the outer shear layer in URANS simulations and the high value of the Schmidt number used in the simulations. As a result, the Flame Transfer Function calculated with the URANS simulations does not agree with the previously conducted LES calculations. Further investigations on the FSC model parameters are required to understand possible reasons for the disagreements.

The linear analysis in the network model with the FTF calculated in the URANS simulations predicts the setup to be stable in the whole range of combustion chamber lengths, while in experiments for a certain range of lengths of the combustor the setup is unstable. The mismatch could be explained by the too dispersed heat release distribution in space.

The linear analysis in the network model with the FTF calculated by Rofi et al. [13] predicts the setup to be unstable in a slightly wider range of combustion chamber lengths than in experiments. A possible reason for the disagreement is the uncertainty in the measured value of the outlet reflection coefficient.

Nonlinear analyses are conducted in the network model with three hybrid Flame Describing Function models. The first two FDFs act as the FTF computed with LES in the linear regime and act as the FDFs calculated with the URANS simulations in the nonlinear regime. The network model simulations with the first FDF model and the reference outlet reflection coefficient underestimate the maximum amplitude of the pressure oscillations in the setup by 19% with respect to the experimental data and predict the combustor's length characterised by the maximum pressure oscillations amplitude to be shifted by 15%.

The network model simulations with the second FDF model and the reference outlet reflection coefficient also predict the combustor's length characterised by the maximum amplitude of the pressure oscillations to be shifted by 15%; however, the maximum pressure oscillations amplitude in the setup is overestimated by 26% with respect to the experimental data. The decrease of the outlet reflection coefficient by 12% brings the maximum pressure os-

cillations amplitude to the length, where the maximum was observed in the experiments; however, the amplitude of the pressure oscillations is 58% lower, than in the experiments. In network model simulations with these FDF models, hysteresis phenomena are observed.

The third FDF model degenerates into the FTF computed with LES for the low-amplitude excitations and inherits the FDF behaviour calculated for the BRS setup in section 3.3.3 for the high-amplitude excitations. The network model simulations with the third FDF model show good agreement with the experimental data both in terms of the unstable frequency and the amplitude of pressure oscillations. The best agreement is achieved when the outlet reflection coefficient is reduced by 6% with respect to the measured value. In fact, the outlet reflection coefficient can have a lower value because its measurement was corrupted by the microphone cooling.

Chapter 5

Conclusions and future investigations

Conclusions

Combustion instabilities are strong pressure oscillations occurring due to the coupling between acoustics, combustion and flow fluctuations. They pose a serious issue to the producers of gas turbines due to the damage they may cause. There is urgent need to develop reliable and simple tools to predict the onset of combustion instabilities from first principles and to find methods to suppress them.

Performing experimental analyses is costly and precise measurement techniques are required to understand the physics of the phenomenon. Conducting CFD analyses of the whole combustion system of the setup is expensive from the computational point view. Instead, hybrid techniques can be successfully used to forecast the onset of combustion instabilities.

In this work a three-step approach to predict combustion instabilities is proposed. The first step is to compute the response of the unsteady heat release to acoustic excitations; this is called the Flame Describing Function (FDF) approach. URANS simulations with the OpenFOAM software are used for this purpose with a Flame Speed Closure model. Compressible URANS simulations are employed because they yield reasonable precision for low frequency excitations and are computationally cheaper than LES. The second step is to approximate the computed FDF through analytic functions. The distributed time-lag FDF model is used in this work because it consists of few parameters that have physical meaning and their dependencies on the amplitude of the excitation are easily tracked. When the pressure drop of the gas in the burner is one order of magnitude higher than the pressure drop of the air in the burner and the fuel injection is situated on the swirler blades, the FDF model for technically premixed swirl-stabilised burners need fewer parameters than the FDF model for perfectly premixed swirl stabilised burners, despite the fact that the former displays a more complicated physics of heat release response to acoustic excitations. The third step of the approach consists in carrying out time-domain simulations of closed-loop combustion-acoustic interactions in a

low-order network model. Such a model, developed in the course of the thesis, is implemented in the MATLAB Simulink environment. Simulations in the time domain permit to predict both unstable frequencies of combustion-driven pressure oscillations and their amplitudes. Moreover, these simulations enable physical insight into important mechanisms.

The three-step approach is applied to analyse the thermoacoustic stability of a laboratory, perfectly premixed, swirl-stabilised test rig. The Flame Transfer Function (FTF) of the setup is calculated perturbing the velocity at the inlet of the computational domain with a broadband excitation and calculating the response of the heat release. Wiener-Hopf inversion is applied to calculate the FTF. The computed FTF differs from the experimentally calculated one because the FSC model used is adiabatic and the setup is strongly non-adiabatic. This results in different heat release distributions between simulations and experiments and, as a result, in a mild disagreement in the FTFs' phases. Then, the setup is perturbed with a monochromatic excitation at several frequencies and amplitudes. As a result, the Flame Describing Function of the setup is computed. The dependence of the FDF model parameters on the excitation amplitude is revealed. Afterwards, both linear and weakly nonlinear analyses are performed with the network model. Stability prediction of the network model coincides with the experimentally conducted stability analysis. The calculated unstable frequency does not coincide with the experimentally observed one, most probably due to the disagreement in the phase of the FTF as observed above. The unstable frequency of the setup is not a pure acoustic mode but is an Intrinsic Thermo-Acoustic (ITA) mode. Parametric analysis is performed to understand possible ways of suppression of the ITA mode. It is shown that the common technique of reducing the acoustic reflection coefficients at the boundaries in some conditions can make the setup even more unstable. It is proposed to reduce the plenum cross-section as a way of suppression of the ITA mode. Last, the weakly nonlinear thermoacoustic analysis in the network model is conducted. The dependence of the frequency of the ITA mode on the amplitude of the acoustic oscillations is shown.

The thermoacoustic stability of an industrial, technically premixed, swirl stabilised test rig is finally analysed with the three-step approach. The results obtained in this chapter are compared to a reference LES study of the setup. Unperturbed URANS simulation with the FSC model predicts more dispersed heat release distribution with respect to the LES. Nevertheless, the temperature distribution in the URANS simulation is close to the experimental one, so it is decided to perform the FDF calculations. The setup is excited with a broadband signal and the FTF of the industrial test rig is calculated again using Wiener-Hopf inversion. The FTF calculated with URANS differs from the FTF calculated previously with LES, because of the disagreement in the heat release distribution. The FDF of the setup is calculated performing URANS simulations at one excitation amplitude and three excitation frequencies. Then, several FDF models are presented. The first two models are based on the FDF computed with URANS and differ in the way the FTF phase at the highest excitation frequency is interpreted. The third and fourth FDF

models are constructed from the FTF calculated previously with LES and the FDF models 1 and 2. The fifth FDF model is a hybrid model composed from the LES FTF for the industrial setup and the FDF calculated with URANS for the laboratory test rig. Linear and weakly nonlinear analyses of the industrial test rig stability are performed with the network model. The linear analysis with the URANS FTF predicts the setup to be stable in the whole range of combustor's lengths, whereas in the experimental campaign with certain lengths of the combustion chamber the setup is unstable. This disagreement is due to the FTF calculated in URANS that is affected by the heat release distribution. The linear analysis with the LES FTF predicts the setup to be unstable in the slightly wider range of combustor's lengths than in experiments. This happens most probably due to the value of the outlet reflection coefficient that was measured inaccurately in the experiments. The dominant frequencies of the setup computed with both FTF models agree well with the experimentally observed values. Network model simulations with the FDF model 4 capture qualitatively the trend of the pressure oscillations amplitude dependence on the combustor's length measured experimentally. The weakly nonlinear analysis in the network model gives good agreement when the FDF model 5 is used and the outlet reflection coefficient is diminished by 6% with respect to the measured value. This reflects the uncertainty inherent with such a measurement.

Lessons learned

The following lessons are learned in the present work:

- The time-domain analysis with a low-order network model is a fertile tool to investigate thermoacoustic instabilities in gas turbines.
- Stability of an Intrinsic Thermo-Acoustic (ITA) mode strongly depends on the acoustic parameters of the setup: reflection coefficients, ducts' length, and cross-sectional area of the ducts. The usual approach of combustion instabilities suppression by the reduction of the absolute value of the reflection coefficient could render the ITA mode even more unstable. The decrease of the plenum cross-sectional area is suggested as a method of suppression of the unstable ITA modes.
- The model for the FDF of the perfectly premixed flames is proposed. The change of the FDF model parameters with the excitation amplitude is supported by the analysis of the heat release distribution under excitation in comparison to the unperturbed one. The strong feature of the proposed FDF model is that the model parameters can be determined from a small number of the CFD simulations due to the small number of these parameters.
- The distribution of unsteady heat release component of the tested technically premixed flame due to acoustic excitations can be assumed propor-

tional to the distribution of the unperturbed heat release distribution, in the case of low amplitude excitation.

- Analysis of the mechanisms driving combustion instability has shown that heat release response to acoustic perturbations of certain technically-premixed, swirl-stabilised, burners can be modelled with just 4 parameters. It is shown that time-domain analysis in the network model with this simple flame model is able to predict both frequency and amplitude of unstable pressure fluctuations.

Ideas for future investigations

The following ideas for future investigations have arisen in the course of the work:

- Calculate the heat release response of the laboratory test rig to acoustic excitation with the recent model proposed by Tay-Wo-Chong et al. [108] that take into account heat losses.
- Perform thermoacoustic analysis of technically premixed combustion systems with tools that solve Helmholtz equation in three dimensions with two distributed time-lag flame model, similarly to how the flame is modelled in this work. Until today, in Helmholtz solver tools, technically premixed flames are modelled through the distribution of a single time-lag.
- Calculate heat release response to acoustic oscillations in different parts of the industrial burner using a Multiple-Input Single-Output method. Separate the burner duct in the network model of the industrial setup into two parallel ducts and model the heat release response to acoustic oscillations in different ducts of the burner.
- Further analysis on the FSC model parameters should be done for the technically premixed setup. Also, a lower value of the lower inflammability limit should be checked. This should result in the appearance of the heat release in the outer shear layer and the shift of the heat release distribution closer to the one previously calculated with LES.
- The FDF computed numerically for the industrial setup is going to be validated against the experimentally calculated FDF. Computation of the FDF with at least one more excitation amplitude is recommended for further improvement of the FDF model. The outlet reflection coefficient needs to be computed with better precision.
- Entropy waves should be considered in the network model of the technically premixed burner. Both the formation of entropy waves and their propagation should be modelled with care. First, only one of the two mechanisms in the current FDF model is able to produce entropy waves.

Second, entropy waves are dispersed as they travel in the flow with non-uniform velocity field in the cross-section and they are highly diffused due to the presence of recirculation zones in combustors with swirl burners. The solution to both of these issues is to calculate a so-called Entropy Transfer Function – the response of the temperature at the end of the recirculation zones to velocity fluctuations upstream of the flame.

5. *Conclusions and future investigations*

Acknowledgements

First of all, I am very thankful to my wife, Kateryna Iurasheva, for her permanent support, this work would not have been possible if I had not met her. I acknowledge Ezio Cosatto for his help with acoustics and for his patience. I would like to thank Vyacheslav Vasilievich Anisimov for his continuous assistance with numerical combustion and for fruitful conversations about thermoacoustics.

I would like to thank Prof. Maria Heckl for a smooth running of the TANGO project and for many useful discussions. I am thankful to Prof. Wolfgang Polifke for his very warm hospitality at the Technical University of Munich during my secondment. I would like to acknowledge Alp Albayrak for familiarising me with the BRS setup and for the consultancy with the OpenFOAM environment. Assistance from Dr Joel Guerrero with the OpenFOAM environment is also highly appreciated.

I would like to acknowledge all of Ansaldo Energia staff for their support. Particularly, I am thankful to Luca Rofi for providing results of LES calculations and to Edoardo Bertolotto for giving me experimental data for the industrial test rig.

Last but not least, I am thankful to the destiny for giving me the two splendid supervisors - Professor Alessandro Bottaro and Dr Giovanni Campa. I highly appreciate their help with my research and assistance with everyday issues that I had plenty during these years.

The presented work is part of the Marie Curie Initial Training Network *Thermo-acoustic and Aero-acoustic Nonlinearities in Green combustors with Orifice structures* (TANGO). I gratefully acknowledge the financial support from the European Commission under call FP7-PEOPLE-ITN-2012.

I acknowledge the CINECA award under the ISCRA initiative, for the availability of High-Performance Computing resources and support.

Bibliography

- [1] Poinso, T., and Veynante, D., 2005. *Theoretical and Numerical Combustion*, 2nd ed. Edwards, Philadelphia.
- [2] Kroner, M., Sattelmayer, T., Fritz, J., Kiesewetter, F., and C., H., 2007. “Flame propagation in swirling flows - Effect of local extinction on the combustion induced vortex breakdown”. *Combustion Science and Technology*, **179**, pp. 1385–1416.
- [3] Heeger, C., Gordon, R., Tummers, M., Sattelmayer, T., and A., D., 2010. “Experimental analysis of flashback in lean premixed swirling flames: upstream flame propagation”. *Experiments in Fluids*, **49**, pp. 853–863.
- [4] Lieuwen, T. C., 2012. *Unsteady combustor physics*. Cambridge University Press, New York, NY.
- [5] Campbell, J., and Chambers, J., 1994. *Patterns in the sky, Natural visualization of aircraft flow fields*. NASA Langley Research Center, Hampton, Virginia. NASA-SP-514.
- [6] Rijke tube. See URL https://en.wikipedia.org/wiki/Rijke_tube.
- [7] Sewell, J., and Sobieski, P., 2005. “Monitoring of combustion instabilities: Calpine’s experience”. In *Combustion instabilities in gas turbine engines: operational experience, fundamental mechanisms, and modeling*, eds. T.C. Lieuwen and V. Yang, eds. American Institute of Aeronautics and Astronautics, Reston, VA, ch. 7, pp. 147–162.
- [8] Goy, C., James, S., and Rea, S., 2005. “Monitoring combustion instabilities: E.ON UK’s experience”. In *Combustion instabilities in gas turbine engines: operational experience, fundamental mechanisms, and modeling*, eds. T.C. Lieuwen and V. Yang, eds. American Institute of Aeronautics and Astronautics, Reston, VA, ch. 8, pp. 163–175.
- [9] Tay-Wo-Chong, L., Bomberg, S., Ulhaq, A., Komarek, T., and Polifke, W., 2012. “Comparative validation study on identification of premixed flame transfer function”. *Journal of Engineering for Gas Turbines and Power*, **134**, pp. 021502–1,8.
- [10] Huber, A., and Polifke, W., 2009. “Dynamics of practical premixed flames, part ii: identification and interpretation of cfd data”. *International Journal of Spray and Combustion Dynamics*, **1 (2)**, pp. 229–250.

BIBLIOGRAPHY

- [11] Laera, D., Gentile, A., Camporeale, S., Bertolotto, E., Rofi, L., and Bonzani, F., 2015. “Numerical and experimental investigation of thermoacoustic combustion instability in a longitudinal combustion chamber: influence of the geometry of the plenum”. GT2015-42322.
- [12] Hermeth, S., Staffelbach, G., Gicquel, L., Anisimov, V., Cirigliano, C., and Poinsot, T., 2014. “Bistable swirled flames and influence on flame transfer functions”. *Combustion and Flame*, **161** (1), pp. 184–196.
- [13] Rofi, L., Campa, G., Anisimov, V., Daccà, F., Bertolotto, E., Gottardo, E., and Bonzani, F., 2015. “Numerical procedure for the investigation of combustion dynamics in industrial gas turbines: LES, RANS and thermoacoustics”. GT2015-42168.
- [14] Goodwin, D. G., Moffat, H. K., and Speth, R. L., 2014. Cantera: An object-oriented software toolkit for chemical kinetics, thermodynamics, and transport processes. <http://www.cantera.org>. Version 2.1.2.
- [15] Lokai, V., Maksutova, M., and Strunkin, V., 1991. *Gas turbines of aircraft engines*. Mashinostroenie, Moscow. (in Russian).
- [16] Frank-Kamenetskii, D., 1987. *Diffusion and heat transfer in chemical kinetics*. Nauka, Moscow, USSR.
- [17] Yun, A., 2010. *Modelling of turbulent flows*. URSS, Moscow, Russian Federation.
- [18] Peters, N., 2010. *Turbulent combustion*. Cambridge University Press, Cambridge, UK.
- [19] Thibaut, D., and Candel, S., 1998. “Numerical study of unsteady turbulent premixed combustion: Application to flashback simulation”. *Combustion and Flame*, **113**, pp. 53–65.
- [20] Chan, C., Lau, K., Chin, W., and Cheng, R., 1992. “Freely propagating open premixed turbulent flames stabilized by swirl”. *24th Symposium (International) on Combustion*, **24** (1), pp. 511–518.
- [21] Rijke, P., 1859. “On the vibration of the air in a tube open at both ends”. *Philosophical Magazine*, **17**, pp. 419–422.
- [22] Culick, F. E. C., 2006. *Unsteady motions in combustion chambers for propulsion systems*. NATO Research and Technology Organisation. RTO-AG-AVT-039.
- [23] Oefelein, J., and Yang, V., 1993. “Comprehensive review of liquid-propellant combustion instabilities in F-1 engines”. *Journal of Propulsion and Power*, **9** (5), pp. 657–677.

-
- [24] Sirignano, W. A., 2015. “Driving mechanisms for combustion instability”. *London Edinburgh and Dublin Philosophical Magazine and Journal of Science*, **17**, pp. 419–422.
- [25] Zel’dovich, Y., 1946. “The oxidation of nitrogen in combustion explosions”. *Acta Physicochimica U.S.S.R.*, **21**, pp. 577–628.
- [26] Lavoie, G., Heywood, J., and Keck, J., 1970. “Experimental and theoretical study of nitric oxide formation in internal combustion engines”. *Combustion Science and Technology*, **1** (4), pp. 313–326.
- [27] Lieuwen, T., and Yang, V., 2005. *Combustion Instabilities in Gas Turbine Engines: Operational Experience, Fundamental Mechanisms, and Modeling*. American Institute of Aeronautics and Astronautics, Reston, VA.
- [28] Huang, Y., and Yang, V., 2009. “Dynamics and stability of lean-premixed swirl-stabilized combustion”. *Progress in Energy and Combustion Science*, **35**, pp. 293–364.
- [29] Marble, F., and Candel, S., 1977. “Acoustic disturbance from gas non-uniformities convected through a nozzle”. *Journal of Sound and Vibration*, **55**(2), pp. 225–243.
- [30] Dowling, A., and Stow, S., 2005. “Acoustic analysis of gas turbine combustors”. In *Combustion instabilities in gas turbine engines: operational experience, fundamental mechanisms, and modeling*, eds. T.C. Lieuwen & V. Yang, ed. American Institute of Aeronautics and Astronautics, Reston, VA, ch. 13, pp. 369–414.
- [31] Silva, C., Emmert, T., Jaensch, S., and Polifke, W., 2015. “Numerical study on intrinsic thermoacoustic instability of a laminar premixed flame”. *Combustion and Flame*, **162**, pp. 3370–3378.
- [32] Courtine, E., Selle, L., and Poinso, T., 2015. “DNS of Intrinsic ThermoAcoustic modes in laminar premixed flames”. *Combustion and Flame*, **162**, pp. 4331–4341.
- [33] Franzelli, B., Riber, E., Gicquel, L., and Poinso, T., 2012. “Large Eddy Simulation of combustion instabilities in a lean partially premixed swirled flame”. *Combustion and Flame*, **159**, pp. 621–637.
- [34] Staffelbach, G., Gicquel, L., Boudier, G., and Poinso, T., 2009. “Large eddy simulation of self-excited azimuthal modes in annular combustors”. In *Proceedings of the Combustion Institute*, Vol. **32** (2), pp. 2909–2916.
- [35] Urbano, A., Selle, L., Staffelbach, G., Cuenot, B., Schmitt, T., Ducruix, S., and Candel, S., 2016. “Exploration of combustion instability triggering using large eddy simulation of a multiple injector liquid rocket engine”. *Combustion and Flame*, **169**, pp. 129–140.

- [36] Komarek, T., and Polifke, W., 2010. “Impact of swirl fluctuations on the flame response of a perfectly premixed swirl burner”. *Journal of Engineering for Gas Turbines and Power*, **132**, p. 061503.
- [37] Palies, P., Durox, D., Schuller, T., and Candel, S., 2011. “Nonlinear combustion instability analysis based on the flame describing function applied to turbulent premixed swirling flames”. *Combustion and Flame*, **158**, pp. 1980–1991.
- [38] Čosić, B., Moeck, J. P., and Paschereit, C. O., 2014. “Nonlinear instability analysis for partially premixed swirl flames”. *Combustion Science and Technology*, **186** (6), pp. 713–736.
- [39] Krediet, H., Beck, C., Krebs, W., Schimek, S., Paschereit, C. O., and Kok, J., 2012. “Identification of the flame describing function of a premixed swirl flame from LES”. *Combustion Science and Technology*, **184**, pp. 888–900.
- [40] Lauer, M., and Polifke, W., 2010. “On the adequacy of chemiluminescence as a measure for heat release in turbulent flames with mixture gradients”. *Journal of Engineering for Gas Turbines and Power*, **132**, pp. 061502–1–8.
- [41] Dowling, A., and Mahmoudi, Y., 2015. “Combustion noise”. *Proceedings of the Combustion Institute*, **35** (1), pp. 65–100.
- [42] Bellucci, V., Schuermans, B., Nowak, D., Flohr, P., and Paschereit, C., 2005. “Thermoacoustic modeling of a gas turbine combustor equipped with acoustic dampers”. *Journal of Engineering for Gas Turbines and Power*, **127**, pp. 372–379.
- [43] Polifke, W., 2010. Low-order analysis tools for aero- and thermo-acoustic instabilities. Lecture Series 1, Von Karman Institute for Fluid Dynamics, Rhode-St-Genes, Belgium, November.
- [44] Schuermans, B., Guethe, F., Pennell, D., Guyot, D., and Paschereit, C., 2010. “Thermoacoustic modeling of a gas turbine using transfer functions measured under full engine pressure”. *Journal of Engineering for Gas Turbines and Power*, **132**, pp. 111503–1–9.
- [45] Bothien, M., Noiray, N., and Schuermans, B., 2015. “Analysis of azimuthal thermo-acoustic modes in annular gas turbine combustion chambers”. *Journal of Engineering for Gas Turbines and Power*, **137**, pp. 061505–1–8.
- [46] Schuermans, B., Polifke, W., Paschereit, C., and van der Linden, J., 2000. “Prediction of acoustic pressure spectra in combustion systems using swirl stabilized gas turbine burners”. In Proceedings of IGTI TE2000. 2000-GT-0105.

- [47] Heckl, M. A., 2013. “Analytical model of nonlinear thermo-acoustic effects in a matrix burner”. *Journal of Sound and Vibration*, **332**, pp. 4021–4036.
- [48] Kim, K., Lee, J., Quay, B., and Santavicca, D., 2010. “Spatially distributed flame transfer functions for predicting combustion dynamics in lean premixed gas turbine combustors”. *Combustion and Flame*, **157**, pp. 1718–1730.
- [49] Camporeale, S., Fortunato, B., and Campa, G., 2011. “A finite element method for three-dimensional analysis of thermoacoustic combustion instability”. *Journal of Engineering for Gas Turbines and Power*, **133** 1, p. 011506.
- [50] Schulze, M., Hummel, T., Klarmann, N., Berger, F., Schuermans, B., and Sattelmayer, T., 2016. “Linearized Euler equations for the prediction of linear high-frequency stability in gas turbine combustors”. In Proceedings of ASME Turbo Expo. GT2016-57818.
- [51] Gikadi, J., 2014. “Prediction of Acoustic Modes in Combustors using Linearized Navier-Stokes Equations in Frequency Space”. PhD Thesis, Technical University of Munich, Garching, Germany.
- [52] Nicoud, F., Benoit, L., Sensiau, C., and Poinso, T., 2007. “Acoustic modes in combustors with complex impedances and multidimensional active flames”. *AIAA Journal*, **45** (2), pp. 426–441.
- [53] Pankiewicz, C., and Sattelmayer, T., 2003. “Time domain simulation of combustion instabilities in annular combustors”. *Journal of Engineering for Gas Turbines and Power*, **125**, pp. 677–685.
- [54] Li, J., and Morgans, A., 2015. “Time domain simulations of nonlinear thermoacoustic behaviour in a simple combustor using a wave-based approach”. *Journal of Sound and Vibration*, **346**, pp. 345–360.
- [55] Silva, C., Nicoud, F., Schuller, T., Durox, D., and Candel, S., 2013. “Combining a Helmholtz solver with the flame describing function to assess combustion instability in a premixed swirled combustor”. *Combustion and Flame*, **160**, pp. 1743–1754.
- [56] Hangos, K., Lakner, R., and Gerzson, M., 2001. *Intelligent Control Systems: An Introduction with Examples*. Applied Optimization. Springer.
- [57] Emmert, T., Jaensch, S., Sovardi, C., and Polifke, W., 2014. “tax - a flexible tool for low-order duct acoustic simulation in time and frequency domain”. In 7th Forum Acusticum.
- [58] Bigongiari, A., and Heckl, M., 2015. “A Green’s function approach to the study of hysteresis in a Rijke tube”. In Proceedings of the 22nd International Congress on Sound and Vibration.

BIBLIOGRAPHY

- [59] Bigongiari, A., and Heckl, M., 2016. “A Green’s function approach to the rapid prediction of thermoacoustic instabilities in combustors”. *Journal of Fluid Mechanics*, **798**, pp. 970–996.
- [60] Crocco, L., and Cheng, S., 1956. *Theory of combustion instability in liquid propellant rocket motors*. Butterworths Publications LTD., London, UK.
- [61] Laera, D., Campa, G., Camporeale, S., Bertolotto, E., Rizzo, S., Bonzani, F., Ferrante, A., and Saponaro, A., 2014. “Modelling of thermoacoustic combustion instabilities phenomena: Application to an experimental test rig”. *Energy Procedia*, **45**, pp. 1392–1401.
- [62] Campa, G., and Camporeale, S., 2014. “Prediction of the thermoacoustic combustion instabilities in practical annular combustors”. *Journal of Engineering for Gas Turbines and Power*, **136** **9**, pp. 091504–1–10.
- [63] Krebs, W., Flohr, P., Prade, B., and Hoffmann, S., 2002. “Thermoacoustic stability chart for high intensity gas turbine combustion systems”. *Combustion Science and Technology*, **174** **(7)**, pp. 99–128.
- [64] Paschereit, C., Schuermans, B., Bellucci, V., and Flohr, P., 2005. “Implementation of instability prediction in design: Alstom approaches”. In *Combustion instabilities in gas turbine engines: operational experience, fundamental mechanisms, and modeling*, eds. T.C. Lieuwen & V. Yang, ed. American Institute of Aeronautics and Astronautics, Reston, VA, ch. 15, pp. 445–481.
- [65] Tay-Wo-Chong, L., and Polifke, W., 2013. “Large eddy simulation-based study of the influence of thermal boundary condition and combustor confinement on premix flame transfer functions”. *Journal of Engineering for Gas Turbines and Power*, **135**, pp. 021502–1,9.
- [66] Sayadi, T., Le Chenadec, V., Schmid, P. J., Richecoeur, F., and Massot, M., 2014. “Thermoacoustic instability a dynamical system and time domain analysis”. *Journal of Fluid Mechanics*, **753**, pp. 448–471.
- [67] Dowling, A., 1997. “Nonlinear self-excited oscillations of a ducted flame”. *Journal of Fluid Mechanics*, **346**, pp. 271–290.
- [68] Gentemann, A., Yuen, S., and Polifke, W., 2004. “Influence of boundary reflection coefficient on the system identifiability of acoustic two-ports”. In *Proceedings of the 11th International Congress on Sound and Vibration*, pp. 3501–3508.
- [69] Luzzato, C., and Morgans, A., 2015. “The effect of a laminar moving flame front on thermoacoustic oscillations of an anchored ducted V-flame”. *Combustion Science and Technology*, **187**, pp. 410–427.

- [70] Bothien, M., Moeck, J., Lacarelle, A., and C.O., P., 2007. “Time domain modelling and stability analysis of complex thermoacoustic systems”. *Proceedings of the Institution of Mechanical Engineers, Part A: Journal of Power and Energy*, **221** (5), pp. 657–668.
- [71] Kolmogorov, A., 1991. “The local structure of turbulence in incompressible viscous fluid for very large reynolds numbers”. *Proceedings of the Royal Society A*, **434**, pp. 9–13.
- [72] Orszag, S. A., 1970. “Analytical theories of turbulence”. *Journal of Fluid Mechanics*, **41** (2), pp. 363–386.
- [73] Smagorinsky, J., 1963. “General circulation experiments with the primitive equations i. the basic experiment”. *Monthly Weather Review*, **91** (3), pp. 99–164.
- [74] Pitsch, H., 2006. “Large-Eddy Simulation of turbulent combustion”. *Annual Review of Fluid Mechanics*, **38**, pp. 453–482.
- [75] Spalding, D., 1971. “Mixing and chemical reaction in steady confined turbulent flames”. *13th Symposium (International) on Combustion*, **13** (1), pp. 649–657.
- [76] Magnussen, B., and Hjertager, B., 1976. “On mathematical modeling of turbulent combustion with special emphasis on soot formation and combustion”. *16th Symposium (International) on Combustion*, **16**, pp. 719–729.
- [77] van Oijen, J., and de Goey, L., 2000. “Modelling of premixed laminar flames using Flamelet-Generated Manifolds”. *Combustion Science and Technology*, **161**, pp. 113–137.
- [78] Peters, N., 1982. “The premixed turbulent flame in the limit of a large activation energy”. *Journal of Non-Equilibrium Thermodynamics*, **7**, pp. 25–38.
- [79] Kerstein, A., Ashurst, W., and Williams, F., 1988. “Field equation for interface propagation in an unsteady homogeneous flow field”. *Physical Review A*, **37** (7), pp. 2728–2731.
- [80] Karpov, V., Lipatnikov, A., and Zimont, V., 1994. “A model of premixed turbulent combustion and its validation”. *Archivum Combustionis*, **14**, pp. 125–141.
- [81] Lipatnikov, A., and Chomiak, J., 2002. “Turbulent flame speed and thickness: phenomenology, evaluation, and application in multi-dimensional simulations”. *Progress in Energy and Combustion Science*, **28**, pp. 1–74.

- [82] Yasari, E., Verma, S., and Lipatnikov, A., 2015. “Rans simulations of statistically stationary premixed turbulent combustion using flame speed closure model”. *Flow, Turbulence and Combustion*, **94**, pp. 381–414.
- [83] Lipatnikov, A., and Sathiah, P., 2005. “Effects of turbulent flame development on thermoacoustic oscillations”. *Combustion and Flame*, **142**, pp. 130–139.
- [84] OpenFOAM, 2014. User Guide. Version 2.3.0.
- [85] Weller, H. G., Tabor, G., Jasak, H., and Fureby, C., 1998. “A tensorial approach to computational continuum mechanics using object-oriented techniques”. *Computers in Physics*, **12 (6)**, pp. 620–631.
- [86] LeVeque, R. J., 2002. *Finite Volume Methods for Hyperbolic Problems*. Cambridge University Press, Cambridge, UK.
- [87] Favre, A., 1965. The equations of compressible turbulent gases. Annual Summary Report 1, Institut de Mecanique Statistique de la Turbulence, 12, Avenue du General Leclerc, Marseille, France, January.
- [88] Menter, F., 1994. “Two-equation eddy-viscosity turbulence models for engineering applications”. *AIAA Journal*, **32 (8)**, pp. 1598–1605.
- [89] Menter, F., Kuntz, M., and Langtry, R., 2003. “Ten years of industrial experience with the sst turbulence model”. In *Turbulence, Heat and Mass Transfer 4*, K. Hanjalić, Y. Nagano, and M. Tummers, eds. Begell House, Inc., pp. 625–632.
- [90] Launder, B., and Sharma, B., 1974. “Application of the energy-dissipation model of turbulence to the calculation of flow near a spinning disc”. *Letters in Heat and Mass Transfer*, **1**, pp. 131–138.
- [91] Launder, B., and Spalding, D., 1974. “The numerical computation of turbulent flows”. *Computer Methods in Applied Mechanics and Engineering*, **3**, pp. 269–289.
- [92] Wilcox, D., 1988. “Reassessment of the scale-determining equation for advanced models”. *AIAA Journal*, **26 (11)**, pp. 1299–1310.
- [93] Menter, F., Ferreira, J. C., Esch, T., and Konno, B., 2003. “The SST turbulence model with improved wall treatment for heat transfer predictions in gas turbines”. In Proceedings of the International Gas Turbine Congress. IGTC2003-TS-059.
- [94] Lipatnikov, A., 2012. *Fundamentals of Premixed Turbulent Combustion*. CRC Press.
- [95] Noiray, N., Durox, D., Schuller, T., and Candel, S., 2008. “A unified framework for nonlinear combustion instability analysis based on the flame describing function”. *Journal of Fluid Mechanics*, **615**, pp. 139–167.

- [96] Polifke, W., Poncet, A., Paschereit, C., and Dobbeling, K., 2001. “Reconstruction of acoustic transfer matrices by instationary computational fluid dynamics”. *Journal of Sound and Vibration*, **245**, pp. 483–510.
- [97] Wickert, M., 2011. *Introduction to signals and systems*. ECE2610 Lecture Notes, Electrical and Computer Engineering College of Engineering and Applied Sciences, University of Colorado, US.
- [98] Press, W., Flannery, B., Teukolsky, S., and Vetterling, W., 1986. *Numerical recipes*. Cambridge University Press, Cambridge, UK.
- [99] Astrom, K., and Murray, R., 2008. *Feedback Systems: An Introduction for Scientists and Engineers*. Princeton University Press.
- [100] Strobio-Chen, L., Bomberg, S., and Polifke, W., 2016. “Propagation and generation of acoustic and entropy waves across a moving flame front”. *Combustion and Flame*, **166**, pp. 170–180.
- [101] Lieuwen, T., Torres, H., Johnson, C., and Zinn, B., 2001. “A mechanism of combustion instability in lean premixed gas turbine combustors”. *Journal of Engineering for Gas Turbines and Power*, **123**, pp. 182–189.
- [102] Huber, A., and Polifke, W., 2009. “Dynamics of practical premixed flames, part i: model structure and identification”. *International Journal of Spray and Combustion Dynamics*, **1 (2)**, pp. 199–228.
- [103] Cho, J., and Lieuwen, T., 2005. “Laminar premixed flame response to equivalence ratio oscillations”. *Combustion and Flame*, **140**, pp. 116–129.
- [104] Albayrak, A., Blumenthal, R., Ulhaq, A., and Polifke, W., 2015. “An analytical model for the impulse response of laminar premixed flames to equivalence ratio perturbations”. In Proceedings of the Combustion Institute. <http://dx.doi.org/10.1016/j.proci.2016.06.002>.
- [105] Schuermans, B., Belluci, V., Guethe, F., Meili, F., Flohr, P., and Paschereit, C., 2004. “A detailed analysis of thermoacoustic interaction mechanisms in a turbulent premixed flame”. pp. 539–551. GT2004-53831.
- [106] Idelchik, I., 1992. *Handbook of Hydraulic Resistance, 3rd Edition*. Mashinostroenie, Moscow. (in Russian).
- [107] Poinso, T., and Lele, S., 1992. “Boundary conditions for direct simulations of compressible viscous flows”. *Journal of Computational Physics*, **101**, pp. 104–129.
- [108] Tay-Wo-Chong, L., Zellhuber, M., Komarek, T., Im, H., and Polifke, W., 2016. “Combined influence of strain and heat loss on turbulent premixed flame stabilization”. *Flow, Turbulence and Combustion*, **97 (1)**, pp. 263–294.

BIBLIOGRAPHY

- [109] Heckl, M. A., 2015. “A new perspective on the flame describing function of a matrix flame”. *International Journal of Spray and Combustion Dynamics*, **7**, pp. 91–112.
- [110] Bomberg, S., Emmert, T., and Polifke, W., 2015. “Thermal versus acoustic response of velocity sensitive premixed flames”. *Proceedings of the Combustion Institute*, **35** (3), pp. 3185–3192.
- [111] Emmert, T., Bomberg, S., Jaensch, S., and Polifke, W., 2017. “Acoustic and intrinsic thermoacoustic modes of a premixed combustor”. *Proceedings of the Combustion Institute*, **36** (3), pp. 3835–3842.
- [112] Silva, C. F., Merk, M., Komarek, T., and Polifke, W., 2016. “The contribution of intrinsic thermoacoustic feedback to combustion noise and resonances of a confined turbulent premixed flame”. In *Thermoacoustic instabilities in Gas Turbines and Rocket engines*.
- [113] Jaensch, S., and Polifke, W., 2016. “On the uncertainty encountered when modeling self-excited thermoacoustic oscillations with artificial neural networks”. In *International Symposium on Thermoacoustic Instabilities in Gas Turbines and Rocket Engines*. Paper No. GTRE-006.
- [114] Hermeth, S., 2012. “Mechanisms affecting the dynamic response of swirled flames in gas turbines”. PhD Thesis, National Polytechnic Institute of Toulouse, Toulouse, France.
- [115] Price, R., Hurle, I., and Sugden, T., 1969. “Optical studies of the generation of noise in turbulent flames”. *Proceedings of Combustion Institute*, **12** (1), pp. 1093–1102.
- [116] Jang, S., and Ih, J., 1997. “On the multiple microphone method for measuring in-duct acoustic properties in the presence of mean flow”. *Journal of the Acoustical Society of America*, **103** (3), pp. 1520–1526.
- [117] Schonfeld, F., and Rudgyard, M., 1999. “Steady and unsteady flows simulations using the hybrid flow solver AVBP”. *AIAA Journal*, **137** (11), pp. 1378–1385.
- [118] Hermeth, S., Staffelbach, G., Gicquel, L., and Poinso, T., 2013. “Les evaluation of non-linear effects on the dynamic flame response in a real gas turbine combustion chamber”. GT2013-95699.
- [119] Selle, L., Lartigue, G., Poinso, T., Koch, R., Schildmacher, K., Krebs, W., Prade, B., Kaufmann, P., and Veynante, D., 2004. “Compressible large eddy simulation of turbulent combustion in complex geometry on unstructured meshes”. *Combustion and Flame*, **137** (4), pp. 489–505.
- [120] Colin, O., Ducros, F., Veynante, D., and Poinso, T., 2000. “A thickened flame model for large eddy simulations of turbulent premixed combustion”. *Physics of Fluids*, **12** (7), pp. 1843–1863.

- [121] Han, X., Li, J., and Morgans, A., 2015. “Prediction of combustion instability limit cycle oscillations by combining flame describing function simulations with a thermoacoustic network model”. *Combustion and Flame*, **162**, pp. 3632–3647.
- [122] Zander, L., 2015. “Numerical analysis of the flame dynamics in a re-heat combustor”. MSc Thesis, Technical University of Berlin, Berlin, Germany.